WASHINGTON UNIVERSITY IN ST. LOUIS

Department of Physics

Dissertation Examination Committee:
Henric Krawczynski, Chair
James Buckley
Roger Chamberlain
Ramanath Cowsik
Martin Israel
Jill Pasteris

Time-Dependent Studies of High-Energy Radiation from Blazars

by

Sarah Elizabeth Thibadeau

A dissertation presented to the
Graduate School of Arts and Sciences
of Washington University in
partial fulfillment of the
requirements for the degree
of Doctor of Philosophy

December 2012

Saint Louis, Missouri

Contents

List of Figures

List of Tables

Acknowledgements

The work that I have done here would not be possible without the love and support of a myriad of people, and I'm grateful for the opportunity to highlight their contributions.

First and foremost, I would like to thank my advisor, Henric Krawczynski. Without his wealth of information, ideas, and feedback, this work would not be possible, and his guidance and support have helped me navigate the world of graduate school with great success.

Thank you also to Jim Buckley, whose help as an unofficial "second advisor" has consistently provided me with thoughtful and interesting feedback and guidance, and who has helped shaped this work in important ways. And thank you to Marty Israel. His steady support and counsel as a member of my Faculty Mentoring Committee were always invaluable.

I would also like to acknowledge and thank the additional members of my dissertation committee - Roger Chamberlain, Ram Cowsik, and Jill Pasteris. They provided extremely thought-provoking, insightful comments about this thesis. Thank you also to both the McDonnell Center for Space Sciences for the Virgil I. Grisson Fellowship, the U.S. Department of Education GAANN Fellowship Program, as well as the U.S. Department of Energy grant DEFG0291ER40628, and NASA grants NNX10AJ56G and NNX09AU08G.

Thank you to the amazing VERITAS community of professors, post-docs, graduate students, staff, and crew. The collaboration provided a fantastic opportunity for hands-on work with an

always interesting and passionate team of people. And thank you to the additional members of the WashU high-energy astro group, including my officemates Kelly, Vicky, and Qingzhen, as well as Matthias, Slava, the Ryans, Jerrad, John E., Brian, Richard, Trey, Fabian, Nathan, and Avery, for making our workplace such a friendly and fun place to go every day.

A huge thank you to the members of the WashU Department of Physics community. I couldn't have asked for a better, more friendly and supportive environment in which to complete my graduate degree, and I consider myself so lucky to have been a member of this community. I want to especially thank Sarah Hedley, without whom the department wouldn't run and who was always such a jovial and warm presence. I also want to say a special thank you to Julia Hamilton, the mom-away-from-home to all of us physics graduate students. I know I couldn't have made it through graduate school without her or her hugs. I always knew that I could pop into her office at any time for a chance to talk about anything; I never walked away from Julia without a big smile on my face.

Thank you to the members of our fledgling Physics Outreach Committee - Ben, Kasey, Pat, Anders, Yan Mei, Jen, and Nilushi. I am so proud of the work we have done, and it was always a joy to work together. I'm so grateful for all of their ideas, encouragement, and feedback. And thank you to those taking the reins of the Outreach Committee - I feel that we are leaving our "baby" in very capable hands.

I was fortunate to have made a wonderful group of friends at WashU, and I want to thank them all for making my graduate school world exciting and rich. In addition to those already mentioned, thank you especially to Patrick, Mike, Flavin, Dan, Jeff, Lauren, Dimitris, as well as all the members of This Team Goes To 11 (with a special shout-out to the Scottish Arms) and Crowbar. Because of you, I always knew to expect fun and adventure.

Most importantly, thank you to my parents Theresa and Andy. There are almost no words to express how much their tireless, selfless support, love, and encouragement have sustained me throughout my entire career. They were always there to share in my triumphs, weather my tears with me, give me words of wisdom and advice, and act as cheerleaders for as long as I can remember. Especially when times grew difficult, I knew I was never alone and that they were always a quick phone call away. I wouldn't have even thought this path possible were it not for their boundless faith in me. I definitely would not have made it through graduate school without them.

And, of course, thank you to my new husband, Brett. We met at the very beginning of graduate school, got married at the very end, and there was never a day that went by in between that I didn't think myself the luckiest woman in the world to have him as my partner and best friend. His tireless patience, love, and encouragement sustained and enriched me throughout the last five years, and knowing that this is the just the beginning of our lives together has filled me with a joy I never thought possible.

ABSTRACT OF THE DISSERTATION

Time-Dependent Studies of High-Energy Radiation from Blazars

by

Sarah Elizabeth Thibadeau

Doctor of Philosophy in Physics

Washington University in St. Louis, 2012

Professor Henric Krawczynski, Chairperson

We have used X-ray and both GeV and TeV gamma-ray temporal data to conduct a probe into possible Lorentz invariance violation dispersion effects, as well as to look into possible correlations between different energy bands in blazar emission.

Some quantum gravity models predict a breaking of Lorentz invariance at an energy level, E_{QG}, generally thought to be close to the Planck energy, which may result in energy-dependent corrections to the photon dispersion relation. By using the ground-based gamma-ray telescope VERITAS to look at the arrival times of high-energy radiation from a large flare from the blazar Mrk 421, we have been able to place strong constraints on E_{QG}, assuming both a linear correction and a quadratic correction to the standard dispersion relation.

Our search for Lorentz invariance violation assumed the simultaneous emission of different energy radiation by the source. This assumption can be tested by modeling particle acceleration and emission processes. To help identify relevant processes, we looked for potential correlations between X-ray data (from the Swift-XRT satellite) and GeV gamma-ray data (from the Fermi-LAT satellite) using the discrete correlation function (DCF). By applying the DCF to 6 different blazars, we have found no correlations between X-ray and GeV gamma-ray emission. The finding does not bolster, but is consistent with, leptonic models, in which electrons of different energies produce the X-ray and gamma-ray emission in inverse-Compton processes.

Chapter 1

Introduction and Theoretical Background

1.1 General Introduction

Observational astrophysics is a relatively peculiar branch of physics. While the work may be considered experimental as opposed to purely theoretical, as astrophysicists often work with data from real astrophysical objects, it is a different kind of experimental process. Astrophysicists cannot construct a star or black hole in a laboratory, carefully control its environment, or alter one variable at a time to look for effects. They cannot yet traverse interstellar distances to visit the source. They must instead build instruments that let them view astrophysical objects with increasingly better degrees of precision. Part of the challenge of being an astrophysicist is learning to adapt to the realities of observational work, and learning to derive solid conclusions from sparse data. For example, the discovery of high-energy emission or a flaring episode from start to finish from a specific source can often be predicted, but just as often these discoveries may be the result of a serendipitous decision to look at a particular source or region of the sky. One important thing to remember - and this will be seen in the two projects developed in this thesis - is that astrophysicists, as observers, must contend with the natural behavior of the sources being studied, and must develop ways

of doing so intelligently so as to extract quantitative conclusions about the physical processes at work.

Once observational instruments, whether they be space- or Earth-based, collect data from an astrophysical source, the products can then be used for a variety of different studies. In general, these studies can be split into two very broad categories - studies of the make-up of the universe, and studies that test fundamental physics. The former category involves, for example, understanding specific objects, classes of objects, the medium between objects, and the behavior of that medium. The latter category takes advantage of the fact that astrophysical environments are often far larger and more energetic that those than can be found or created here on Earth. This gives scientists opportunities to probe processes that cannot be realized in laboratories on Earth; hence, studies of astrophysical processes and environments can lead to the development of fundamental physics.

The path to constructing any new science often involves first observing and measuring the properties of photons with astrophysical origins, then seeking to determine how they were created, why they have the energy that they do, how they got from source to observer (i.e., what happened to them as they travelled), and how photons of different energies relate to one another. As these questions are answered, new insights may be derived - from a more complete picture of the specific object, or of the *class* of objects, those photons came from, to the general mechanism that created them, to the environments they travelled through on their way to the observer, to any sort of physics of a more fundamental nature.

The two projects presented in this thesis each represent one of the broad categories of astrophysical study. The first, which we are calling the **Lorentz Invariance Violation** (LIV) analysis, uses data from an extragalactic source to look into whether or not the photon dispersion relation may in fact have energy-dependent corrections to it, particularly in the

high-energy regime. We can do this by looking for propagation-induced, energy-dependent arrival time delays in flux data (Amelino-Camelia et al. (1998)). This study demonstrates how certain probes into fundamental physics require energies and conditions not otherwise accessible; astrophysics thus fills in the gaps of what we are capable of achieving solely here on Earth.

In the second project, which we are referring to as the **Discrete Correlation Function** (DCF) analysis, we compare the gamma-ray flux as a function of time to the X-ray flux as a function of time from several different extragalactic sources, with the goal of determining whether the behavior of the photon flux between the two energy bands is correlated. Investigations into the potential correlations between energy bands can provide useful insights into the nature of the emission mechanisms and regions of the sources studied, particularly if trends are found across several different sources. Thus, this project demonstrates how astrophysical observations can be used to build up and expand upon existing information about the contents of the universe.

Although these two projects are quite different in scope and execution, they complement each other in important ways. LIV studies that use time delay-based analyses - as many do, including this one - require the assumption that radiation of different energies be emitted by the source simultaneously. We can strengthen that assumption by gaining a better understanding of the source physics. DCF analysis seeks to achieve that better understanding, particularly with regard to emission mechanisms and the nature of emission regions, which means that any results that come from this study have the potential to be used in the future designs of LIV experiments.

There also lies within these two projects important similarities that make them excellent conceptual companion pieces. As the title states, they are both time-dependent studies of

high-energy radiation emitted from blazars (a class of active galactic nuclei, which will be discussed later). The three key ideas from this title (time-dependent studies, high-energy radiation, and blazars) form the theoretical underpinnings of this thesis, which affords a good opportunity for us to provide a brief description of each of these terms, so that we may establish a baseline vocabulary for the rest of the work.

1.1.1 A Description Of Important Terms

Temporal Studies

Time-dependent studies provide a powerful means for us to characterize a targeted source's behavior over a period of time, in a way other astrophysical studies (such as time-independent spectral analysis) cannot. Temporal data can be expressed in several ways, though the two ways we will be using here are data sets of the *flux* of photons in a given energy range as a function of time (a plot of this information is called a *light curve*), and *event lists*, which are compilations of the energies of individual photons and the times at which they were observed (where the observation of a photon is often called an "event"). Studies that are specifically designed to look at the radiation from an astrophysical source as a function of time relay information about how the source and the source's environment may be evolving, or about the nature of the environment the radiation traversed as it propagated from source to observer. Both the LIV and the DCF studies of this thesis are very good examples of the power and the breadth of temporal studies.

A Brief History of High-Energy Astrophysics

The electromagnetic spectrum extends from the low energy radio waves all the way up to the highest-energy gamma rays; each band of radiation has its own rich history. The "gamma-ray" classification typically covers the range of a few keV all the way up to the *Very High Energy* (VHE) band at > 100 GeV energies. The study of VHE gamma rays constitute a relatively young subfield of astrophysics; TeV photons have been described as embodying

"one of the last frontiers of the gamma-ray sky" (Weekes (2005)). Although the theory and seeds of the detector technology have been around since the late 1940's (for historical reviews and broader perspectives on the detector techniques, please look to Weekes (2005)), it was not until the first definitive detection of TeV photons from the Crab nebula by the Whipple Observatory on Mount Hopkins in Arizona (see the seminal paper Weekes et al. (1989)) that the field really took off. This discovery is of particular importance because not only does it hold the distinction of being the first detection of TeV gamma rays from a specific source, detected with a high significance of 9 σ, but it was the first time the imaging atmospheric Cherenkov technique (see Chapter 3 for more information) could successfully distinguish the high-energy signal from gamma rays from the high-energy background signal caused by cosmic rays. Since then, the rapid development of increasingly sophisticated ground-based and space-borne detectors has led to an explosion of discoveries and the emergence of a whole new field of study (see Buckley et al. (2002), Weekes (2008), and Hinton and Hofmann (2009) for reviews of the history, status, and goals of gamma-ray astronomy).

Special attention should also be given to the Fermi satellite (see Chapter 3 for the technical details). Launched in June of 2008, its very high sensitivity to a broad range of energy (roughly 20 MeV to over 300 GeV) led to the detection of 1873 gamma-ray sources in its first two years of operation (please refer to their second catalog, Nolan et al. (2012)). In the few years since, it has served as an excellent complement to ground-based instruments, and helped sustain the rapid development of high-energy astrophysics.

The two studies presented in this thesis take advantage of the cutting edge advances in the field of gamma-ray astronomy to probe physics in new ways.

Blazars

Blazars are a sub-category of *active galactic nuclei* (AGN), which are "believed to be supermassive black holes, 10^8 - 10^{10} $M_\odot$, accreting matter from the nucleus of a host galaxy" (Buckley et al. (2002)). Blazars are AGN that have one of their jets pointing roughly towards the observer (see, for example, Ghisellini et al. (1998) and the references therein), which enables observers to essentially stare down the central engine of extremely energetic and violent objects. Because of the relativistic motion of the jet plasma, this orientation causes a beaming of the emitted radiation (for example, see Urry and Padovani (1995)). As will be discussed later when, in Chapter 4, we delve into the specific sources used in this thesis, there are two types of blazars - *Flat Spectrum Radio Quasars* and *BL Lac objects*. Blazars also comprise some of the farthest known sources (the farthest known blazar, Q0906+6930, is at a redshift of 5.47; see Romani et al. (2004)), and they are known for, among other things, fast variability and violent flares that emit photons with energies into the TeV regime.

Of historical importance are the contributions of both radio and gamma-ray observations to the understanding of blazars. For example, radio observatories, which have monitored blazars for years, have provided valuable information about the nature of the parsec-scale jets of blazars, including jet speeds and Doppler beaming factors (see, for example, Savolainen et al. (2010) and the references therein). Fermi in particular has added significantly to blazar physics - for example, the large catalog of Fermi-detected AGN (Ackermann et al. (2011)) shows the satellite's potential for important contributions towards blazar science. Good examples are measurements of the luminosity functions of a large sample of blazars (Ajello et al. (2012)), in-depth studies of blazar emission lines and the correlation with the jet power (Sbarrato et al. (2012)), and full analyses of blazar spectral energy distributions (Abdo et al. (2010b)).

The remainder of this chapter will provide the background physics that motivate each of the projects in this thesis.

1.2 Lorentz Invariance Violation

Quantum gravity (QG) theories have emerged as attempts to unite gravitational theories with those of quantum mechanics (Jacobson et al. (2005), Mattingly (2005), Will (2006)). Though the various theories are divergent in many ways, many predict some kind of violation of Lorentz invariance (LIV). Experimentally, at some energy level, we should see the speed of light deviating from the commonly known value of "c" in an energy-dependent manner. Radiation of a higher energy may subsequently travel faster (or slower) than radiation of a lower energy; mathematically, the normal photon dispersion relation will change to reflect an energy dependence. Thus, one possible verification of QG theories is through an attempt at experimental measurements of the LIV effect by determining to what degree propagation affects travel times. Amelino-Camelia et al. (1998) were the first to propose the idea of an experimental test of LIV through the use of time-of-flight measurements.

The breaking of Lorentz invariance is generally supposed to occur at or near the Planck energy scale ($\approx 1.22 \times 10^{19}$ GeV), which is derived from the Planck mass. When accounting for gravitational interactions, the Planck mass is the mass elementary particles would have to have for gravitational coupling to become significant (see, for example, Perkins (2003)):

$$M_{\text{Planck}} = \left(\frac{\hbar c}{G}\right)^{1/2} \approx 1.22 \times 10^{19}\ \text{GeV}/c^2 \tag{1.1}$$

where G is the gravitational constant ($= 6.673 \times 10^{-11}$ N m^2 kg^{-2}), and thus the Planck energy is the associated rest mass energy:

$$E_{\text{Planck}} = \left(\frac{\hbar c^5}{G}\right)^{1/2} \approx 1.22 \times 10^{19}\ \text{GeV}. \tag{1.2}$$

Note that the values of the Planck mass, and thus the Planck energy, are derived from the particular combination of fundamental constants that achieve the proper units of mass and energy, respectively, as given by equations 1.1 and 1.2. As discussed in Perkins (2003), if two elementary particles, each with a mass equal to the Planck mass, are separated by the Planck length (ie, the Compton wavelength associated with the Planck mass), their gravitational potential energy is equal to their rest masses, thus making quantum gravitational effects important at the Planck scale - and thus providing one argument for why the Planck scale may be the threshold at which Lorentz invariance may break. (From a purely analytical point of view, Scargle et al. (2008) put forth another, similar argument - the above combinations of fundamental constants that naturally yield quantities on the Planck scale provide a good candidate for the potential scale at which quantum gravity effects become important because they contain fundamental constants from each realm of physics - i.e., from gravity, relativity, and quantum mechanics.)

Although TeV photons fall well short of the Planck energy scale, it was proposed (Amelino-Camelia et al. (1998)) that, given VHE radiation from a distant (i.e., extragalactic) astrophysical source, tiny propagation-induced effects of the order $\sim 1\ \mathrm{TeV}/\mathrm{E}_{\mathrm{Planck}}$ could potentially still be observed.

1.2.1 LIV Theoretical Background

As of yet, there is no definitive prediction of the mathematical form of the altered photon dispersion relation. However, many theories predict a symmetry breaking at an energy on the order of the Planck energy scale (Rodríguez Martínez and Piran (2006)). If we assume that the energy of radiation emitted from various astrophysical sources is much lower than this energy scale, we can expand the known, energy-independent, dispersion relation ($E^2 = p^2c^2$) as a function of the photon energy in units of the Planck energy:

$$\frac{p_{ph}^2\, c^2}{E_{ph}^2} - 1 = \sum_{n=1}^{\infty} s_n \left(\frac{E_{ph}}{\xi_n\, E_{pl}} \right)^n \tag{1.3}$$

where the LHS of the equation represents the original dispersion relation and the RHS the LIV corrections. Note that E_{pl} is the Planck energy, valued at $\approx 1.22 \times 10^{19}$ GeV, and ξ_n is a scaling factor such that $\xi_n E_{pl} = E_{QG,n}$, i.e., the "quantum gravity" energy scale at which this effect is supposed to occur. (A discussion of "s_n" is below.) Finding the scaling factor ξ_n amounts to finding this energy scale, which remains one of the more important overall goals. Also note that our assumption allows us to neglect all but the leading order correction term, which, depending on the QG theories used, may be linear (n=1) or quadratic (n=2).

Supposing that two photons of different energies (with E_h representing the higher energy photon and E_l representing the lower energy photon) are emitted from a source of redshift z at the same time, we can derive the subsequent delay in their arrival times, using cosmological considerations and the fact that although the *proper* distances the two photons travel are different, their *comoving* distances are the same and can be equated (Jacob and Piran (2008), Rodríguez Martínez and Piran (2006)).

$$\Delta t = t_h - t_l = s_n \frac{1+n}{2H_0} \frac{E_h^n - E_l^n}{(\xi_n E_{pl})^n} \int_0^z \frac{(1+z')^n\, dz'}{\sqrt{\Omega_\Lambda + \Omega_m (1+z')^3}} \tag{1.4}$$

where s_n is -1 for the super-luminal case (negative delay - higher energy photons travel faster than lower energy ones) and s_n is $+1$ for the sub-luminal case (positive delay - higher energy photons travel slower than lower energy ones) (Abdo et al. (2009a)). Note that we will use a standard cosmology, with values from the latest WMAP results, Jarosik et al. (2011): H_0, the Hubble constant, is 71.0 km/sec/Mpc, Ω_Λ, the energy density of dark energy, is 0.734, and Ω_m, the total energy density of matter (baryonic and dark), is 0.266. We can also write a similar expression for the delay one photon, of energy E_0, would experience due to LIV effects, by comparing when it actually arrives, t^{obs}, with when it should have arrived were there no LIV dispersive effects, t':

$$\Delta t = t^{obs} - t' = s_n \frac{1+n}{2H_0} \left(\frac{E_0}{\xi_n E_{pl}} \right)^n \int_0^z \frac{(1+z')^n \, dz'}{\sqrt{\Omega_\Lambda + \Omega_m (1+z')^3}} \tag{1.5}$$

Once again, we have defined ξ_n such that $\xi_n E_{pl} = E_{QG,n}$, i.e., the so-called quantum gravity energy scale.

Eqn. 1.5 provides the theoretical framework for an experimental test. The process of applying this expression to a real experimental test will be discussed in the next chapter.

1.3 Discrete Correlation Function

Multiwavelength studies of the emission from an astrophysical source provide a wealth of information that single energy studies cannot; these types of studies can give greater insights into the behavior of the specific sources studied, as well as the class of sources. A common practice in multiwavelength studies is to analyze temporal correlations between the behavior in different energy bands. Such correlations, or lack thereof, can give information about, for example, the size and location of emitting regions in blazars (see, for example, Misra et al. (2010)). Linking different energy bands can help constrain the models that govern the mechanisms responsible for emission in those bands (see, for example, Krawczynski et al. (2004a) and Fossati et al. (2008a)).

For the purposes of this thesis, to search for correlations we will rely on the fairly robust method that uses the statistical tool called the "discrete correlation function" (DCF). Edelson and Krolik (1988) introduced this function by expanding on the "correlation function" commonly used in temporal studies.

In the next section, we will discuss the key statistical tools used to characterize light curves. A more detailed discussion can be found in Priestley (2004).

1.3.1 Time Series Analysis

In the language of time series analysis (in which a time series is simply any process that is time-dependent), the process plotted in a light curve - the emission of flux as a function of time - may be thought of as "random". A random process (also called "stochastic" or "non-deterministic") is one whose outcome may change each time a measurement is taken. Or, in other words, there is no mathematical formula that can be constructed to predict the flux from a source at any given point in time. As discussed in Priestley (2004), there are three scenarios as to why the process may be considered random: the system itself may contain random elements, the system may be deterministic but so complex that it must be considered random, or statistical errors may introduce randomness.

Random processes are described by probability theory, in which each possible outcome of the random process is called a "realization". In the following, our starting point is a list of observed fluxes, $\{f_1, f_2, ..., f_N\}$, from an astrophysical source measured at certain times (or, more precisely, measured in certain time intervals). That list of observed fluxes can be thought of as a realization of a random process that contains all three "randomizing" elements from above. In general, not only is our understanding of the emission region and mechanisms often too poor to enable us to construct a function that could predict the observed flux, but the observational methods used to record the data will inject noise - i.e., an element of randomness - into the system. Probability theory will enable us to mathematically characterize the structure of a light curve, as well as compare different light curves; this in turn allows us to constrain the process that gave rise to the light curve, and the physical environment in which it occurred.

Probability

Suppose we have a discrete random variable, X, that is a function of time and whose possible measured values form the set $\{x_i\}$, where $i = 0, 1, 2, ...$ For a given time, t_i, we can construct

the probability that a particular value x_i will be measured by performing our experiment n times. Supposing that x_1 is measured n_1 times, x_2 measured n_2 times, etc, such that $n_1 + n_2 + ... = n$, as n gets very large, we can define the probability, p_i that a specific x_i will be measured as simply n_i/n.

From this basic definition we can construct a number of important concepts used to characterize any given realization. The mean, μ, of a data set $\{x_1, x_2, ..., x_k\}$ is

$$\mu = \frac{1}{n} \sum_{i=1}^{k} n_i \, x_i = \sum_{i=1}^{k} p_i \, x_i \tag{1.6}$$

which represents a typical value of the data, where we have used the definition of probability, $p_i = n_i/n$. The variance of the data is then

$$\frac{1}{n} \sum_{i} n_i (x_i - \mu)^2 = \sum_{i} p_i (x_i - \mu)^2 \tag{1.7}$$

The square root of the variance gives the standard deviation, σ.

$$\sigma = \sqrt{\frac{1}{n} \sum_{i} n_i (x_i - \mu)^2} = \sqrt{\sum_{i} p_i (x_i - \mu)^2} \tag{1.8}$$

This value gives a measure of the spread of the data - i.e., how much overall deviation from the mean the data set exhibits. As can be seen, p_i acts as a weight that results in more probable values being more heavily favored in the mean and standard deviation.

To simplify matters, we can write the mean and the standard deviation using a simple device known as the "expectation operator". Since the mean is just the "typical" - or, "expected" - value of our random variable, we can write it simply with this notation:

$$\mu = E[X] \equiv \sum_{i} p_i \, x_i \tag{1.9}$$

And so we can easily write the variance (i.e., the square of the standard deviation) as

$$\sigma^2 = E[(X - \mu)^2] = \sum_i p_i (x_i - \mu)^2 \tag{1.10}$$

One Important Case: A case that is often seen is when each value is equally weighted, so that p_i reduces to $1/n$. Thus, we get the well-known equations for mean and standard deviation:

$$\mu = \frac{\sum_i x_i}{n} \tag{1.11}$$

$$\sigma = \sqrt{\frac{\sum_i (x_i - \mu)^2}{n}} \tag{1.12}$$

Moments

We can build upon the ideas of mean and standard deviation to arrive at equations that give a statistical sense of the structure of one data set as well as allow us to compare two data sets.

Since the mean and standard deviation are together not enough to fully characterize a data set (many vastly different looking data sets can still, in principle, have the same mean and standard deviations) (Priestley (2004)), we can define a more general expression, called the moment of power r, where $r = 1, 2, 3, ...$:

$$\mu'_r = \sum_i p_i \, x_i^r = E[X^r] \tag{1.13}$$

$$\mu_r = \sum_i p_i \, (x_i - \mu)^r = E[(X - \mu)^r] \tag{1.14}$$

where the first equation is the "moment about the origin" and the second equation is the "moment about the mean". Of course, when $r = 1$, the first equation simply reduces to the

mean (and the second equation to 0), and when $r = 2$, the second equation reduces to the variance (and the first equation to $\sigma^2 + \mu^2$, which contains no new information). Though we will not use them here, moments of higher orders will contain information about asymmetry ($r = 3$), flatness ($r = 4$), etc. (Priestley (2004))

Cross-Correlation and Auto-Correlation

Because our analysis requires us to compare two different data sets, we must expand the mathematics developed thus far to encompass two data sets at once. Suppose we have two random variables, $X(t)$ and $Y(t)$, each with its own mean (μ_x and μ_y, respectively) and standard deviation (σ_x and σ_y). Given their joint probability distribution p_{ij}, we can easily write their r^{th}, s^{th} moments about the origin and about the means:

$$\mu'_{rs} = \sum_i \sum_j p_{ij}\, x_i^r\, y_j^s = E[X^r\, Y^s] \tag{1.15}$$

$$\mu_{rs} = \sum_i \sum_j p_{ij}\, (x_i - \mu_x)^r\, (y_j - \mu_y)^s = E[(X - \mu_x)^r\, (Y - \mu_y)^s] \tag{1.16}$$

(Note that when either r or s equals 0, the moment simply becomes the individual moment for the other random variable.)

An important equation comes from setting both $r = s = 1$ in the moment about the means. This is called the covariance, and is a measure of the "linear association" (Priestley (2004), pg. 78) between the two data sets:

$$Cov[X(t), Y(t)] = E[(X - \mu_x)\, (Y - \mu_y)] \tag{1.17}$$

To normalize this, we simply divide by $\sqrt{\sigma_x^2\, \sigma_y^2}$. This gives the *correlation function*:

$$Corr[X(t), Y(t)] = \frac{E[(X - \mu_x)\,(Y - \mu_y)]}{\sqrt{\sigma_x^2\,\sigma_y^2}} \tag{1.18}$$

$$= \frac{\sum_i \sum_j (x_i - \mu_x)\,(y_j - \mu_y)\,p_{ij}}{\sqrt{\sigma_x^2\,\sigma_y^2}} \tag{1.19}$$

Because of the normalization, the correlation function can take on any value from -1 to +1. The product $(x_i - \mu_x)\,(y_j - \mu_y)$ represents every possible pair of data points from each data set X and Y. Of course, we expect that the points within each data set will fluctuate about their respective means. Things start to become interesting when we look at the fluctuations in each data set together. When the points x_i and y_j are both greater than their respective means, then of course the product $(x_i - \mu_x)\,(y_j - \mu_y)$ will be positive. The farther away each is from their means, the larger the product. Similarly, when the points x_i and y_j are both less than their respective means, then of course the product $(x_i - \mu_x)\,(y_j - \mu_y)$ will also be positive. If this type of trend - where the behavior of one data point with respect to its mean is mirrored in the other data set - occurs with all of the pairs of data points (or enough of them such that the effect is not washed out), then the covariance function is large and positive. The normalization factor thus results in a correlation function that is close to +1, and indicates that there is a positive linear trend between the two data sets.

In a similar vein, when one point is greater than its mean and the other is less than its mean, the product $(x_i - \mu_x)\,(y_j - \mu_y)$ will of course be negative. Once again, the greater the difference, the greater the magnitude of the product. When enough data pairs exhibit this trend, the resulting covariance function will be large and negative - and the correlation function will be close to -1, suggesting a negative linear trend.

Finally, if one component of the pair largely deviates from its mean and the other does not,

the two effects cancel, leaving a product close to 0. Furthermore, if we see a mix of positive and negative trends, the sum over all the data pairs will cancel the two effects, also leaving a correlation function close to 0; both of these scenarios suggest little correlation. (This does not necessarily suggest, though, that the two data sets are *independent* of each other - see Priestley (2004) for more details.)

The correlation function is used to compare two data sets, and can be applied to one of the main questions of this thesis - does the temporal behavior in one energy band always signal that similar temporal behavior will occur in another energy band a time τ later? This notion of an inherent time lag - which we denote as τ - is an important one, and we can further develop the properties of the correlation function to allow us to quantify the answer.

To do this, we must first introduce the notion of a stationary process. Complete stationarity, which indicates that "the statistical properties [of a function] do not change with time" (Priestley (2004), pg. 104) - and thus that the joint probability distributions for all combinations of X sampled at different times must always be equal, even when their times are shifted - can be a rather stringent requirement. A far more forgiving - and realistic - requirement is for stationarity up to order m (Priestley (2004)). This simply asks that the moments up to order m be equal, even through time shifts. This gives us three important consequences that will be of immediate use to us: (1) $E[X(t)]$ (i.e., the mean) is constant in time, (2) $E[X^2(t)]$ (i.e., the standard deviation) is constant in time, and (3) when we wish to compare two values of X at different points in time, the expectation value $E[X(t)\,X(s)]$ is a function of the difference $(t-s)$ only - and thus, the covariance of $X(t)$ and $X(s)$ is a function of $(t-s)$ only. (Priestley (2004), pg. 106)

Now suppose that we take s to be $t+\tau$, where τ, our time lag, can take on any possible time shift value. We immediately have the auto-covariance function, which we have already seen

will just be a function of τ:

$$AutoCov(\tau) = E[(X(t) - \mu)\,(X(t+\tau) - \mu)] \tag{1.20}$$

and normalized we get the *Auto-Correlation function*:

$$AutoCorr(\tau) = \frac{E[(X(t) - \mu)\,(X(t+\tau) - \mu)]}{\sigma^2} \tag{1.21}$$

which, like the regular correlation function, can range in value from -1 and +1, with the usual interpretations for those values. The auto-correlation function allows us to compare one data set with itself to see if there are any patterns or similarities between points separated by τ. In principle, we should see a peak to +1 at $\tau = 0$ (since of course there we are just comparing a data point with itself). We also expect a decay of some sort to 0 as $|\tau| \to \infty$ for non-periodic data. How quickly the auto-correlation function decays as $|\tau|$ gets larger represents the "memory of the process" (Priestley (2004), pg. 108).

Now suppose we wish to do something similar to the auto-correlation function, this time comparing *two* data sets. Extending the above arguments to two data sets to obtain the cross-covariance function is straight-forward:

$$CrossCov(\tau) = E[(X(t) - \mu_s)\,(Y(t+\tau) - \mu_y)] \tag{1.22}$$

And then we once again normalize to obtain the *Cross-Correlation function*:

$$CrossCorr(\tau) = \frac{E[(X(t) - \mu_x)\,(Y(t+\tau) - \mu_y)]}{\sqrt{\sigma_x^2\,\sigma_y^2}} \tag{1.23}$$

As before, the cross-correlation function should take on any value between -1 and +1, with the usual interpretations. The main difference between the cross- and auto-correlation functions is that the cross-correlation function need not peak at $\tau = 0$ - it can peak anywhere (Priestley

(2004)). Where it peaks will give us information about what sort of correlation may exist between the two data sets. If there are no clearly defined peaks, then this suggests little correlation between the two data sets. If there *is* a clearly defined peak, then this provides some measure of evidence that there is some correlation - that there is some trend that is mirrored in both the data sets, separated in time by the time lag τ.

The research presented in this thesis will apply the method of the cross-correlation function to real data, and then investigate the statistical significance of any findings through Monte Carlo simulations. The discussion through this point has relied on a fairly idealized notion of data sets. As already pointed out, any analysis of astrophysical data has to contend with the realities of observational challenges. How this analysis will do so, using the discrete correlation function (DCF), will be presented in the next chapter.

1.4 Gamma-Ray Emission Processes

In order to execute the two studies in this thesis, we will be relying on observed data in the gamma-ray regime (TeV for the LIV analysis, and GeV for the DCF analysis), as well as data in the X-ray regime for the DCF analysis. We therefore must introduce the various mechanisms that can be responsible for creating X-ray and gamma-ray photons. Before we get into specific processes, however, we will first look into a very general concept that forms the basis for what will follow - this is the idea of a radiating charged particle.

1.4.1 Lamor's Formula

An important foundation for any discussion of radiation is the simplest way radiation may be generated - through the acceleration of charged particles. The fact that a charged particle will radiate when it accelerates is a well-studied area of electrodynamics. (For a rigorous treatment of this type of material, an advanced textbook on electrodynamics - the classic one

is Jackson (1998) - would be an excellent source. Alternatively, Rybicki and Lightman (1979) provides in-depth coverage of this topic, with an eye towards astrophysical applications.) In general, we must consider two cases: where the accelerating particle is non-relativistic, and where it is relativistic.

Non-relativistic: When a charged particle accelerates (i.e., its speed increases or decreases, or its direction of motion changes), it loses energy in the form of radiation. When the speed of the particle is non-relativistic, we can rely on the famous *Lamor's Formula* to give an expression for that energy loss (note this formula is given is CGS, not SI, units):

$$P = \frac{dE}{dt} = \frac{2q^2a^2}{3c^3} \tag{1.24}$$

where P is the power, q is the charge of the accelerating particle, a is the acceleration, and c is the speed of light.

Relativistic: As is typical, the picture becomes a little more complicated when the accelerating particle has a relativistic speed. The relativistic form of Lamor's Formula is:

$$P = \frac{dE}{dt} = \frac{2q^2}{3c^3}\gamma^4(a_\perp^2 + \gamma^2 a_\parallel^2) \tag{1.25}$$

where γ is the particle's Lorentz factor and $a_\perp$ and $a_\parallel$ are the components of the particle's acceleration that are perpendicular and parallel, respectively, to the particle's velocity. From examining this formula, it is interesting to note that the parallel component of the acceleration will contribute significantly more to the energy loss than the perpendicular component.

We will return to these formulae later as we develop more specific forms of emission mechanisms.

1.4.2 Synchrotron Radiation

Synchrotron radiation is one of the more important emission mechanisms for non-thermal astrophysical sources such as blazars. Note that for the purposes of this discussion, we really only need to consider the case where the particle is moving relativistically. When a particle with charge q moves through a magnetic field, $\mathbf{B}$, with a relativistic velocity $\mathbf{v}$, it experiences a force equal to $F = (q/c)\,\mathbf{v} \times \mathbf{B}$. (Thus, a particle moving completely perpendicular to the direction of the magnetic field will experience the maximum amount of force, as compared to a particle moving at some angle to the magnetic field. Of course, a particle moving completely parallel to the direction of the magnetic field will experience no force.) This force causes the particle to accelerate; because of the cross-product in the force equation, the acceleration will be perpendicular to the velocity of the particle and will have a magnitude of $qBv_\perp/\gamma mc$. Since we know that accelerating particles radiate, we can use the relativistic expression of Lamor's formula (Eqn. 1.25).

The more likely scenario in astrophysics is when there is a *population* of particles, each moving at a different angle with respect to the magnetic field. To find the total power radiated by this population, we integrate over all possible pitch angles in order to find the average energy loss per particle, see, e.g., Rybicki and Lightman (1979) and Ginzburg and Syrovatskii (1965). This results in the well-known synchrotron energy loss formula:

$$P = \frac{dE}{dt} = \frac{4}{3}\sigma_T c \gamma^2 \beta^2 U_B \tag{1.26}$$

where σ_T is the Thomson cross-section, $\beta = v/c$ gives the particle velocity, γ is the particle's Lorentz factor, and $U_B = B^2/8\pi$ is the energy density of the magnetic field.

In blazars, the radiating particles are typically electrons. Depending on the strength of the magnetic field and the velocity of those seed electrons, the resulting radiation can peak from

anywhere in the radio regime up to X-rays. Thus, this particular emission mechanism may be important in generating the X-ray data we see.

1.4.3 Inverse-Compton Scattering

Inverse-Compton scattering is the process by which an electron scatters off of a photon, imparting energy to the photon and thus boosting it to higher energies; it is capable of accelerating photons up to very high energies, including TeV, thus making it a very important process when it comes to the data collected for this thesis. Blumenthal and Gould (1970) set up the problem thusly: an electron with energy γmc^2 travels through a "gas" of photons. In the scattering that follows, the electrons give up some energy to the photons; in the end, we wish to know what the average energy loss is, which will give clues to the resulting spectrum. Following the derivation in, for example, Rybicki and Lightman (1979), we find that the average power gained per photon is given by:

$$P = \frac{dE}{dt} = \frac{4}{3}\sigma_T c \gamma^2 \beta^2 U_{ph} \tag{1.27}$$

where σ_T is the Thomson cross-section, γ is the electron Lorentz factor, β gives the electron speed, and U_{ph} is the energy density of the photon gas. Note that this formula is almost identical to the analogous formula for synchrotron radiation (see Eqn. 1.26), with the only difference being the energy density variable. Additionally, this expression is only valid in the non-relativistic limit, i.e., when $\sqrt{E_e \times \hbar\omega} \ll m_e c^2$, where E_e is the electron energy, $\hbar\omega$ is the photon energy and $m_e c^2$ is the electron rest energy. The full Compton scatting expression for the cross section that includes the relativistic corrections is called the Klein-Nishina formula (see, for example, Rybicki and Lightman (1979)):

$$\sigma = \sigma_T \frac{3}{4}\left[\frac{1+x}{x^3}\left\{\frac{2x(1+x)}{1+2x} - \ln(1+2x)\right\} + \frac{1}{2x}\ln(1+2x) - \frac{1+3x}{(1+2x)^2}\right] \tag{1.28}$$

where $x \equiv \hbar\omega/m_e c^2$, and where we can see that the cross section decreases with increasing photon energy - thus making collisions less likely. In the non-relativistic limit, the cross section reduces to the Thomson cross section, as we would expect from, for example, Eqn. 1.27.

The spectral energy distributions (SEDs) of blazars are typically characterized by a signature two-bump structure. It is generally agreed that synchrotron radiation is responsible for the lower energy emission observed. There are competing theories for what may generate the higher energy gamma rays, but one of the popular ones is inverse-Compton scattering. The question then becomes, how did the seed photons that are scattered into those higher energies originate? Traditionally, there are two models that describe possible sources for these photons. In Synchrotron-Self Compton models, the seed photons are actually the photons already created by the electrons undergoing synchrotron radiation. In External Compton models, the seed photons originate outside the region - for example, Dermer and Schlickeiser (1994) explore the possibility of the photons coming from the blazar accretion disk. Details of these models can be found in Inoue and Takahara (1996), Fossati et al. (1998) and Ghisellini et al. (1998).

1.4.4 Pion Decay

Up until now, we have discussed leptonic (i.e., electron-based) models for the production of photons. There is one important hadronic (i.e., proton-based) model that can describe the creation of high-energy gamma rays. When a proton with a very high energy collides with a nucleus, there can be a number of products, including neutral pions, π^0. These pions have very short lifetimes (1.78×10^{-16} seconds in the pion's rest frame - see Longair (1992)), decaying quickly into 2 photons. The resulting gamma rays can have energies up to a factor of about 10 less than the original proton energy. (Thus, 10 TeV protons colliding with nuclei can produce gamma rays with about 1 TeV of energy.)

For blazars, such interactions are improbable. However, it is possible for higher energy protons (i.e., $\geq 10^{10}$ eV) can interact with ambient photons to produce pions and ultra high-energy gamma rays. These gamma rays can cascade down to TeV energies via electromagnetic showers (see, for example, the discussion of electromagnetic showers in Chapter 3).

1.4.5 A Note About Lower Energy Emission Processes

The emission processes presented above are by no means an exhaustive list but are likely to account for the bulk of the radiative power of blazars. Additional processes that are generally of interest in astrophysics are bremsstrahlung, which will be important later when we discuss photon-detector techniques, and ionization and other scattering processes. However, because these processes are not of central importance for this thesis, we have decided to not focus on them here.

1.5 High-Energy Photon Propagation Physics

This thesis relies on measurements of photon arrival times. It is therefore important to ask if there are any processes - not related to potential LIV effects - that could affect the propagation of photons and thus arrival time measurements. Luckily, gamma rays and X-rays traversing intergalactic space are typically not vulnerable to other dispersive interactions. At most, we need to be aware of possible absorption processes - though if photons are absorbed, we simply do not see them; this should not affect arrival times. Thus, it is perfectly acceptable to assume that the observed light curves have not changed due to these energy-dependent absorption processes if the flares are achromatic (i.e., if the spectrum of the source does not vary). It is still worthwhile, however, to briefly explore potential absorption processes.

Absorption by interstellar gas can be ignored at energies exceeding a few keV, particularly for gamma rays, as the gas density is too low (as a point of reference, the number density

of particles in galactic interstellar space is roughly 1 particle per cubic centimeter - i.e., extremely low - and the particle density of intergalactic space is even smaller). The only process that may be of some consequence, probably more so for future studies, is electron-positron pair production by high-energy gamma rays interacting with photons from the optical/infrared extragalactic background light. Such effects are more pronounced at high energies.

1.5.1 Pair Production

When a photon has energy at least equal to $2m_e c^2$, it is possible for it to produce an electron-positron pair when it interacts with an ambient photon. This process cannot occur in a vacuum without another particle present to "absorb some of the energy or momentum" (Longair (1992), pg. 118), as energy and momentum cannot be conserved simultaneously without another interacting particle. As discussed in Stecker (2007) and references therein, the ambient photons from the Cosmic Microwave Background would make the universe "opaque to gamma rays of energy above 100 TeV at extragalactic distances". We thus expect to see some kind of cut-off in extragalactic source spectra at TeV energies. Even more interestingly, given a source at redshift z, photons above an energy given by $\sim 100(1+z)^{-2}$ TeV should not be seen on Earth (Stecker (2007)); thus, the farther away a source is, the lower the energy of the location of the cut-off. It is for this reason that probing high-TeV energies from distant extragalactic sources is so difficult.

Far more important to the discussion of photon absorption is the role of the Extragalactic Background Light (EBL), because it affects gamma rays of lower energies (i.e., those on the order of 1 TeV, as pointed out in Stecker et al. (1992)). Primack et al. (2005) discuss the fact that collisions between gamma rays and the EBL constitute the main process by which gamma rays are absorbed as they traverse from source to observer, and such collisions should result in a cut-off in the observed spectrum of a gamma-ray source. Studies and

modeling of the EBL and its evolution are very important to high-energy observatories (such as the ground-based VERITAS, used for part of this thesis - see Chapter 3) as they provide information about interactions gamma rays experience between emission and observation, and thus about the shape and behavior of observed spectra and light curves. See, for example, Primack et al. (2005) for their modeling work. Furthermore, observations of sources at TeV energies can provide methods for probing the EBL in ways not previously possible - see, for example, Stecker et al. (1992)

The LIV analysis, the details of which are described in Chapter 2, uses photons from Mrk 421. For the redshift of the source and the energy range under consideration (mostly from 100 GeV to 5 TeV), EBL absorption can be neglected.

1.6 The Fourier Transform

Before we move onto a discussion of the specific methods used in the next chapter, it is worthwhile to briefly introduce one important tool that will be used in the DCF analysis - the Fourier transform. Any continuous time-dependent signal or function may be decomposed into Fourier components, which provide information about the power spectrum and phases. A basic Fourier transform works by transforming the starting function from time-space to frequency-space. Then, in order to recover the original function, we apply the inverse-Fourier transform. The definition of these transforms are:

$$H(\omega) = \int_{-\infty}^{\infty} h(t) e^{i\omega t} dt \tag{1.29}$$

$$h(t) = \frac{1}{2\pi} \int_{-\infty}^{\infty} H(\omega) e^{-i\omega t} d\omega \tag{1.30}$$

where $h(t)$ is the original function in time-space, and $H(\omega)$ is that function's Fourier trans-

form - i.e., the original function in frequency-space. As an example, we can briefly examine what happens to a simple function: $A\sin(\omega_o t) + d$, where A is the function amplitude, the frequency is ω_o, and d is an offset. Knowing that $\sin(\omega_o t)$ may be written as $\frac{1}{2i}(e^{i\omega_o t} - e^{-i\omega_o t})$, its Fourier transform becomes:

$$H(\omega) = A\frac{\pi}{i}\big(\delta(\omega_o - \omega) - \delta(\omega_o + \omega)\big) - d\delta(\omega) \tag{1.31}$$

Note that our original function is simply a sine wave superimposed with a constant function, d. Thus, the Fourier transform contains superimposed information from both terms. The first two delta function terms in the Fourier tranform correspond to the sine function; they show two "spikes" located at frequencies ω_o and $-\omega_o$ - i.e., at our known frequency. The third delta function term corresponds to the offset and indicates that there is information imbedded at the 0 frequency - as one would expect with a constant function, where there is no oscillatory behavior. This last bit therefore constitutes the offset information of the original function.

Chapter 2

Analysis Methods

2.1 Lorentz Invariance Violation

The ultimate goal of this study is to constrain the energy level at which the violation of Lorentz symmetry becomes observable. The cosmological foundation for such arguments was presented in Chapter 1. To this end, we start by constraining energy-dependent propagation by finding time delays in light curves, which are independent of quantum gravitational considerations. These delays can then interpreted as the upper limits on the maximum level of dispersion, and thus related to the minimum energy at which the effects of LIV may be seen.

The first step is to construct an experimental search for evidence of energy-dependent time delays in radiation propagation. There are a number of different methods, each with their own strengths and weaknesses. We have relied on the DisCan – "dispersion cancellation" – method (Scargle et al. (2008)), which was the method used by Abdo et al. (2009a) to derive the best published LIV constraints. Additional details about how they applied the DisCan method to astrophysical data, and the theoretical underpinnings of the work, can be found in that paper and its supplemental materials. That work formed the basis for the analysis presented in this thesis.

2.1.1 Dispersion Cancellation - The Method

In this method, we assume that any dispersion introduced, by LIV or any other hypothetical effect, essentially "smears out" the profile of the emitted light curve. The result would be the broadening of any peaks in the original emission and the spreading out of the general time span of the light curve. Experimental tests look for the most plausible mathematical form of the dispersion; in principle, this would be one that, when removed, would result in a tighter, more strongly peaked light curve. For such a test, an ideal data set would be one in which we can safely assume that radiation was emitted achromatically, and one that has a fair amount of strongly peaked structure.

As discussed in Chapter 1, if we assume that the leading order correction to the energy-independent dispersion relation is either linear or quadratic, we can write the subsequent time-delay dispersion models in terms of a free parameter, θ. We thus obtain time-delay expressions in either linear (n=1, in the language developed in Chapter 1) or quadratic forms (n=2):

$$\textbf{Linear: } t_i' = t_i^{obs} - \theta(E_i^{obs} - E_{avg}) \tag{2.1}$$

$$\textbf{Quadratic: } t_i' = t_i^{obs} - \theta((E_i^{obs})^2 - (E^2)_{avg}) \tag{2.2}$$

where t_i^{obs} is the observed arrival time of a photon, denoted i, from some astrophysical source, t_i' is the time at which that photon *would* have arrived were it not for the dispersive effect, E_i^{obs} is the observed energy of that photon, and E_{avg} is the average energy of the observed light curve. (Note - we have added the E_{avg} for proper scaling.) Dimensional analysis shows that θ will have units of sec/GeV in the linear model, and units of sec/GeV^2 in the quadratic

model. A finding of $\theta > 0$ indicates the sub-luminal case, i.e. the positive delay, where high-energy photons theoretically arrive later than they would have without a dispersive influence. Conversely, a finding of $\theta < 0$ indicates the super-luminal case, i.e. the negative delay, such that photons theoretically arrive earlier than they would have without a dispersive influence.

Note that, in the context of LIV, we can very easily relate this parameter θ to our original parameter ξ_n by returning to Eqn. 1.5. In the linear and quadratic formulations, the magnitude of θ is simply:

$$\textbf{Linear: } |\theta| = \frac{1}{H_0}\frac{1}{\xi_1 E_{pl}}\int_0^z \frac{(1+z')\,dz'}{\sqrt{\Omega_\Lambda + \Omega_m(1+z')^3}} \tag{2.3}$$

$$\textbf{Quadratic: } |\theta| = \frac{3}{2H_0}\Big(\frac{1}{\xi_2 E_{pl}}\Big)^2\int_0^z \frac{(1+z')^2\,dz'}{\sqrt{\Omega_\Lambda + \Omega_m(1+z')^3}} \tag{2.4}$$

where for ξ, a subscript of "1" corresponds to the value for the linear model, and a subscript of "2" corresponds to the value for the quadratic model.

Constraining this θ becomes straightforward; the procedure is the same for both the linear and quadratic models. After obtaining a light curve from a distant (preferably extragalactic) astrophysical source (the farther away the better, to allow for the maximum build up of propagation effects), we assume that the source radiation was emitted achromatically; LIV propagation effects should then "smear out" the radiation profile, resulting in an observed light curve which is wider than the emitted one - even when correcting for cosmological time dilation. Assuming no other source for any potentially observed delay, Eqn. 2.1 and Eqn. 2.2 should provide a formulation for roughly canceling out the energy dependent propagation effects using the linear and quadratic models, respectively, thus leaving the desired tighter time profile - i.e., the time profile we would expect to see were it not for dispersive effects.

Theoretically, θ can be any value from $-\infty$ to $+\infty$. However, exceptionally large values of $|\theta|$ would shift the event list into times that are well outside the observation time range, which is not physically realistic. We can instead look at θ's within a window based on the time frame of the observed event list. For example, we can define a $\theta_{max}^{window} \approx (t_{last}^{obs} - t_{first}^{obs})/(500\text{GeV})$, where the 500 GeV scales the value roughly according to observed energies, and a $\theta_{min}^{window} = -\theta_{max}^{window}$.

For each θ that we sample within this range, we have a new event list that must be evaluated in some manner. We use an entropy-minimization method to determine which θ gives the new event list that most likely resembles what the radiation time profile would have looked like without the dispersion effect. Entropy, of course, has the useful property that it is minimized when events are "squeezed" together in time as closely as possible. This property lets us use entropy as a cost function in order to evaluate each new event list. Thus, we bin each new event list and calculate the Shannon entropy according to:

$$S = -\sum_k p_k \ln p_k \tag{2.5}$$

where $p_k \equiv n_k/N$ is simply the fraction of the total events that fall within the k-th bin (Abdo et al. (2009a)). We evenly sample a selection of θ's between the window's maximum and minimum θ values and calculate the entropy associated with that θ to arrive at plot of entropy versus θ. From this plot we ascertain which θ yields the smallest value of entropy, and this becomes the experimental θ_{min} – i.e., the θ that minimizes the Shannon entropy. To fine-tune that value, we then conduct several additional iterations, with each one zooming into finer θ scales with the previous θ_{min} at the center of the new range.

2.1.2 Important Binning Details

A major strength of this method is that it does not require us to bin our light curve in energy. Instead, we work with individual events characterized by their arrival times and reconstructed

energy. However, we do need to bin the light curves in time in order to calculate the entropy cost function. Unfortunately, binning data always involves some loss of information (in this case, the exact time of events) and some arbitrariness (in this case, the start of the first bin and the bin width). We are not aware of the existence of any method for evaluating LIV dispersion effects that does not rely on binning.

The size of the bins should take into account our knowledge about blazar flares. The bin size should not be so large that it washes out peaks and flares in the light curve structure, and it should not be so small that each bin would only contain a few counts. A bin width of sixty seconds turns out to provide a fair balance between these two concerns for the present data set. Blazars have been known to exhibit variability down the minute time scale, so a 60 second binsize should capture intricate light curve structure without being too small. Since we have dictated how large in time the bins will be, the *number* of bins required to cover each shifted event list depends solely on how much time that shifted event list spans.

The relative value of the entropy parameter depends on the temporal concentration of the flare at the source, along with the the choice of bin width and thus the number of bins and the number of events that fall within each bin. For now, let us consider what effect the number of bins has on entropy. When events are more closely packed in time, fewer bins are needed and the entropy is naturally smaller. As the θ steps become smaller and smaller, this can lead to what initially may appear to be jump discontinuities in the entropy versus θ plots. A good example can be seen in the top panel of Fig. 2.1.

In reality, these sudden jumps or drops in entropy are byproducts of binning. When the θ steps were larger, the shifted event lists between each pair of adjacent test θ's were different enough that each required its own number of bins. "Discontinuities" would not have been visible. When we probe smaller scales, however, the difference between two adjacent θ's

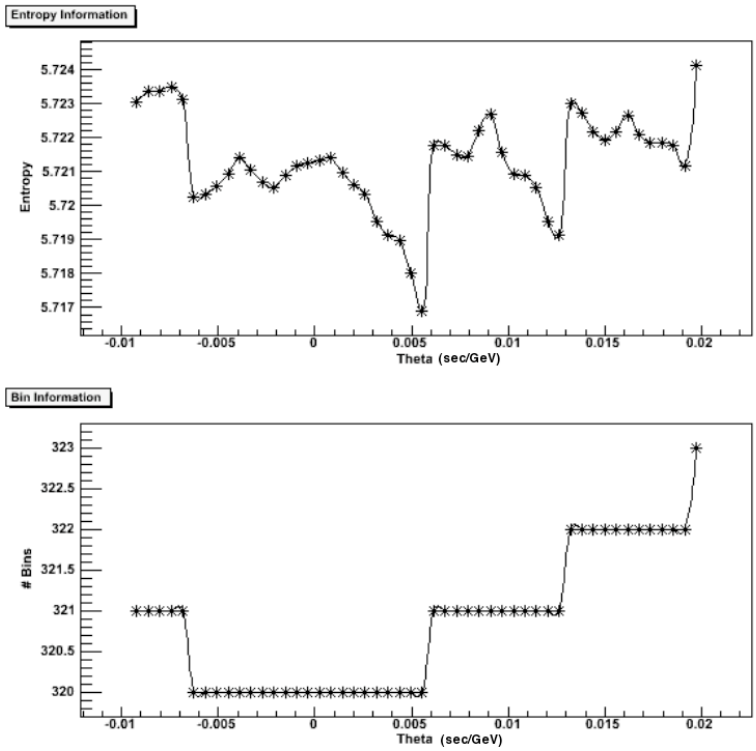

Figure 2.1: A comparison of entropy versus θ to the number of bins per test theta.

becomes quite small, i.e., on the the order of 0.001 or even 0.0001 and the manner in which each individual test θ shifts around the events are no longer so different. Several adjacent test θ's may actually need the same number of bins, and thus their different values of entropy depend only on small variations in the number of events in each bin. Occasionally, though, there reaches a point were the shifted event list has changed just enough from one test θ to the next that either an additional bin is needed to handle event spill-over, or an extra bin is no longer needed. This change adds an additional "variable" in the entropy calculations, resulting in what appears as a jump. To illustrate this, we plot an example entropy versus θ plot on top of a graph of the number of bins per each test θ (see Fig.2.1). We see clearly that each bin jump corresponds to a sudden change in the number of bins required.

As we continue zooming into finer scales, we should see less of this effect. We can use this as a guide to tell us when we have zoomed in far enough and homed in on the θ that has appropriately minimized entropy.

Ways to Minimize the Discontinuity in the Entropy Curve

One way we found to minimize the effect and appearance of discontinuities in the entropy curve was by simply excluding the 1st and last bins when calculating entropy. These bins generally had only a few events each. Recall the definition of the Shannon entropy from Eqn. 2.5:

$$S = -\sum_k p_k \ln p_k \tag{2.6}$$

Of course, each bin's p_k, which is defined as the number of entries in that bin divided by the total number of events, will have a value somewhere between 0 and 1. The smaller the value, the more negative its natural logarithm will be (hence the overall negative sign serves to force a positive value for entropy). For those bins that have only a few entries, generally the outlier bins, $\ln p_k$ will be disproportionately large and will throw off the entropy calculation. This

becomes especially problematic between the test θ's where the discontinuities occur, since those are when the outlier bins tend to be less populated. We found that simply excluding these bins in all cases helped to reduce the discontinuities. In that vein, we also excluded bins that had *no* entries.

2.1.3 LIV Simulations

The final result from the dispersion analysis is the θ that minimized the entropy cost function. Once this has been found, it can be interpreted in the quantum gravity framework, as will be done in Chapter 4. In order to test the statistical significance of that result, we needed to execute a Monte Carlo simulation. This was done by generating a large number of random event lists (usually 1,000), and performing the DisCan analysis method on each one to find the entropy-minimizing θ, each called θ_{min}. The θ_{min}'s were then collected into a histogram, and the experimental results compared to the distribution, which will be discussed in Chapter 4.

The random events lists were generated by fixing the time values and scrambling the energy values around with respect to the time points. Doing so created a new, randomized distribution of energy as a function of time that could then be evaluated using the DisCan method.

2.2 Discrete Correlation Function

2.2.1 The Discrete Correlation Function

In experimental scenarios, data sets are usually comprised of unevenly sampled individual events, rendering the cross-correlation function (Eqn. 1.23) no longer applicable, as the cross-correlation function assumes that data has been evenly sampled. Astrophysical data is generally not evenly sampled. Observational instruments (ground-based telescopes and

space-borne satellites) generally must contend with the visibility of the source, and with competition with other visible sources, leading to gaps in data; additionally, particularly in the case of ground-based instruments, weather changes, hardware/software problems, and even the rising of the sun, all conspire to produce unevenly sampled data sets. Mathematically, we need a way to compare data sets regardless of the irregularities of the time-sampling. This way comes in the form of the discrete correlation function (DCF), as proposed and discussed in Edelson and Krolik (1988). A good use of the DCF being applied to gamma-ray data can be found, for example, in Jordan (2004); there, the author applied the DCF to Mrk 421 flare data collected from March 18th to April 1st, 2001, using TeV gamma-ray data from the Whipple Observatory and keV X-ray data from the RXTE satellite.

Suppose we have two sets of measured fluxes, $\{a_i\}$ and $\{b_j\}$. We can then define an "unbinned" correlation factor, $UDCF_{ij}$, for each possible pair of measurements from the two data sets:

$$UDCF_{ij} = \frac{(a_i - \bar{a})(b_j - \bar{b})}{\sqrt{(\sigma_a^2 - e_a^2)(\sigma_b^2 - e_b^2)}} \tag{2.7}$$

where $\bar{a}$ and $\bar{b}$ are the averages of each data set, e_a and e_b are each data set's mean measurement error, and the denominator normalizes the expression. As usual, σ_a and σ_b are the standard deviations for each data set, defined here as, for example,

$$\sigma_a = \sqrt{\frac{\Sigma(a_i - \bar{a})^2}{N - 1}} \tag{2.8}$$

for data set $\{a_i\}$. If there are N_1 data points in set $\{a_i\}$ and N_2 data points in set $\{b_j\}$, then there are $N_1 \times N_2$ pairs of data points, and thus $N_1 \times N_2$ UDCF values. For each pair of data points, there is an associated time lag $\Delta t_{ij} = t_j - t_i$, with t_i and t_j being the times of the flux measurements a_i and b_j, respectively.

We can then bin the $UDCF_{ij}$'s according to their corresponding Δt_{ij}'s, and calculate the average UDCF in each bin:

$$DCF(\tau) = \frac{1}{M} \sum UDCF_{ij} \tag{2.9}$$

where M is the number of pairs with a time lag Δt_{ij} falling into the bin defined as $\tau - \Delta\tau/2 < t_{ij} < \tau + \Delta\tau/2$, where τ is the representative time lag for each bin (and is the center value of the bin) and $\Delta\tau$ is the width of that bin. Recalling our discussion of time series analysis in Chapter 1, for uncorrelated time series we expect DCF values close to zero. DCF values close to +1 or -1 indicate a linear correlation or anti-correlation, respectively. If there is a linear correlation between the two time series for a time lag τ_{true}, then we expect that it will give rise to a large DCF value close to 1 at a time lag τ close to τ_{true}. This analysis searches for the largest positive DCF (which we are denoting DCF_{max}) as a function of τ. We are denoting the τ that corresponds to the largest positive DCF as τ_{max}, which we are taking as the best guess for the true time lag.

As described below, to assess the statistical significance of DCF values obtained for experimental data, we performed Monte Carlo simulations. However, it is still worthwhile to assign error bars to the DCF results. Edelson and Krolik (1988) developed an error on the DCF to be:

$$DCF(\tau)_{error} = \frac{1}{M-1} \left\{ \sum \left[UDCF_{ij} - DCF(\tau) \right]^2 \right\}^{1/2} \tag{2.10}$$

We have used this formula in assigning error bars to our experimental DCFs. However, as discussed in Jordan (2004), the errors come with a caveat, since the DCFs, and by extension the error on the DCF, cannot be considered "independent"; this comes from the fact that each data point may fall into more than one DCF bin.

"Time Lag" Meaning

In practice, we compare two light curves from the same source from the same time period. (An example of two light curves are the Fermi gamma-ray and Swift X-ray light curves for a flaring episode from the blazar 3C 454.3. These will be discussed in detail in later chapters.) The more evenly sampled light curve (usually Fermi data) is designated "light curve #1"; the other is designated "light curve #2". We then find the time lag (i.e., the τ) that gives the largest DCF value. These (DCF_{max} and τ_{max}) become our experimental values. It is important to note, though, precisely what we mean by "time lag". We have already shown that the time lag, τ, acts as a representative of the Δt's within its bin - in other words, a representative of the differences in times between each pair of data points within that bin. Each Δt is defined as the time from the first light curve subtracted off the time from the second light curve (i.e., $t_2 - t_1$). Thus, all time lags are a measure of the first light curve with respect to the second light curve. When we speak of a time lag of, for example, 60 days, we are comparing events in light curve 1 that occurred 60 days *prior* to events in light curve 2. Similarly, a time lag of -60 days indicates a comparison of events in light curve 1 that occurred 60 days *after* events in light curve 2.

2.2.2 Improvements to the Standard DCF Analysis

We improved the standard DCF analysis in two ways. First, we restricted the range of considered τ values to ensure that there was a sufficiently large number of $UDCF_{ij}$'s in each τ-bin. We did so by constructing a window that encompasses one-half of all of the τ's; specifically, if we denote the smallest of the time lags as τ_{small} and the largest of the time lags as τ_{large}, then we only consider those time lags that fall within the window $\tau_{small}/2 < \tau < \tau_{large}/2$.

Second, for each τ-bin, when calculating the $UDCF_{ij}$'s according to Eqn. 2.7, we used only the a_i's and b_j's that contribute to that particular bin for the values of $\bar{a}$, $\bar{b}$, σ_a, and σ_b; this

was instead of using $\bar{a}$, $\bar{b}$, σ_a, and σ_b calculated for each entire data set. This helps to ensure that flaring behavior that may be present in one part of a light curve will not influence the non-flaring behavior in other parts of the light curve. Not doing this may result in a contamination of bins that represent different parts of the light curves, resulting in DCFs that are larger than $[-1, +1]$.

2.2.3 DCF Simulations

To investigate the statistical significance of the basic experimental result (the time lag, τ_{max}, that produces the largest DCF), we performed a Monte Carlo simulation. The basic method is simple: obtain a random light curve based on light curve #1 and repeat the DCF analysis between the random light curve and light curve #2 in order to find the largest DCF. Note that we only need to generate a random light curve based on *one* of the light curves (preferably the one that is more evenly sampled - this reasoning will become apparent shortly when we return to *how* to generate a random light curve). Because we are testing the strength of the relationship between our two original light curves, we need to preserve one of them so that our resulting simulations still hold some physical resemblance to the experimental result. Thus, we retain one light curve and build a random light curve based on the properties of the other one. Once this process has been done multiple times (usually 10,000), we go through and count how many DCF_{max}-values are larger than the experimental one. This allows us to calculate the chance probability, P, that, in the absence of any linear correlation - i.e., owing strictly to pure chance - we could observe DCF values as large or larger than the one found in the experimental data set:

$$P = \frac{\#\ DCFs\ larger}{\#\ of\ trials} = \frac{N'}{N} \tag{2.11}$$

The chance probability gives us a measure of the likelihood of the experimental DCF being due simply to statistical fluctuations; the higher the chance probability, the less significant our experimental result. We calculate the error on the chance probability by using the Poisson

error on N' such that:

$$P_{err} = \frac{\sqrt{N'}}{N} \tag{2.12}$$

The error on the chance probability holds additional information that we can use when building our simulation - we can gain insight into whether we are using a large enough number of trials in the simulation. We want the error to be less than 10% of the actual chance probability - i.e., we want $\frac{\sqrt{N'}}{N}/P < 0.1$. This indicates that we want N' (the number of DCFs found to be greater than the experimental value) to be more than 100. If we see this, we are doing enough trials. If not, we need to redo the simulation with a larger number of trials. Note that this method of error estimation only works when we want our chance probability, P, to be small. If we wanted P to be large (~ 0.99), then we'd be using N-N' instead of N'. If we wanted an intermediate value of P, we'd have to resort to using a more complicated expression based on the statistics for a binomial distribution.

2.2.4 Generating Random Light Curves

Unfortunately, the generation of random light curves is not always straight forward. The main concern when generating these simulated light curves is that they have the same temporal structure as the original light curve. More precisely, the fluxes should vary on the same temporal time scales - or, put another way, the simulated light curves and the original light curves should all have a similar Fourier power spectra. Simply scrambling the fluxes to obtain a random sampling of fluxes as a function of time could produce variability on time scales that are not physically possible. There are a number of ways to produce physical synthetic light curves. For example, in Jordan (2004), light curves were generated by the pile-up of flares with rise and fall times comparable to data.

Here, we rely on a different, less subjective approach to simulating light curves than the use of the pile-up of flares. We base the light curve generation on a Fourier decomposition of the

original light curve. The simplest way to reproduce similar Fourier power spectra between the original light curve and the simulated one is to work in the frequency domain; we Fourier transform the original light curve, then multiply each Fourier coefficient by a random phase, $2\pi\phi$, where ϕ can take on any value such that $0 \leq \phi \leq 1$ - i.e., we "scramble the phase" of each point. We then inverse-Fourier transform to obtain the simulated light curve in the usual time domain.

In order to execute this procedure, we must use a light curve that is evenly sampled as the basis for the random one, since a discrete Fourier transform assumes that the spacings between each data point are consistent; we will call this spacing δt. For a set of flux values, $\{a_k\}$, containing N_1 number of points and a spacing of δt between each time value, the discrete Fourier transform follows from the continuous time transform by making the substitutions $t \rightarrow t_k = k \times \delta t$ and $f \rightarrow f_n = n \times 1/T$, where $T = N_1 \times \delta t$. We then have a form for the discrete Fourier transform:

$$f_n = \frac{n}{N_1 \times \delta t} \tag{2.13}$$

$$H_n = \sum_{k=0}^{N_1-1} a_k e^{i2\pi kn/N_1} \tag{2.14}$$

$$= \sum_{k=0}^{N_1-1} a_k [\cos(2\pi kn/N_1) + i \sin(2\pi kn/N_1)] \tag{2.15}$$

where f_n is the Fourier frequency and H_n are the Fourier transform coefficients of the set $\{a_k\}$. Note that we use the index n such that $0 \leq n \leq (N_1 - 1)$ so that there are the requisite N_1 number of data points in Fourier space. Also notice that for each individual Fourier point, we must sum over all of the actual flux data points.

The simulated Fourier transform coefficients are then generated by combining the Fourier

coefficients with random phases, $2\pi\phi$:

$$H_{n,\,random} = H_n \times e^{i2\pi\phi} = H_n \times [\cos(2\pi\phi) + i\sin(2\pi\phi)] \tag{2.16}$$

If we explicitly break this down into the real and imaginary components, we have:

$$H^{real}_{n,\,random} = \sum_{k=0}^{N_1-1} h_k \big[\cos(2\pi kn/N_1) \times \cos(2\pi\phi) - \sin(2\pi kn/N_1) \times \sin(2\pi\phi)\big] \tag{2.17}$$

$$H^{imag}_{n,\,random} = \sum_{k=0}^{N_1-1} h_k \big[\cos(2\pi kn/N_1) \times \sin(2\pi\phi) + \sin(2\pi kn/N_1) \times \cos(2\pi\phi)\big] \tag{2.18}$$

It is worth noting that thus far we have used the convention of $0 \leq n \leq (N-1)$ for simplicity in coding. Often, however, the convention $-(N/2) \leq n \leq (N/2)$ is used to emphasize symmetry properties between positive and negative frequencies; for that reason we will denote that method the "symmetric" scheme. This is purely a stylistic difference and does not affect any of the mathematics (though of course it is important to keep track of the scheme being used). However, we can use the properties of the symmetric scheme to classify when a function is real. In Fourier space, a function is real when $a(-f) = a^*(f)$, where the * denotes the complex conjugate. In other words, the positive and negative frequency pairs of the *real* components must be equal in magnitude and in sign, while the positive and negative frequency pairs of the *imaginary* components must be equal in magnitude and opposite in sign.

We have assured that the simulated light curves are real by noting that the positive frequencies correspond to $1 \leq n \leq (N_1/2 - 1)$ and the negative frequencies correspond to $(N_1/2 + 1) \leq n \leq (N_1 - 1)$. The value $n = N_1/2$ is special and corresponds to both the positive and negative limits on the frequency. To ensure our resulting simulated light curve is real, we must "phase-scramble" all points that correspond to $1 \leq n \leq (N_1/2 - 1)$ (i.e., all the "positive" frequency points). We then set the real components of the "negative" fre-

quencies - those that correspond to $(N_1/2+1) \leq n \leq (N_1-1)$ - equal in magnitude and sign to their symmetric, positive frequency counterparts, and the imaginary components equal in magnitude yet *opposite* in sign to their symmetric, positive frequency counterparts. The imaginary component of the point corresponding to the special value $n = N_1/2$ must be set to 0. Refer to Fig. 2.2 for a cartoon of the conditions that ensure real light curves.

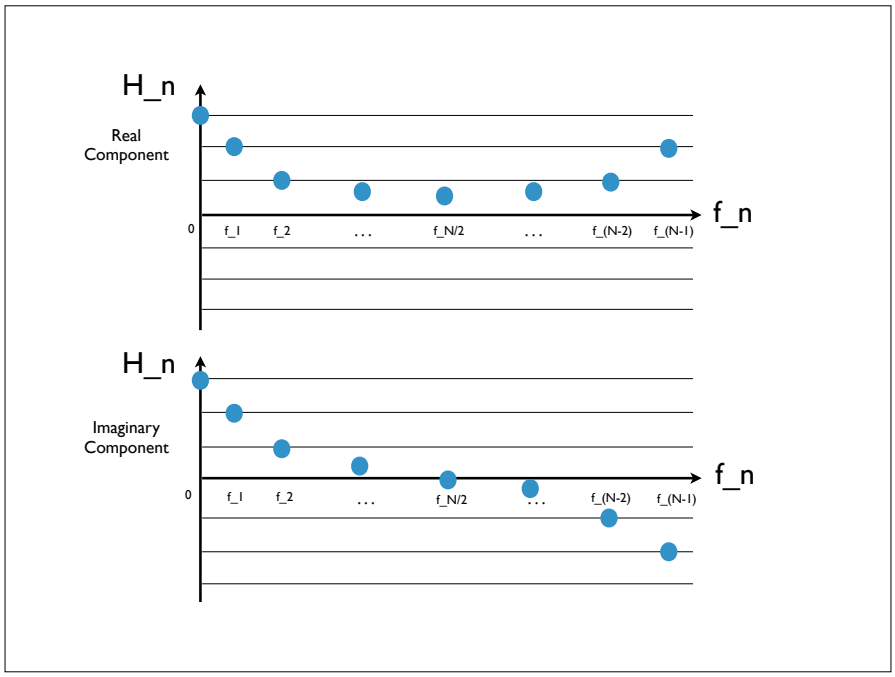

Figure 2.2: Cartoon of the conditions that ensure real light curves in Fourier space.

So far, we have not discussed the "center" frequency point - the one that corresponds to $n = 0$ in our scheme. This point represents the zero frequency Fourier point, and thus contains any information embedded within the original light curve that does not have oscillatory behavior; in other words, this is where any baseline (or offset) flux information is stored. Although the presence of offset information ultimately does not matter for the purposes of this analysis - inspection of Eq. 2.7 shows that all that matters is the flux data *with respect to its mean* - it is still worthwhile to preserve offset information in order to obtain physical-looking random light curves. This is done by simply not altering that particular point in the phase-scrambling

process.

Once we have calculated the real and imaginary components of the random light curve's Fourier points, all we need to do is execute the inverse-discrete Fourier transform in order to obtain the random light curve in the usual time domain:

$$a_{k,\,random} = \frac{1}{N_1} \sum_{n=0}^{N_1-1} H_n e^{-i2\pi kn/N_1} \tag{2.19}$$

In component form, this is a rather cumbersome set of equations:

$$a^{real}_{k,\,random} = \frac{1}{N_1} \sum_{n=0}^{N_1-1} H^{real}_{n,\,random} \times \cos(2\pi kn/N_1) + H^{imag}_{n,\,random} \times \sin(2\pi kn/N_1) \tag{2.20}$$

$$a^{imag}_{k,\,random} = \frac{1}{N_1} \sum_{n=0}^{N_1-1} -H^{real}_{n,\,random} \times \sin(2\pi kn/N_1) + H^{imag}_{n,\,random} \times \cos(2\pi kn/N_1) \tag{2.21}$$

We can then proceed with the rest of the simulation as described above.

For illustrative purposes, Fig. 2.3 shows examples of two simulated light curves (the top two panels) generated using the method described. These examples were compiled from the actual DCF analysis for the blazar 3C 273 (see Ch. 4) using gamma-ray data from the Fermi satellite (see Ch. 3). For comparison, the real light curve is shown in the bottom panel of the figure. As can be seen, the flux values for the simulated light curves may be negative. Although this is not necessarily unphysical (in practice, flux may be negative if the background flux exceeds the source flux), for the purposes of the DCF analysis, the *relative* values of the flux with respect to the mean flux is of more relevance than the actual flux values.

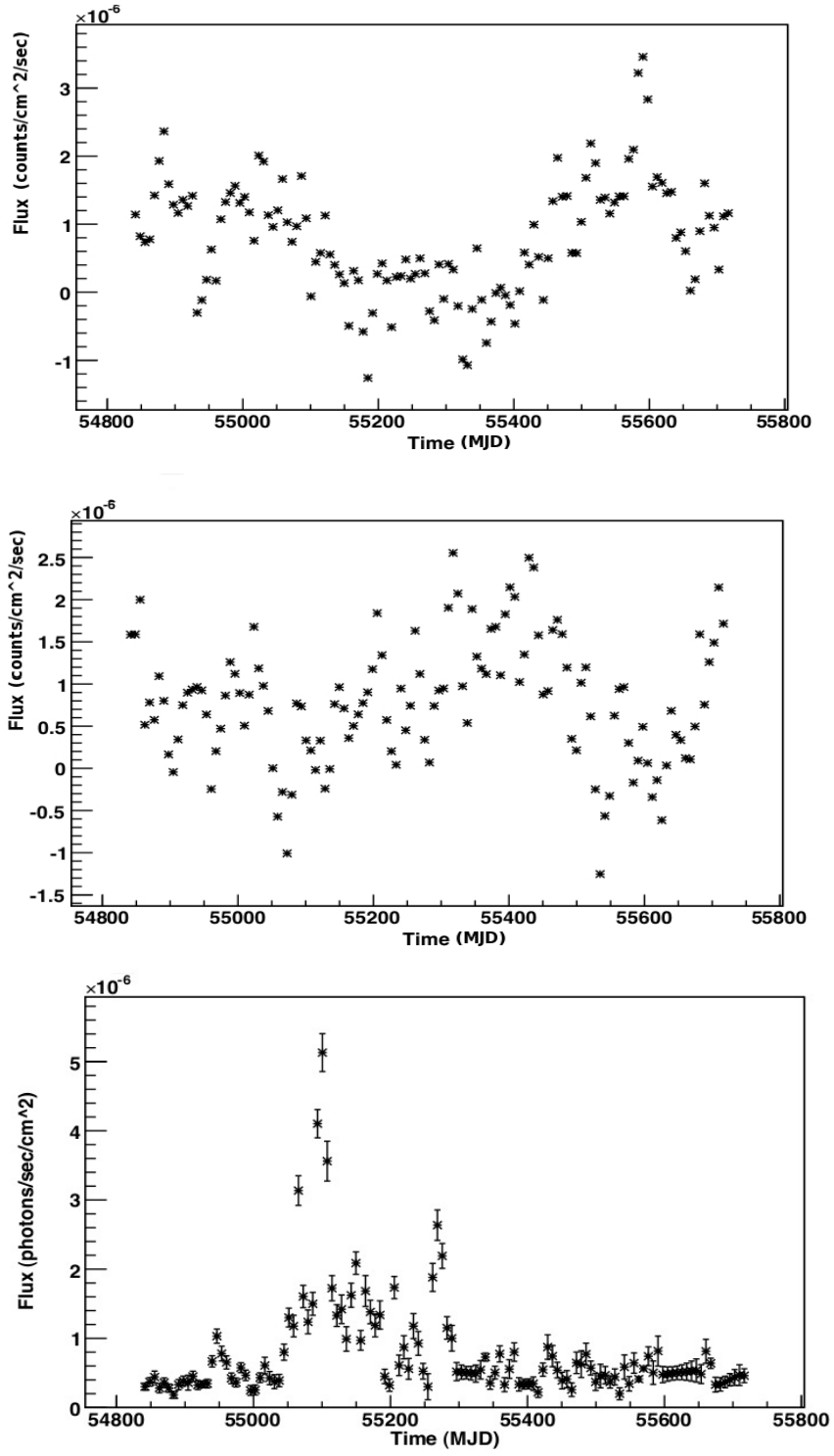

Figure 2.3: Examples of simulated light curves generated using real data from Fermi observations of the blazar 3C 273 (see Ch. 3 for more details about the Fermi gamma-ray satellite, and Ch. 4 for more details about 3C 273 and its data). The **top two panels** are the simulated lightcurves, and for comparison the **bottom panel** is the actual light curve.

Chapter 3

Data Collection

For the purposes of the work presented in this thesis, we have relied on three instruments for data collection: VERITAS (a very high-energy gamma-ray observatory), Fermi (a gamma-ray satellite covering roughly the 100 MeV to 10 GeV energy regime), and Swift (an X-ray satellite). In this chapter, we will discuss each of those instruments, including the physics of how they function and collect data, and the ways we found were best to handle the data once it was taken. For an overview of which subset of multi-wavelength data was used for each study, we have:

- **Lorentz Invariance Violation:** Since the best test of LIV comes from using data that probes very high energies, it was best to use an instrument that is capable of detecting TeV photons. For that we used the VERITAS gamma-ray telescope array. Much of this chapter will be devoted to discussing how VERITAS works, starting with considerations of what happens to a photon when it interacts with the Earth's atmosphere. We will then move onto a discussion of VERITAS itself, and later the specific data set we used.

- **Discrete Correlation Function:** In order to compare contemporaneous data sets from two energy bands for a multitude of sources, we relied on the Fermi Gamma-Ray Space Telescope and the Swift Telescope. The latter part of this chapter focuses on

those two instruments and the best ways to handle their data.

3.1 The Detection of a Photon

A full understanding on the mechanics of ground-based TeV astronomy requires a good understanding of what happens to a photon from the time it hits the Earth's atmosphere until the time the ground-based instrument recognizes such an event has occurred. We will consider a photon of some energy, denoted E_0, incident on Earth's atmosphere. Depending on the specific value of its energy, this photon will either penetrate to the ground (allowing it to be directly detected by ground-based instruments), be completely absorbed, or initiate some kind of reaction (with particle by-products that can then be observed by ground-based instruments). Fig. 3.1 shows the penetrating depths of photons with energies across the electromagnetic spectrum. Study of this figure reveals immediately that a photon whose energy is in the high-energy range - ie, MeV or higher - will not penetrate directly to the ground. Instead, ground-based instruments must rely on detecting the products of the resulting electromagnetic shower these high-energy photons initiate.

3.1.1 Electromagnetic Showers

As described in Chapter 1, a photon with an energy E_0 that is greater than $2m_ec^2$ incident upon a non-vacuum medium such as the Earth's atmosphere will produce an electron-positron pair, each with energy equal to approximately half of the original photon energy ($E_0/2$). In this instance, it is pair producing with the assistance of the nuclei of the atoms of the atmosphere. In one radiation length, each of these resulting particles will lose about half of its energy via emission of a bremsstrahlung gamma ray. Bremsstrahlung is the mechanism by which a particle radiates as it is accelerated by the electric field of another particle. In the case of electromagnetic showers, the pair-produced electrons or positrons radiate when they impinge on either ions or the nuclei of an atom in the Earth's atmosphere. The physics gov-

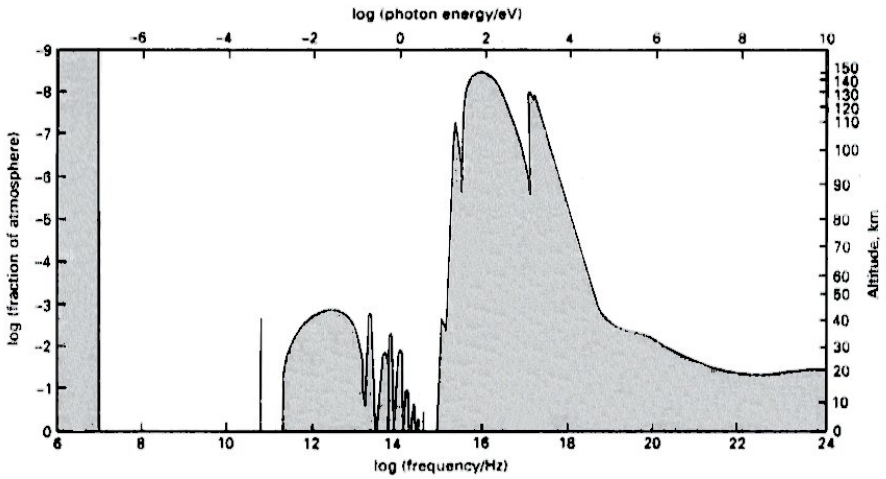

Figure 3.1: Penetration depths through the Earth's atmosphere for photons with energies across the electromagnetic spectrum. For each photon energy, the white area corresponds to the altitudes at which the atmosphere is transparent to that particular energy, while the shaded region corresponds to altitudes at which the atmosphere is opaque to that particular energy. From Longair (1992), pg. 19.

erning bremsstrahlung can be fairly complicated. (For in-depth reviews, please see Rybicki and Lightman (1979) or Blumenthal and Gould (1970).)

To first approximation, in each radiation length traversed by an electron or a positron, the number of particles will double, due to the creation of a gamma ray via bremsstrahlung; similarly, in each radiation length traversed by a gamma ray, the number of particles will double through the production of an electron-positron pair. The overall effect is that the number of particles in the shower will have doubled with each path length. The energy of the original incident photon will thus be spread across this expanding shower of photons and electron-positron pairs until the electrons/positrons each reach a critical energy, E_c - the value of which is dependent on the medium through which the particles are traveling - at which point the particles no longer have enough energy to undergo bremsstrahlung and thus their energy losses are due mainly to ionization. This point denotes the shower maximum, where there is the largest amount of particles present, after which the electromagnetic shower will rapidly die out. Please refer to Fig. 3.2 for an illustration of this process. An important

point is that because both pair production and bremsstrahlung have the same radiation length in this energy regime, each stage of the shower develops along the same time scales and thus at the same height from the ground.

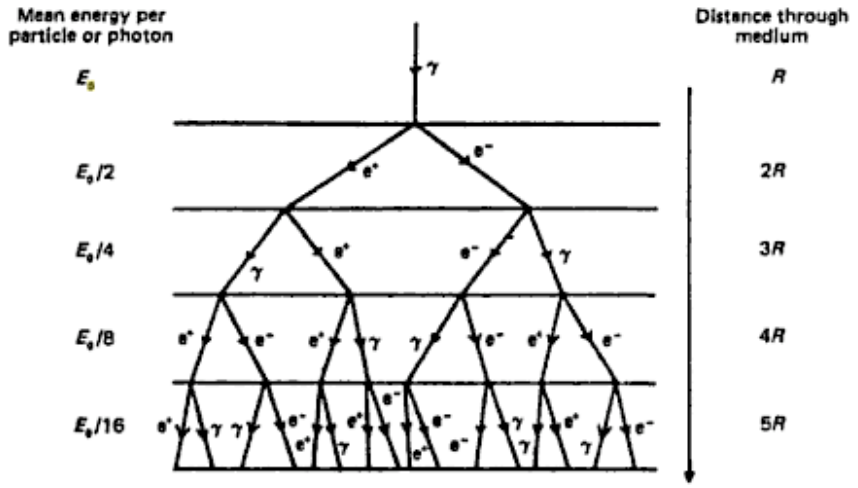

Figure 3.2: Schematic of the development of an electromagnetic shower. From Longair (1992), pg. 120.

3.1.2 Cherenkov Radiation

When a particle is moving with a uniform speed, v_{part}, through a medium with an index of refraction given by n, typically no detectable radiation is emitted. However, in the case when the particle is moving fast enough, radiation, named Cherenkov radiation after one of its discoverers, Pavel Alekseevich Cherenkov, is observable. (For a good recounting of the history, see Bolotovskii (2009).) If we look at Fig. 3.3 for the relevant geometry, we note that the angle, θ, between the line that denotes the flight path of the particle (which, in that figure, is the horizontal line pointing toward O_4) and the envelope of the emitted spherical waves is given by $\cos\theta = c/(v_{part}\, n)$. Because in physical situations $\cos\theta \leq 1$, it follows that for this geometry to hold up, the following condition must be met: $v_{part} > c/n (= c_{medium})$. In other words, the particle must be traveling faster than the speed of light *in that medium*. The waves emitted, which will be traveling at $c/n = c_{medium}$, will not be able to keep up with the

original particle, allowing the radiation left behind to combine coherently and be detected by ground-based instruments. (When the condition is not met, any emitted wavefronts will not be left behind in the wake of the propagating particle and will interfere with itself destructively, resulting in no observable radiation.)

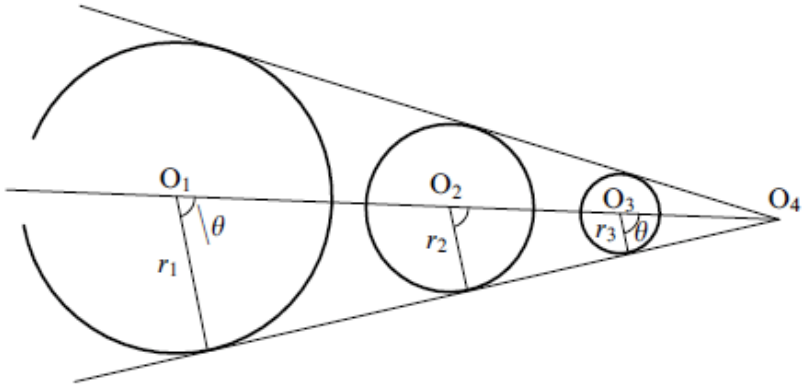

Figure 3.3: Cartoon of the geometry of Cherenkov radiation. From from Bolotovskii (2009).

In general, the emitted spectrum of Cherenkov radiation follows a $1/\lambda^2$ distribution. However, as we saw in Fig. 3.1, radiation with energies greater than UV will be absorbed by the atmosphere, thus resulting in a cut-off in the observable Cherenkov radiation. Additionally, we must remember that the index of refraction of the Earth's atmosphere is wavelength dependent - for example, the shorter the wavelength, the faster its speed, and thus the smaller its index of refraction. For wavelengths corresponding to radiation energies of X-ray or higher, the index of refraction is small enough that a particle cannot meet the condition for Cherenkov radiation - hence we see an additional factor contributing to a sharp cut-off in the Cherenkov spectrum at high energies. See Fig. 3.4 for the total Cherenkov spectrum.

Specifically, we see that the observable radiation will peak in the blue region of the optical range.

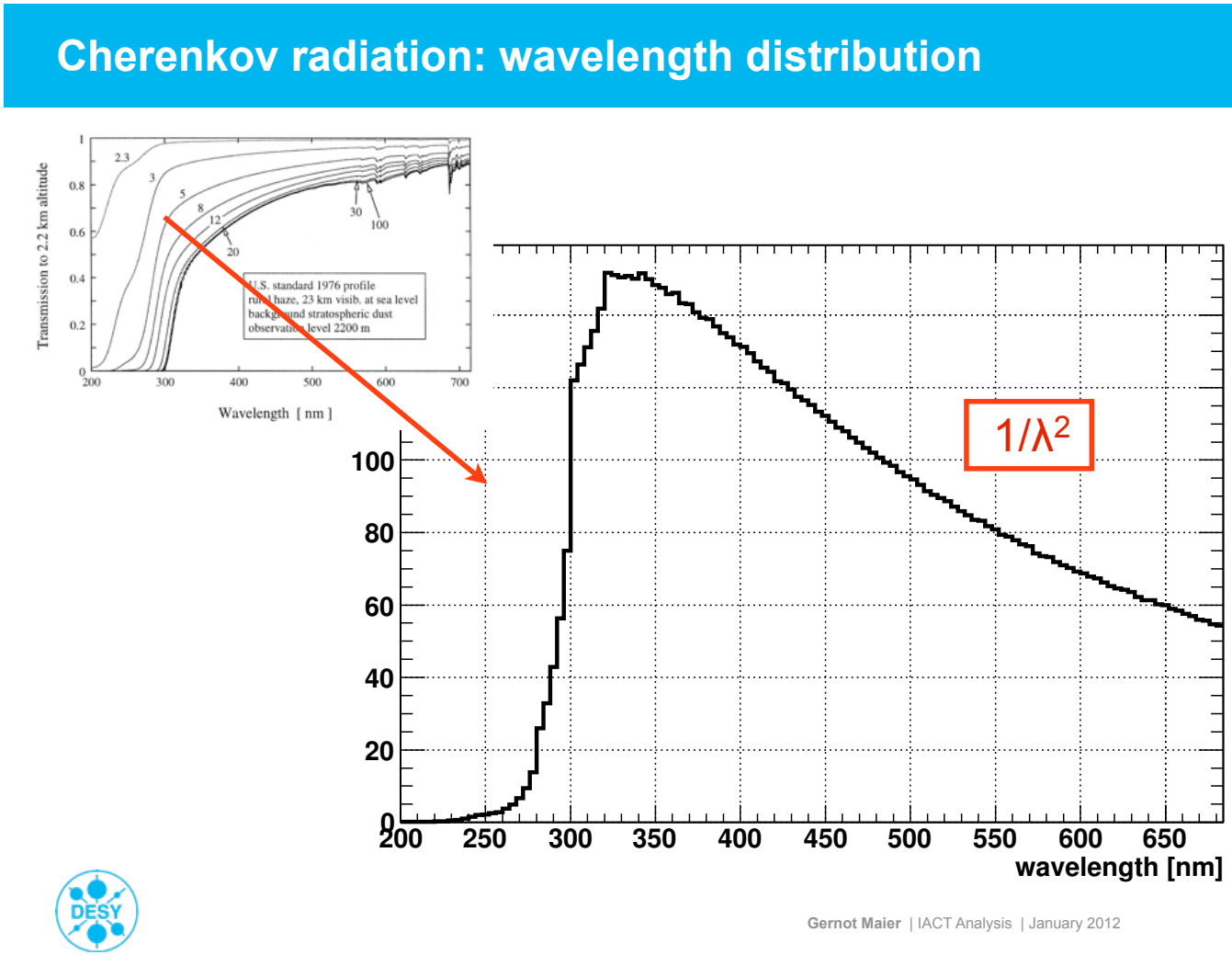

Figure 3.4: Large graph: The detected Cherenkov radiation spectrum resulting from a particle traveling through the Earth's atmosphere. Inset graph: Atmospheric absorption based on wavelength. Plot courtesy of Gernot Maier from an internal VERITAS presentation.

During the development of the electromagnetic showers, many of the electron-positron pairs produced by high-energy gamma rays will have more than enough energy to produce Cherenkov radiation. Of course, the absolute minimum energy an incident photon can have in order to pair produce is $2M_e c^2$. However, in order to observe the radiation by-products from a shower, the incident photon must have a large enough energy to pair produce electrons and positrons that, in turn, have enough energy to emit Cherenkov radiation. If we consider that the critical energy for air is 83 MeV (Longair (1992), pg. 208), the incident photon will have to have an absolutely minimum energy on the order of 10^2 or 10^3 MeV to build up a large enough shower for ground-based instruments to detect. Shower maximum will occur roughly 10 to 12 km or so above sea level. (For more information, please refer to Longair (1992)).

Because the main by-products (electrons and positrons) of showers initiated by ≤ 100 GeV photons die out quite rapidly after shower maximum, only Cherenkov radiation arrives at ground level. (Note that for photons with energy $\gtrsim 1$ TeV, the tail of the resulting electromagnetic shower can actually be detected by ground-based detectors. This method of detecting gamma-ray events has been used by other experiments - for example, the Milagro experiment (Atkins et al. (2003)). Although it is a very powerful technique, it must take into account intrinsic fluctuations in the electromagnetic shower development, which can result in relatively poor angular and energy resolution.) The opening angle of the radiation cone will be on the order of 1 deg, which, from a height of about 8 to 10 km, illuminates the ground with a pool of Cherenkov light with a radius of around 125 m. The shower lasts for roughly 10^{-4} seconds, but the resulting Cherenkov radiation travels almost as fast as the particles within the electromagnetic shower, meaning that the detectable light and the electromagnetic shower keep pace with each other within $\sim$2 ns. This short time window means that ground-based detectors can use very fast electronics, which in turn helps to cut down on unwanted background noise (see Völk and Bernlöhr (2009) for more details).

3.2 VERITAS

VERITAS, short for **V**ery **E**nergetic **R**adiation **I**maging **T**elescope **A**rray **S**ystem, is an array of 4 Imaging Atmospheric Cherenkov Telescopes (IACTs) that is designed to use Cherenkov radiation from air showers to detect very high-energy gamma rays, and to use the Earth's atmosphere as a fully active calorimeter. The array is located at the base of Mount Hopkins in Green Valley, Arizona, and the telescope design is based on the Whipple Observatory, an IACT that pioneered the field of ground-based gamma-ray astronomy and is located on a ridge 2.5 km above sea level on the same Mount Hopkins. VERITAS is sensitive to the 100 GeV to 50 TeV photon energy range. For its 4 telescope configuration, please refer to Fig. 3.5. Note that T1 was moved to its present location as part of an upgrade effort over the summer of 2009. Prior to the move, a source at 1% of the Crab Nebula flux could be detected in 47 hours of observations; after the move, that time decreased to under 30 hours (Ong et al. (2009)).

Basic Specs

The four identical telescopes are based on the Davies-Cotton design, with mirror reflectors spanning 12 m in diameter, and a camera located in the focal plane of the telescope, also 12 from the center of the mirrors. (See Fig. 3.6 for two views of a telescope.)

The camera (see Fig. 3.7 for a close-up) consists of 499 photomultiplier tubes (PMTs) with 0.15° spacing between each one; all together each telescope has a 3.5° field of view. Each PMT signal is read out by a 500 MSPS FADC (megasample-per-second flash analog to digital converter) (Buckley (1999)). For more information about VERITAS specs, please refer to Holder et al. (2008) and Ong et al. (2009). Because the array observes the radiation from air showers initiated within the Earth's atmosphere, it has an especially large collection area of about 10^5 m^2 (Krawczynski et al. (2006)).

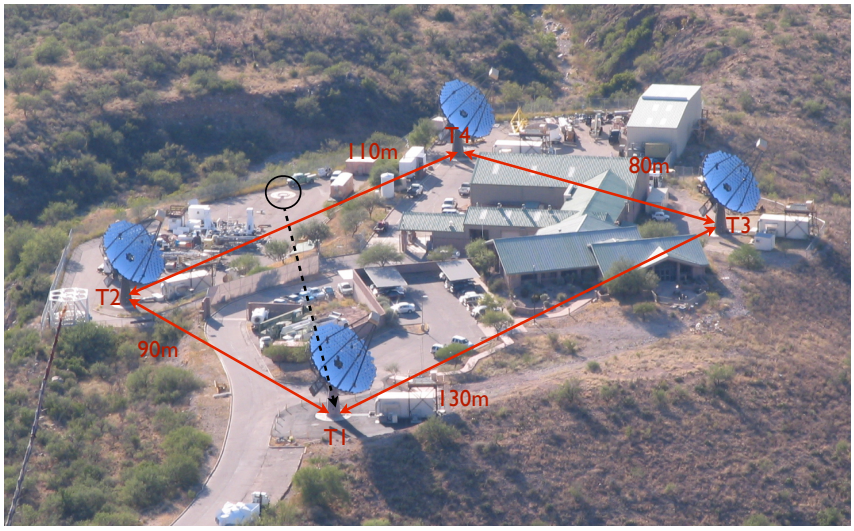

Figure 3.5: The configuration of the four IACTs of VERITAS. The black circle shows the original location of T1 and the dotted line shows its move to its present location over the summer of 2009. Photo credit: Steve Criswell; graphics added by Sarah Thibadeau.

Figure 3.6: Two views of the telescopes. Left image photo credit: Sarah Thibadeau. Right image (which contains Sarah Thibadeau for scale) photo credit: Brett McArthur

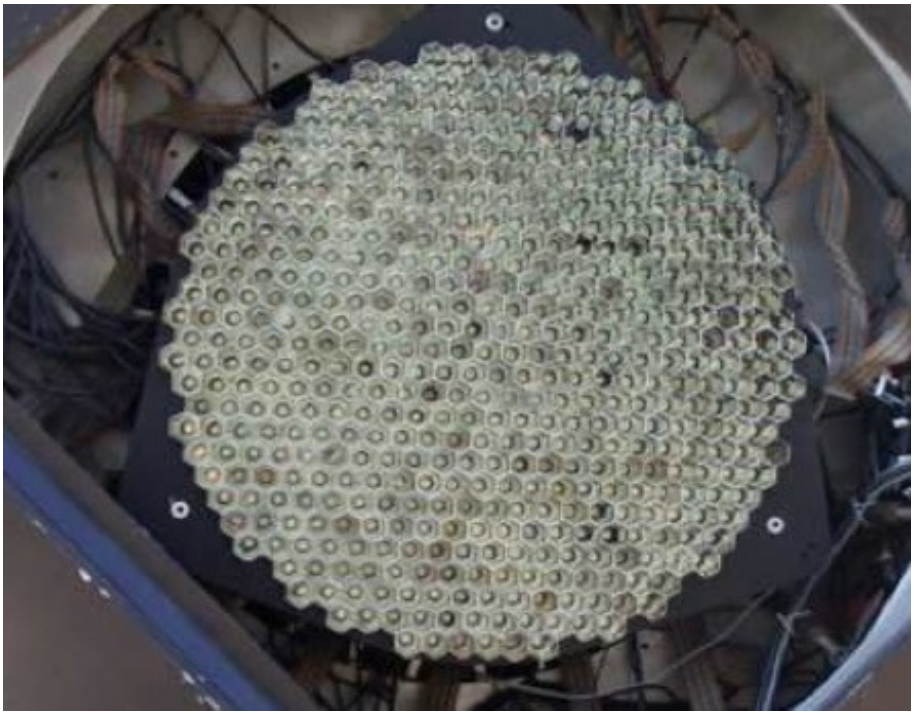

Figure 3.7: A close up of an IACT camera. From VERITAS Collaboration: T. Nagai et al. (2007).

3.2.1 Signal vs. Background

VERITAS' cameras are designed to be sensitive enough to detect the faint blue flashes of Cherenkov radiation that ultimately result from each high-energy photon hitting the atmosphere. However, a vast majority of the Cherenkov events that VERITAS records are in fact not from photon-initiated electromagnetic showers but from cosmic-ray initiated showers. For perspective, the array trigger rate (which both photon- and hadronic-initiated showers contribute to) is generally about 150 Hz; the rate of gamma rays from the Crab Nebula, which is a strong gamma-ray source generally used as the standard candle in high-energy astrophysics, is about 10 per minute for VERITAS.

Hadronic Showers

High-energy cosmic rays (about 75% of which are protons and most of the remaining 25% are helium nuclei) hit the atmosphere with a flux per solid angle that is $\geq 10^3$ greater than that

of gamma rays from the strongest gamma-ray sources (Völk and Bernlöhr (2009)). These events initiate a shower, called a hadronic shower, that has properties that closely mimic that of an electromagnetic shower. When a cosmic ray hits the atmosphere, the resulting interaction with the electric field of the atmospheric nuclei produces nuclear fragments and a number of positively and negatively charged pions, as well as neutral pions. The neutral pion quickly decays into two gamma rays, which in turn produce an electromagnetic shower of the kind already discussed. The positively and negatively charged pions will also eventually decay into positrons and electrons respectively, with additional by-products of neutrinos and muons. Of course, these positrons and electrons initiate their own electromagnetic showers. (See Fig. 3.8)

Because of the large transverse momenta of the pions, and thus the large angular spread in the resulting sub-showers, the overall hadronic shower will, in general, be much broader than an electromagnetic shower. (For a comparison, see Fig. 3.9). As will be discussed later, parameters can be established that allow an observer to differentiate from a cosmic ray induced shower and a gamma ray induced shower. Of additional help is the presence of the muons in a hadronic shower; these have a life time on the order of a microsecond. However, because of the effect of time dilation, to the ground-based observer their lifetime is actually $\sim 10^{-6}\gamma$, where here γ is their Lorentz factor. Those with a $\gamma \geq 20$ will live long enough to make it to the ground (note that this Lorentz factor corresponds to a speed roughly 0.9987 times the speed of light in a vacuum!). These muons that make it to the ground are then readily rejected by ground-based detectors like VERITAS. Furthermore, the single cone of Cherenkov light emitted from each individual muon can be detected as a "muon ring" or arc by ground-based detectors. (See Longair (1992), pg. 148 for more details.) The muon ring or arc adds to the more irregular shape of the Cherenkov images that result from hadronic showers, which improves the detector's ability to discern between gamma-ray images and the hadronic images that contribute to the background signal.

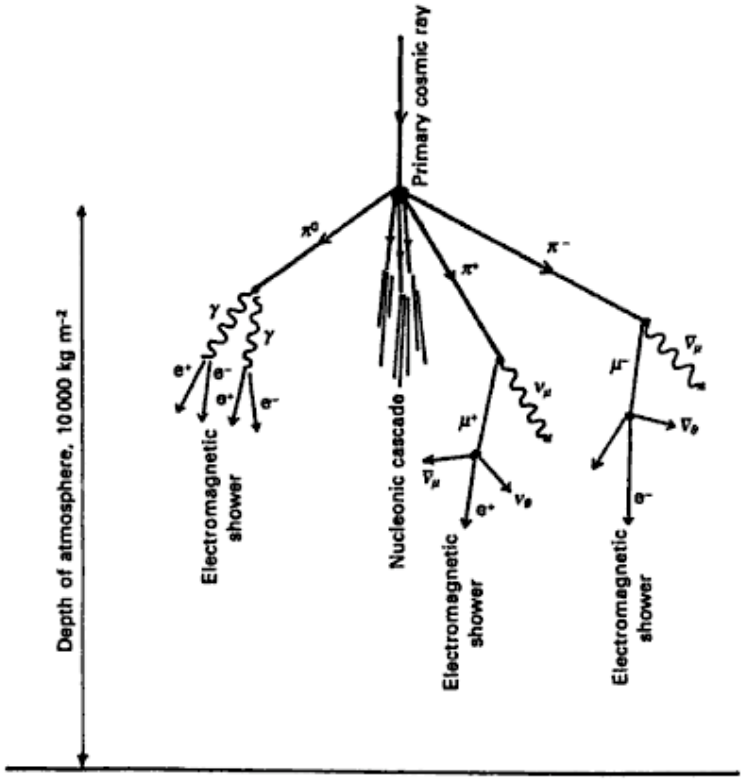

Figure 3.8: An example of a cosmic ray induced shower. From Longair (1992), pg. 149.

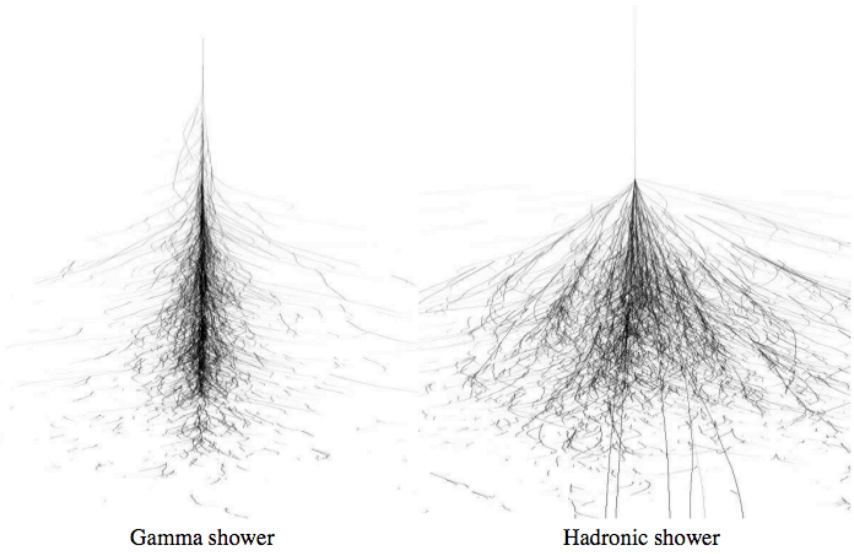

Figure 3.9: A comparison of a gamma-ray shower and a hadronic shower. Note that the gamma-ray shower is narrower than the hadronic one. From Völk and Bernlöhr (2009).

Hillas Parameters

When a telescope camera records an image of a shower, the next step is to characterize that image using standard parameters. Doing so not only helps to determine if a shower was gamma-ray or cosmic-ray initiated, but it also will help in the reconstruction of several other important features discussed below, such as shower direction and original energy. Fig 3.10 gives a visualization of how the geometry of a shower maps to the geometry of the resulting image in the telescope camera. We can see that the characteristic image in the camera is an ellipse.

There was a key paper published in 1985 that established the framework for the parameters that are now considered standard for image analysis (Hillas (1985)). These parameters are called the Hillas parameters. See Fig 3.11 for several of these parameters. The ones that are especially important are *length*, *width*, and *image axis*. For example, the length and width pa-

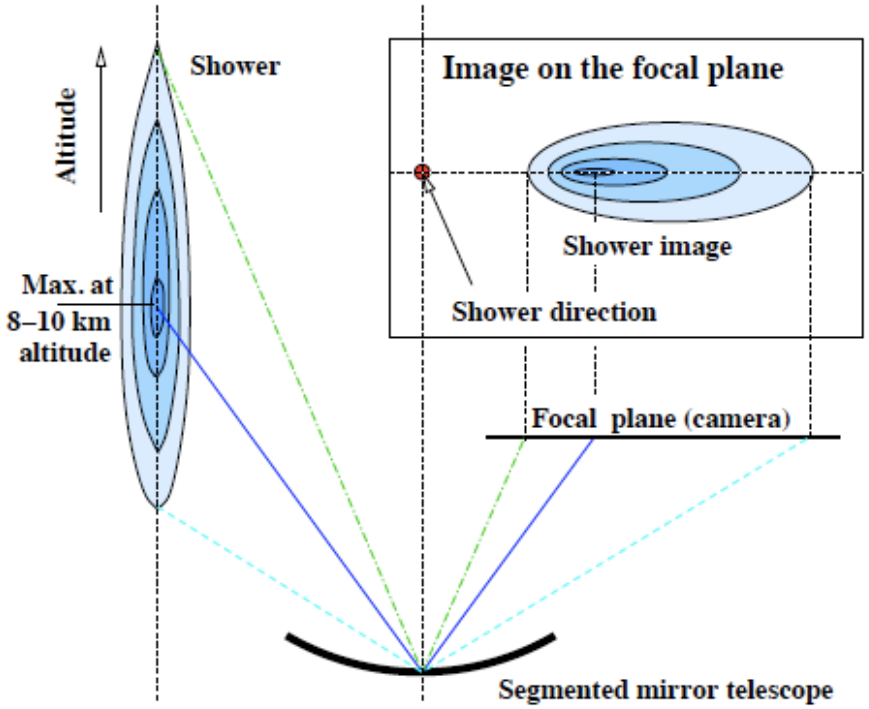

Figure 3.10: A diagram of how the shower geometry translates to an image in an IACT camera. From Völk and Bernlöhr (2009).

rameters are useful when differentiating between gamma-ray showers and hadronic showers, as hadronic shower parameters are typically larger than gamma-ray shower parameters. Additionally, cosmic ray initiated showers have a larger width due to the transverse momentum in the hadronic interactions; the length is different due to differences in the cross-section and the longitudinal shower development. For a sense of how these parameters, particularly width and length, can be used as a tool to differentiate between gamma-ray events and cosmic-ray events, a good example would be the seminal 1989 discovery of TeV photons from the Crab Nebula using the Whipple observatory (i.e., using one IACT) - Weekes et al. (1989). In that paper, they discuss Monte Carlo simulations they executed by tracking the air shower development and telescope response to cosmic rays and gamma rays hitting the atmosphere. One of the important results from these simulations was a plot of the distribution of the width and length parameters, broken down according to cosmic rays and gamma rays. See Fig. 3.12. As can be seen, despite some overlap, there is a rough distinction between typical cosmic-ray parameter values and gamma-ray parameter values.

Analysis of Data from Stereoscopic Telescope Arrays

As has been alluded to, Whipple, which was built in 1968, was the first ground-based, high-energy gamma-ray observatory (see, eg, Fazio et al. (1968)), and was the first instrument to detect photons in the TeV range. It essentially helped lay the groundwork for the extremely powerful IACT technique used for detecting gamma rays, and its impact on the field of astrophysics cannot be understated. One of its main drawbacks, however, was its single telescope design, which restricted its sensitivity and energy threshold, among other things. A major step forward in ground-based gamma-ray astronomy was the implementation of the stereoscopic method, where multiple telescopes are used in tandem. Just as the Whipple group pioneered the imaging technique, another ground-based gamma-ray observatory, HEGRA (High-Energy Gamma-Ray Astronomy) pioneered and demonstrated the power of the stereoscopic measurements obtained with multiple telescopes (Aharonian (1993), Kohnle

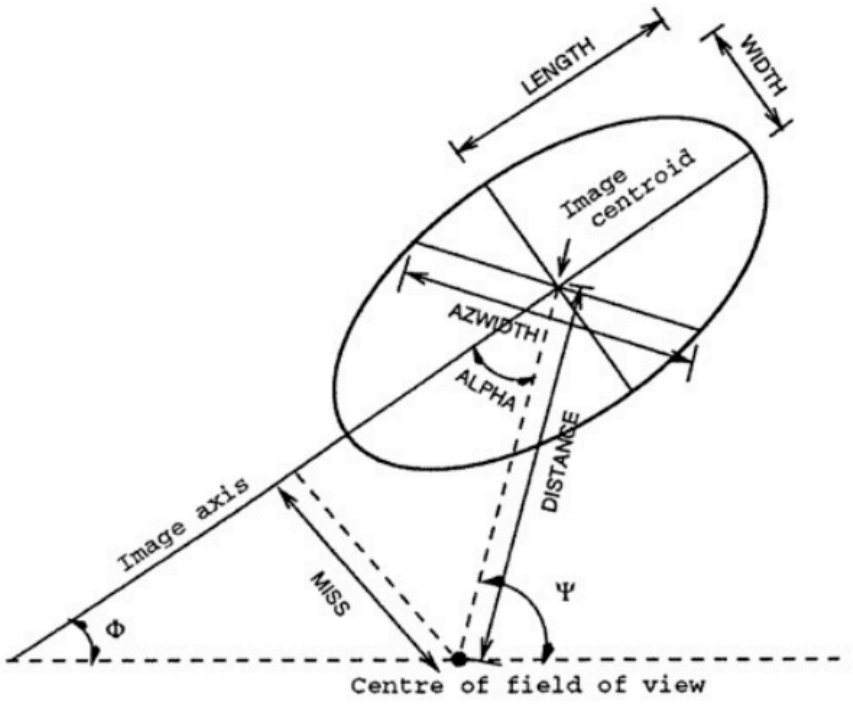

Figure 3.11: Hillas parameters used for the ellipse that constitutes a standard shower image in an IACT camera. Plot courtesy of Gernot Maier from an internal VERITAS presentation.

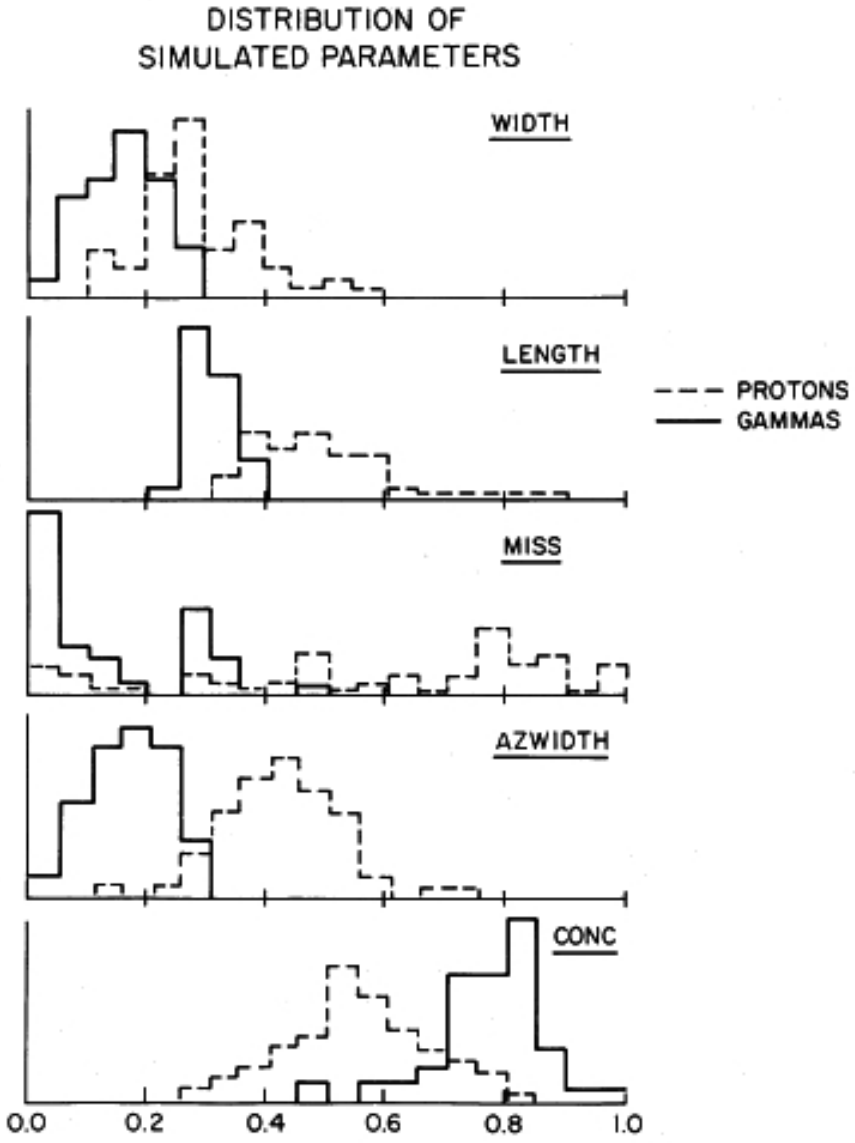

FIG. 4.—Image parameter distribution predicted by simulations for an on-axis gamma-ray source at the zenith and an isotropic background of cosmic rays. In all but *Conc* the scale is in degrees.

Figure 3.12: Distribution of Hillas parameters from Monte Carlo simulations. For the purposes of this discussion, the two important ones can be seen in the top two panels - width and length. From Weekes et al. (1989).

et al. (1996)). Having multiple telescopes view the same event from different angles provides a wealth of additional, 3-dimensional information that, for example, enables a precise determination of shower direction and other parameters, as well the suppression of muon events. The latter is of special importance because muons constitute a significant fraction of the background events observed during telescope operation. With one telescope, unless that telescope fell within the center of the muon cone (in which case the telescope would see the whole distinctive muon ring shape), differentiating between a muon event and a gamma-ray event is extremely difficult. However, with multiple telescopes, the muon cone is generally small enough that only one telescope would record it, thereby failing to initiate the array trigger (see below). Cutting back on a significant amount of the background allows the telescope array to lower its energy threshold

As a further example of the enormous benefits of the stereoscopic method, it is worthwhile to take a moment to more carefully define how two of the more important image parameters - width and length - change with the use of multiple telescopes. These parameters are recast as *mean scaled width (MSW)* and *mean scaled length (MSL)* (Krawczynski et al. (2006)). For any given shower, they are defined as:

$$\text{MSW} = \frac{1}{N_{images}} \left[\sum_{i}^{N_{images}} \frac{width_i}{w_{MC}(R, S, \theta)} \right] \tag{3.1}$$

$$\text{MSL} = \frac{1}{N_{images}} \left[\sum_{i}^{N_{images}} \frac{length_i}{l_{MC}(R, S, \theta)} \right] \tag{3.2}$$

where N_{images} is the number of telescopes used (ie, the number of images possible for one event, meaning it is an integer number from 1 to 4), $width_i$ and $length_i$ are the measured width and length from each telescope's image, and $w_{MC}(R, S, \theta)$ and $l_{MC}(R, S, \theta)$ are the values for width and length derived from gamma-ray Monte Carlo simulations that are pertinent to this particular shower; they are functions of the image's position and orientation

in the camera, and the targeted source's position in the sky. When a camera image closely mirrors that of a simulated gamma-ray image, its measured width or length will be similar to the simulated value, thus resulting in a fraction close to 1; the values from all telescopes are then averaged. We expect that events that are gamma-ray like should have a MSW or MSL close to 1. Large deviations from 1 help to differentiate gamma-ray events from cosmic-ray events. (The amount of deviation is not fixed. Rather, analysts can choose the amount of deviation from 1 that they deem tolerable for their particular source. For example, 0.25 is a common deviation value.) By incorporating *weighted* information from all telescopes and from simulations, the stereoscopic method has produced a powerful method for more reliably selecting an actual gamma-ray signal out of the cosmic-ray background.

3.2.2 3-Level Trigger System

In order to weed out the random noise fluctuations that naturally occur during observations, VERITAS employs a 3-level trigger system that provides increasingly rigorous conditions that must be met in order for an event to be recorded. Level 1 - also called the L1 rate - requires each pixel surpass a set signal threshold. Once this threshold has been met, the L1 is triggered. The second trigger is the telescope, or L2, trigger, which requires that at least 3 adjacent pixels see an L1 trigger within 10 nanoseconds of each other. Each telescope has its own L2 rate that can be monitored during observations. Finally, there is the array trigger - ie, the L3 rate - that requires that at least 2 telescopes trigger within 50 nanoseconds of each other (see, for example, Krawczynski et al. (2006), which details the work that went into testing and simulating the gamma-hadron separation techniques that VERITAS eventually employed). The triggering of L3 communicates to the FADC to stop read-out. The region in the FADC memory that contains the signal of interest can then be found by offsetting the L3-stop time. This trigger system provides the first step of identifying true gamma-ray events, and enables more efficient real-time data storage.

3.2.3 Shower Direction Reconstruction

The stereoscopic method provides the ability to accurately reconstruct the direction of the shower, and thus the initial direction of the incident photon. The key to the method is the fact that "the major axes of the images are projections of the shower axis" (Krawczynski et al. (2006)). Thus, in principle, information from all 4 telescopes can be combined to find the original shower direction and location. See Fig. 3.13. There are several different ways one can combine the geometrical information to obtain shower direction, though all methods rely on the intersection of the shower axes in either angular space (for the reconstruction of the shower direction) or projected on the ground (for the reconstruction of the impact point). Typically, the methods involve some kind of weighting so as to preferentially use cameras with images that have more precisely-calculated shower parameters such as length and width of the ellipse.

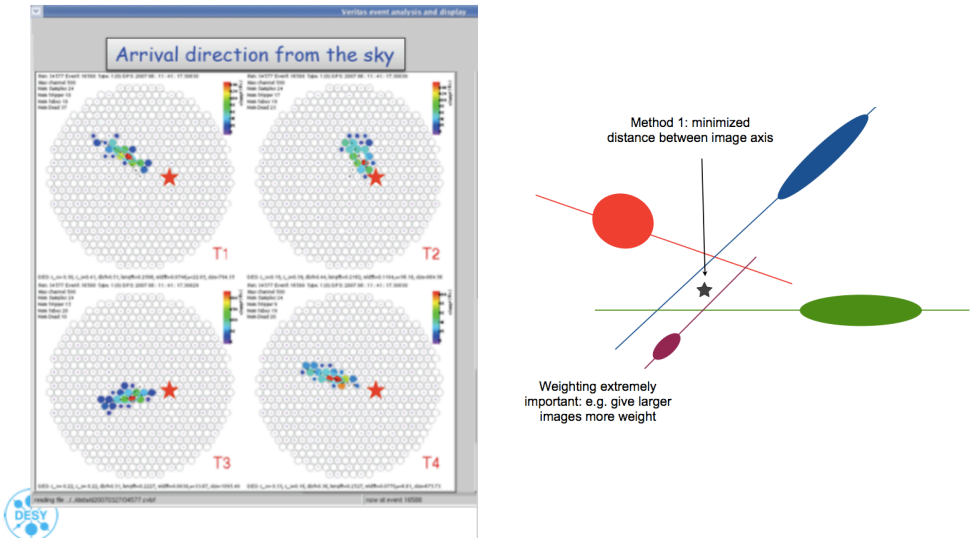

Figure 3.13: Left image: a typical image in all 4 IACT cameras. Right image: one possible way to use the information contained in the camera images to reconstruct the shower direction. Both images courtesy of Gernot Maier from an internal VERITAS presentation.

3.2.4 Energy Reconstruction

The ability to reconstruct the energy of the original incident photon based on the observed image parameters is extremely important, particularly to our analysis of Lorentz invariance violation, where we ultimately need event lists composed of individual event time and energy. This process of energy reconstruction is based on extensive simulations. The showers of and subsequent telescope response to incident photons with known energies and directions are simulated and look-up tables are generated that give image parameters as a function of initial energy. In practice, then, these look-up tables are "inverted" and are used to determine photon energy based on the values of image parameters derived from post-observation analysis (for more information, see Krawczynski et al. (2006)). One element that is important to note is the relationship between initial energy and shower parameters. As we saw from our discussion of electromagnetic showers previously, the number of particles present during shower maximum scales with the energy of the original photon. Thus, the greater the energy, the bigger the shower, and thus the shower parameters can be expected to scale appropriately.

An additional parameter important to accurate energy reconstruction is the *impact parameter*. This is the location at which the original photon would have reached ground level if its interactions with the atmosphere had not generated an electromagnetic shower. (This point is calculated through the reconstruction of the shower direction.) The further away this impact point is from the telescope array, the less Cherenkov light the array will observe from the shower, and thus the less intense the signal. By correcting for the impact point's location with respect to the telescope array, the energy of the original gamma ray can be more accurately reconstructed.

3.3 Instruments Used For DCF Analysis

For the discrete correlation function analysis, we chose to compare gamma-ray emission from the Fermi Gamma-Ray Space Telescope with X-ray emission from Swift. At this point it should be noted that one of the excellent features of the discrete correlation function is its ability to use data in any format, whether that data is composed of individual events or is binned, or whether there are large gaps in the data. Although using individual events is ideal - binning always tends to inject an additional element of complication into analysis - the realities of the data collection necessitated that we use data that had been binned in time. As we discuss each of these instruments below, the reasons for doing so will become clear.

3.3.1 Fermi Gamma-Ray Space Telescope

The Fermi Gamma-Ray Space Telescope was launched into orbit on June 11, 2008 and has since proved indispensable to the field of high-energy astrophysics. Aboard this telescope are two instruments - the Gamma-Ray Burst Monitor (GBM), which is designed to detect gamma-ray bursts and relay the sky coordinates to other observatories, including VERITAS, between seconds and minutes after the start of the event, and the Large Area Telescope (LAT). Much of the data used in the discrete correlation function analysis presented in this thesis came from the Fermi-LAT; thus it is this instrument that we will focus on primarily. For a more detailed discussion than the one presented here, please refer to Atwood et al. (2009).

The Fermi-LAT is a large field of view (FoV) gamma-ray telescope sensitive to a range of below 20 MeV to more than 300 GeV (Atwood et al. (2009)). (Note that because of this, the Fermi-LAT serves as an excellent complement to VERITAS, as it fills in the energy region just below VERITAS' range of sensitivity.) The instrument works by providing high-Z mate-

rial that facilitates the $e^- - e^+$ pair production from a gamma-ray incident on the instrument. Specifically, the instrument consists of a precision converter-tracker and a calorimeter designed to detect and analyze the paths of the particles created in the initial pair-production. The converter-tracker contains layers of tungsten that serve to convert the gamma ray into an $e^- - e^+$ pair; while most of the pair production occurs in the first layer, higher energy gamma rays may pass through that layer and pair produce in subsequent layers. Each layer of tungsten is closely followed by two thin sheets of silicon strips that track the trajectory of the resulting particles and thus help to reconstruct the direction of the incident gamma ray. After these elements, a calorimeter is in place that tracks the development of the resulting shower, and provides, among other things, the information necessary to reconstruct the energy of the initial gamma ray. The design is implemented such that most of the gamma rays that pair produce in the converter-tracker will make it to the calorimeter. The calorimeter has a total vertical depth of 8.6 radiation lengths and the whole instrument has a vertical depth of 10.1 radiation lengths (Atwood et al. (2009)).

One of the main benefits of FermiLAT is its large FoV and its ability to observe the entire sky in a relatively short amount of time. The height/width ratio of its converter-tracker is 0.4, resulting in a FoV of about 2.4 steradians at 1 GeV. The Fermi-LAT generally operates in "scanning" mode, which allows for an almost uniform exposure of the entire sky after 2 complete orbits - ie, 3 hours of elapsed time (Atwood et al. (2009)).

Using Fermi Data

Fermi-LAT monitors several sources that are deemed important; generally, they are those that have exhibited interesting, flaring behavior in recent history. The information is publicly available through their website (`http://fermi.gsfc.nasa.gov/ssc/data/access/lat/msl_lc/`) in the form of Fits data files. These Fits data files contain flux values in photons/sec/cm^2, the error on those flux values, also in photons/sec/cm^2, as well as the

start and end times for that particular point, in Mission Elapsed Time (which will be discussed below). We took the time value for each point to be the half way point between the start and end times.

The data points are presented in either daily or weekly installments. Although for this study daily light curves would have been preferable in order to enable us to get as finely sampled data as possible, we ultimately chose to use the weekly light curves. The main problem with the daily variety was that a significant number of the data (ie, usually larger than 20%) were upper limits rather than detected data points. Because using a large number of upper limits may lead us to overestimate the flux values of the light curve, we wished to err on the side of caution and use the more reliable data.

There were still usually a handful of upper limits in the weekly light curves, as well as occasional one to two week data gaps. As can be readily seen by inspection of the expression used to calculate the DCF (see Eqn. 2.7 and Eqn. 2.9), the fact that "missing" data exists is itself not a problem - the equation is designed to deal with the realities of astronomical data. However, the simulations portion of the analysis requires the discrete Fourier transform of one of the data sets, which itself requires an evenly sampled data set. Because the Fermi data is far more evenly sampled to start with than the Swift data we also use, it made more sense to come up with a way to generate an even sample out of this data. To do so, we simply either replaced the upper limits or filled in the data gaps using linear interpolation.

One final note: the Fermi Fits files allow the user the option of choosing to look at data within different energy bands. We chose to use the all-inclusive, 100 - 300,000 MeV energy band.

3.3.2 Swift Gamma-Ray Explorer

The Swift Gamma-Ray Explorer (Gehrels et al. (2004)) is a satellite dedicated largely to the study of gamma-ray bursts (GRBs) and their afterglows. It was launched on November 20, 2004 and contains three instruments - the Burst Alert Telescope (BAT), which primarily serves to detect GRBs and isolate their coordinates, the Ultraviolet/Optical Telescope (UVOT), and the X-Ray Telescope (XRT). For the purpose of the DCF analysis, we are mainly concerned with X-ray data, and thus will confine our discussion to Swift-XRT only. Please refer to Burrows et al. (2005) for more detailed, technical information about this particular instrument.

Although most of Swift's main mission objectives revolve around the study of GRBs - for which having UV, optical, and X-ray instruments on board allows for comprehensive multiwavelength study of GRB afterglows - the Swift-XRT instrument also conducts its own monitoring of sources, thus providing an excellent window into the X-ray regime of many important astrophysical objects. The XRT employs a grazing incidence Wolter 1 telescope and a CCD camera to obtain X-ray images (Gehrels et al. (2004)). It has an effective area of 110 cm^2, and is sensitive to X-rays in the 0.2 to 10 keV energy range.

In order to be able to continuously observe the afterglows of GRBs, whose fluxes can decrease significantly over their lifetime, Swift-XRT must be able to respond rapidly, and autonomously, to quickly changing flux conditions (Burrows et al. (2005)). Thus, built into its design are several different observing modes, each of which is designed to accommodate a different range of flux magnitude and which can be called upon quickly depending on the flux count rate. The two modes of primary importance to the construction of light curves are the windowed timing mode, which uses high temporal resolution (about 1 microsecond) at the expense of position information and is best for fluxes below 5 Crab, and the photon-counting mode, which has a slower time resolution (about 2.5 seconds) but is very useful for

faint signals (ie, fluxes below 1 mCrab) (Burrows et al. (2005)).

Using Swift Data

As stated, Swift-XRT conducts its own monitoring of sources, typically ones that the Fermi-LAT has chosen to monitor. This data is also publicly available through their website (`http://www.swift.psu.edu/monitoring/`) in the form of ASCII text files, which contain flux values in units of counts/sec, errors on the flux, also in units of counts/sec, and the time of the data point, in Modified Julian Date (MJD). Unlike the Fermi data, Swift data tend to be far more unevenly sampled.

3.3.3 A Note On Time Conventions

The actual time units of the data sets have no importance to the DCF analysis; what is important is the *relative* time between the two data sets under investigation. Because of this, the same time-counting system should be used; for simplicity, the best option is to just ensure that both data sets use the same time convention. As already noted, Fermi data is presented in Mission Elapsed Time (MET) while the Swift time is in the Modified Julian Date (MJD) time system. MET is a time counting system that picks an arbitrary starting point as "0" and counts continuously from there in seconds; it has the advantage of not having to accommodate leap seconds or other adjustments to everyday time keeping. MJD, on the other hand, is a common astronomical time keeping system comprised of an integer component and a decimal component. The integer component denotes the day while the decimal component represents the time of day as a fraction of that day.

Fermi's MET starts at an MJD of 51910 (which corresponds to midnight on January 1, 2001). The formula, then, to convert between the Fermi MET to MJD is:

$$MJD = \frac{MET}{86400} + 51910 + 7.4287037 \times 10^{-4} \tag{3.3}$$

where dividing MET by 86400 (ie, the number of seconds in one day) gives the number of days that have elapsed since the start of MET, and 7.4287037×10^{-4} is the conversion factor between the two time keeping systems that accounts for leap seconds. We applied this formula to the Fermi times in order to have the same time convention for each data set.

Chapter 4

Analysis Results

4.1 Lorentz Invariance Violation

We conducted the LIV analysis with both a linear model and a quadratic model using flare data from the blazar Mrk 421, to be discussed presently. In each model, once the θ's that minimized entropy was found - which we are calling θ_{min} - we interpreted those results in the framework of quantum gravity by calculating the constraints on ξ and E_{QG}. What follows is a brief discussion of the history and characteristics of Mrk 421; we then report on the results from the linear model analysis and the quadratic model analysis.

4.1.1 Mrk 421

Mrk 421 is one of the more famous and well-studied of the known extragalactic blazars. It holds the distinction of being the first extragalactic object to be detected in the TeV regime (Punch et al. (1992)), a feat that was accomplished at the Whipple observatory (which, as already discussed, was a pioneer of ground-based gamma-ray astronomy, and was the precursor to VERITAS). It is a relatively close (z=0.031) BL Lac object (see Ulrich et al. (1975), Maza et al. (1978)) that has been known to exhibit extremely violent, fast flares, with sub-hour flux variability having been seen during these flaring episodes (for the first of such reports, see Gaidos et al. (1996)), thus making it one of the most quickly varying

gamma-ray sources (Abdo et al. (2011b). In addition to this behavior, it has also exhibited spectral variations during flaring episodes, with a fairly well-established correlation between flux and spectral index (Krennrich et al. (2002), Aharonian et al. (2002)).

Mrk 421 has been a prime candidate for use in many different types of studies. All of the ground-based gamma-ray telescopes have observed and analyzed it (for a very limited selection of the vast amount of papers available, refer to Aharonian et al. (2003), Aharonian et al. (2005), and Albert et al. (2007)). It is also often the subject of extensive multi-wavelength campaigns. For an example of one led by VERITAS, see Acciari et al. (2009b). For other examples, see Buckley et al. (1996), in addition to Fossati et al. (2008b) and Rebillot et al. (2006a). The studies have all produced a wealth of probing analysis into features including flux variability, spectral variability, SED modeling, and emission mechanisms and regions.

Because of its well-documented, sub-hour flaring episodes, Mrk 421 is an excellent candidate for LIV studies. It fits the criteria of properties required from a source candidate (see, for example, Amelino-Camelia et al. (1998) - though this paper proposes the use of gamma-ray bursts, it does establish a framework for experimental tests; additionally, refer to Biller et al. (1999), which provided the first published limit on the quantum gravity energy scale, and did so using Mrk 421 flare data from the Whipple observatory): it is extragalactic, thus ensuring that emitted photons traverse enough distance before reaching Earth to allow the dispersion effect to accumulate, and it emits highly energetic photons in large, very rapid bursts. In particular, the data from a major flare on February 17, 2010 provides us with an excellent opportunity for a rigorous test.

4.1.2 Mrk 421 Flare

On February 17, 2010 UTC, Mrk 421 exhibited a spectacular flare; the flare was so large that Mrk 421 was "detected at $> 10\ \sigma$ statistical significance in any 2 minute bin" (Galante

(2011)). See Fig. 4.1.

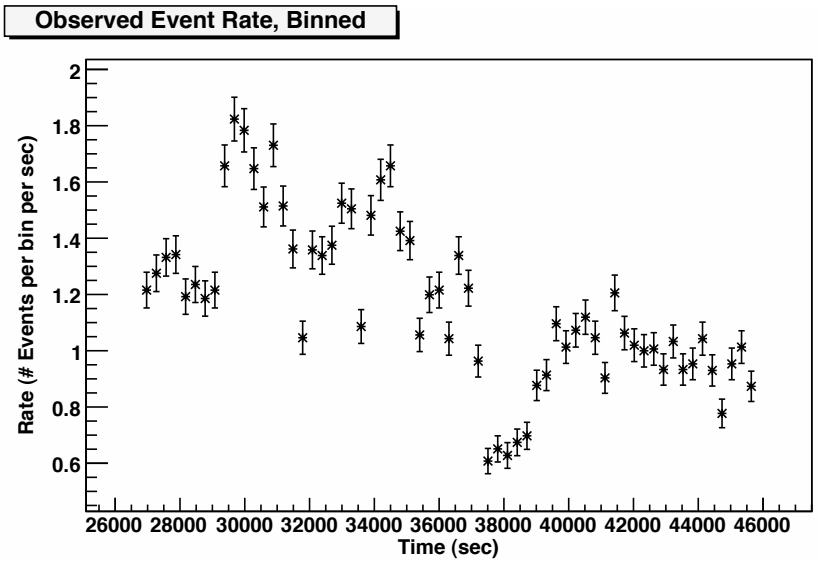

Figure 4.1: The observed' Mrk 421 event rate. We have collected the data into roughly 5 minute bins, and plotted the event rate per bin (i.e., the number of counts per bin divided by 300 seconds) versus the time that falls in the center of each bin. Note that the time is the UTC time of day in seconds on February 17, 2010.

Given the contemporaneous burst of a large amount of high-energy photons, and the great distance those photons traveled, the episode presented itself as an excellent opportunity for an experimental investigation into LIV phenomena. The flare's event list (which is composed of the reconstructed energy, in GeV, for each event, as well as the UTC time of day in seconds associated with each event), encompasses 22,248 individual events spread over about 5.27 hours in the course of one night. Due to technical issues, Telescope # 1 was offline, resulting in data being taken with a 3 telescope array only. For more information about this flare and the data collection, please refer to Galante (2011).

Observations of the flare began at roughly 7:30 on February 17, 2010 UTC, and ended at roughly 12:50, at the end of the night in Tucson, AZ. Over the course of the observations, Mrk 421 continued to rise, reached its culmination, then began to set. Please refer to Fig.

4.2 for its elevation plot as a function of UTC time for that night, taken from Wakely and Horan (2012).

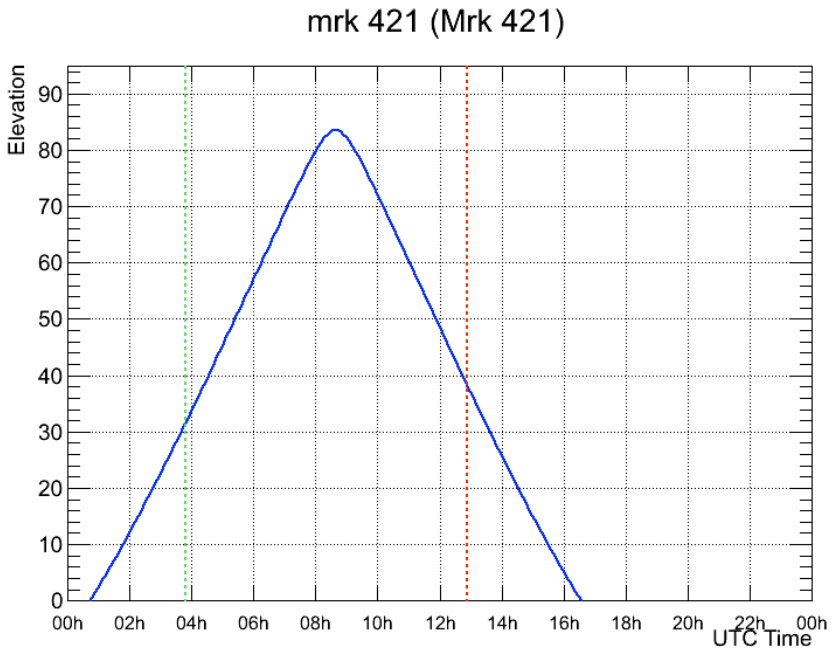

Figure 4.2: Mrk 421's elevation plot over the course of the night of February 17, 2010 UTC. The green dotted vertical line refers to moonset at the VERITAS site, and the red dotted vertical line refers to sunrise at the VERITAS site. Plot from Wakely and Horan (2012)

VERITAS' energy threshold is zenith angle dependent, particularly at larger zenith angles. There are two systematics that lead to this - not only is there larger atmospheric absorption of lower energy gamma rays the more obliquely they enter the atmosphere (since the photons must travel through more atmosphere), but the resulting cone of Cherenkov light is much broader, which means there is a lower density of light, which in turn makes it more difficult for the VERITAS PMT trigger conditions to be met. This zenith angle-dependent energy threshold is of particular importance to the LIV study; because this study seeks to analyze the arrival times of individual photons given their reconstructed energy, we require as unbiased a view of energy as a function of time as possible in our event lists.

For illustrative purposes, we plotted the Mrk 421 energy versus time in roughly 5 min bins in two energy bands - all those events that have an energy larger than the median energy observed - calculated to be 563.757 GeV - and all those events that have an energy less than the median energy observed. In this plot (please refer to Fig. 4.3) a rise in average energy over the course of the night is clearly visible, particularly in the lower energy band.

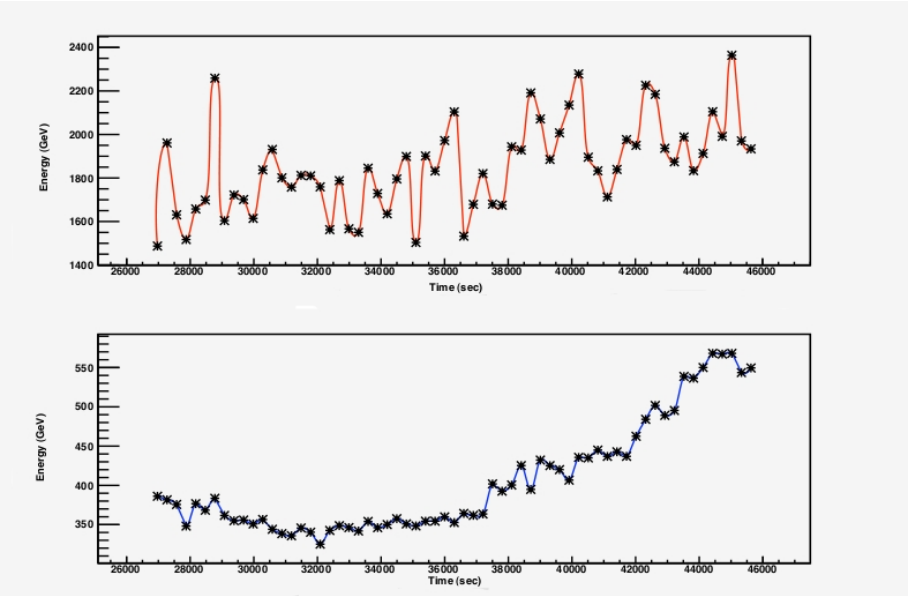

Figure 4.3: Mrk 421's average energy over the course of the night. The upper panel contains events whose energy is greater than the median energy of 563.757 GeV; the lower panel contains events whose energy is less than the median energy. Note that energy is in GeV and, as usual, time is UTC time of day in seconds on February 17, 2010.

Because this rise in energy could lead to the appearance of an artificial dispersive effect, the simplest solution was to (1) cut away the sections of the night that see the largest rise in energy, and (2) cut away the lowest energies, since these are seen systematically less over the course of the whole night and we wanted each energy band to be detected equally. To determine where to make these cuts, we plotted, in twenty minute slices, a histogram of all the events with energy less than the median energy (ie, those in the lower panel in Fig. 4.3). Please refer to Fig. 4.4.

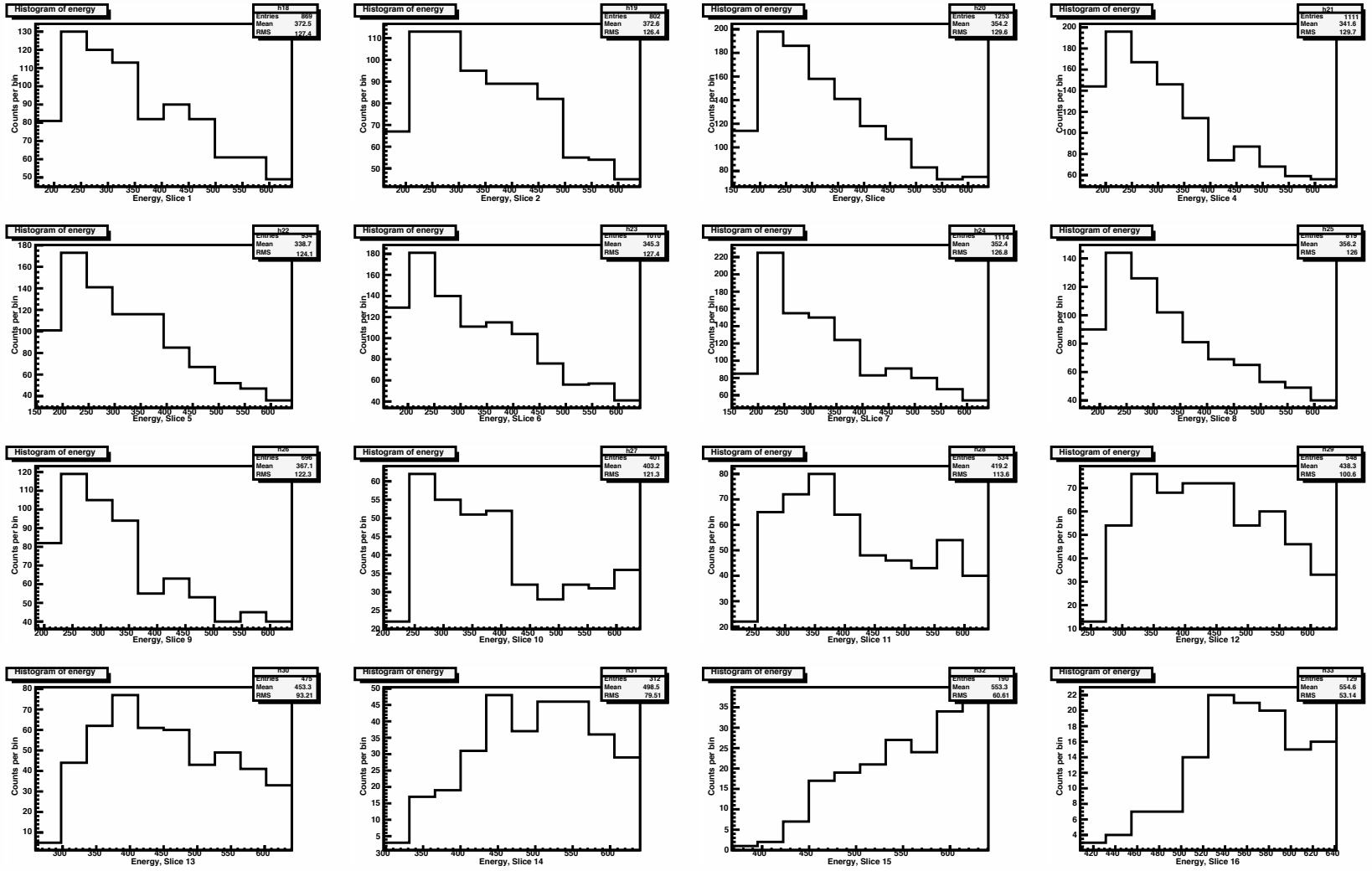

Figure 4.4: Histograms of all the events from Mrk 421 flare with energy less than the median energy of 563.757 GeV in consecutive 20 minute time slices. Note that energy is in GeV.

Starting with the top left histogram and counting horizontally, we can easily see that between slices 9 and 10 there is a drastic decrease in the number of events that correspond to the lowest energies. Thus, we cut everything after time slice 9 - ie, we cut all events with a time larger than 37,650 sec. Additionally, we cut all events that corresponded to the lowest energy bin - ie, we cut all events with an energy less than 215 GeV. Once we did this, we were left with 12,874 events that formed a much flatter distribution of average energy versus time. Fig. 4.5 shows the energy distribution post-cuts.

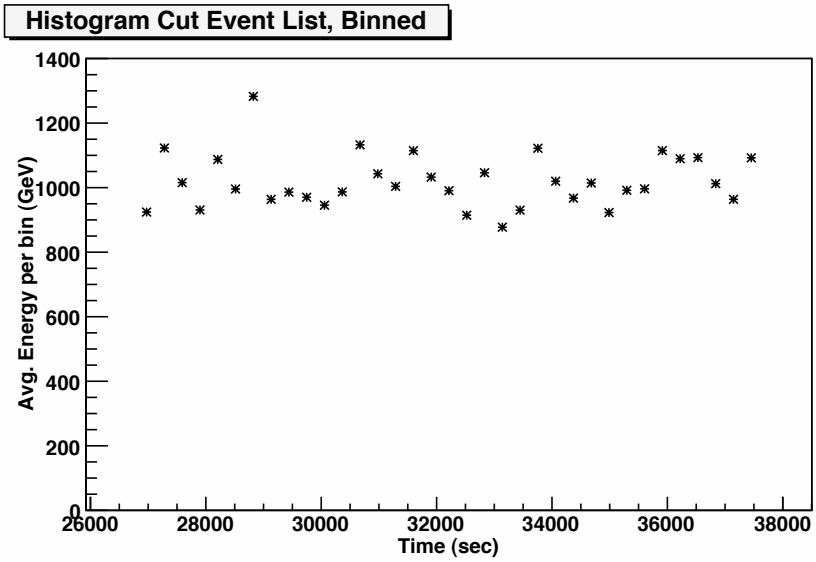

Figure 4.5: Mrk421's average energy versus time in 5 minute bins, post-cuts. As usual, the time is UTC time of day in seconds on February 17, 2010.

4.1.3 Linear Model Results

Using this Mrk 421 flare data and using the linear time delay expression $t_i' = t_i^{obs} - \theta(E_i^{obs} - E_{avg})$, we found the experimental (i.e., observed) θ_{min}, which we are calling θ_{min}^{obs}, to be $\theta_{min}^{obs} = -6.58 \times 10^{-3}$ sec/GeV, which corresponds to a minimized entropy of $S_{min} = 5.12$. See Fig.4.6 for the distribution of entropy versus test θ's.

To test statistical significance, we conducted a Monte Carlo simulation of $1,000$ random event

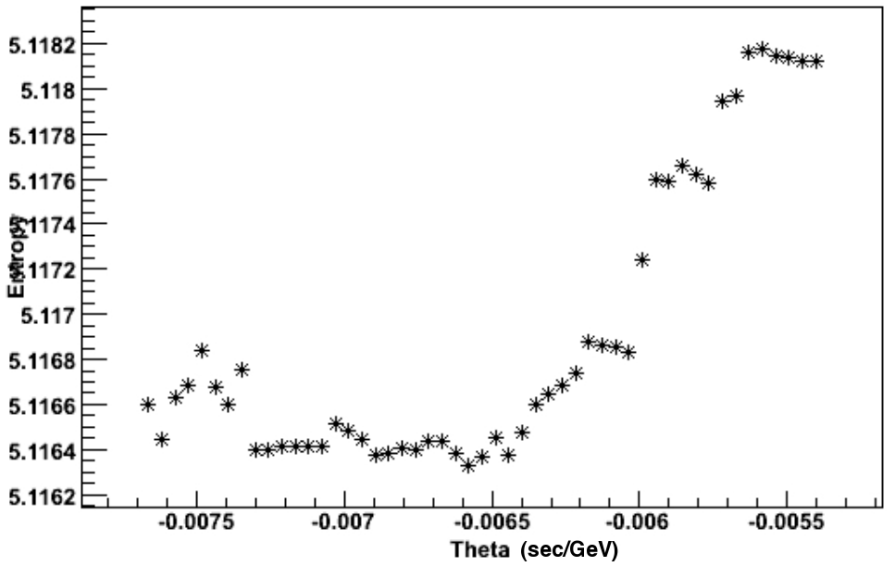

Figure 4.6: The experimental entropy versus θ distribution for the Mrk 421 data set using the linear model.

lists, each created by scrambling the energy of the experimental event list (as mentioned in Chapter 2). For each random event list, we used 10 iterations ("zooming-ins"), 51 trial θ's per iteration, and a 60 second binsize when binning the shifted event lists from each trial θ in order to calculate the entropy. We collected the resulting θ_{min}'s from each random event list into a histogram.

We then determined a 95% confidence level for two cases, the sub-luminal case and the super-luminal case, by looking at all the θ's above and below 0 and finding the values $\theta_{95,+}$ and $\theta_{95,-}$, respectively, such that 95% were less than $|\theta_{95,\pm}|$ and 5% were greater than $|\theta_{95,\pm}|$. This yielded $\theta_{95,+} = 4.56 \times 10^{-3}$ sec/GeV and $\theta_{95,-} = -6.19 \times 10^{-3}$ sec/GeV. These upper limits give the values of θ which we could have detected with a 95% confidence for the sub-luminal and super-luminal cases, respectively. See Fig. 4.7 for the histogram of Monte Carlo simulation results, the 95% confidence levels, and where the experimental θ_{min}^{obs} falls in comparison.

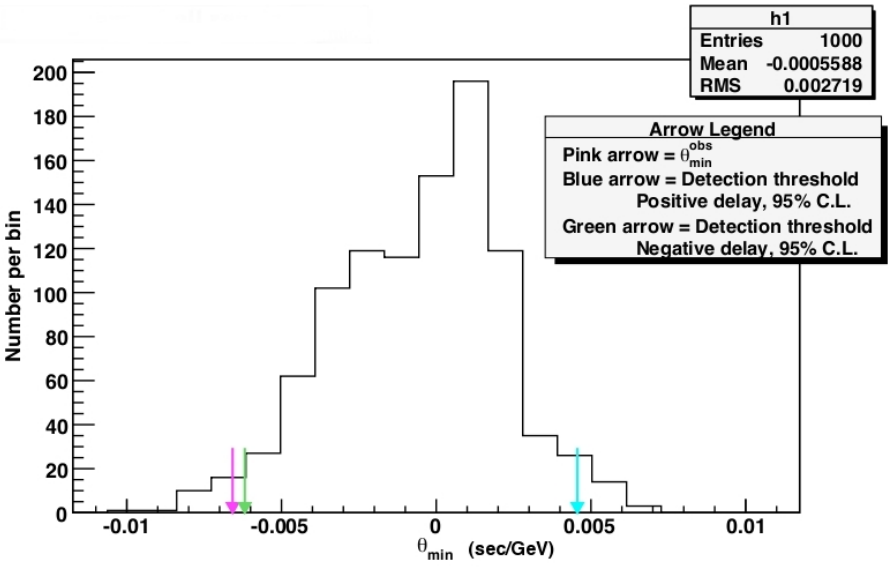

Figure 4.7: The collection of θ_{min}'s from $1,000$ simulated event lists using the linear model. θ_{min}^{obs} is the experimental θ.

Since 3.8% of the θ_{min}'s from the simulations were smaller (more negative) than the experimental θ_{min}^{obs}, we could not claim to see strong evidence for a definite time delay. Thus, we used Eqn. 2.3 to constrain ξ_1, and thus the quantum gravity energy scale, given our $|\theta_{min}^{obs}| = 6.58 \times 10^{-3}$ sec/GeV:

$$\xi > 0.169 \tag{4.1}$$

$$E_{QG} > 2.07 \times 10^{18} \text{ GeV} \tag{4.2}$$

We can also construct constraints using the 95% confidence levels derived from the histogram of simulated results, as these are more conservative and incorporate information from Monte Carlo simulations. For the sub-luminal case, with $|\theta_{95,+}| = 4.56 \times 10^{-3}$ sec/GeV, we find, with 95% confidence:

$$\xi > 0.244 \tag{4.3}$$

$$E_{QG} > 2.98 \times 10^{18}\ \text{GeV} \tag{4.4}$$

and for $|\theta_{95,-}| = 6.19 \times 10^{-3}$ sec/GeV, we find for the super-luminal case, with 95% confidence:

$$\xi > 0.180 \tag{4.5}$$

$$E_{QG} > 2.20 \times 10^{18}\ \text{GeV} \tag{4.6}$$

4.1.4 Quadratic Model Results

Using the Mrk 421 flare data and using the quadratic time delay expression $t'_i = t_i^{obs} - \theta((E_i^{obs})^2 - (E^2)_{avg})$, we found a $\theta_{min}^{obs} = -1.58x10^{-6}$ sec/GeV^2, which corresponds to minimized entropy of $S_{min} = 5.12$. See Fig.4.8 for the distribution of entropy versus test θ's.

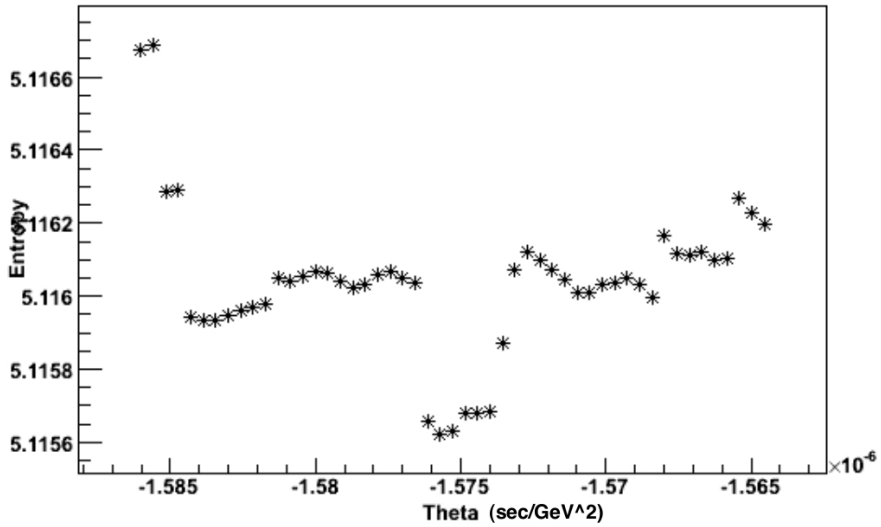

Figure 4.8: The experimental entropy versus θ distribution for the Mrk 421 data set using the quadratic model.

As with the linear case, in order to test statistical significance, we conducted a Monte Carlo simulation of $1,000$ random event lists, each created by scrambling the energy of the experimental event list. For each random light curve, we used 16 iterations ("zooming-ins"), 51 trial θ's per iteration, and a 60 second binsize when binning the shifted event lists from each trial θ in order to calculate the entropy. We collected the resulting θ_{min}'s from each random event list into a histogram.

Once again, we then determined a 95% confidence level for two cases, the sub-luminal case and the super-luminal case, by looking at all the θ's above and below 0 and finding the values $\theta_{95,+}$ and $\theta_{95,-}$, respectively, such that 95% were less than $|\theta_{95,\pm}|$ and 5% were greater than $|\theta_{95,\pm}|$. This yielded $\theta_{95,+} = 8.30 \times 10^{-7}$ sec/GeV^2 and $\theta_{95,-} = -1.31 \times 10^{-6}$ sec/GeV^2. These upper limits give the values of θ which we could have detected with a 95% confidence for the sub-luminal and super-luminal cases, respectively. See Fig. 4.9 for the histogram of Monte Carlo simulation results, the 95% confidence levels, and where the experimental θ_{min}^{obs} falls in comparison.

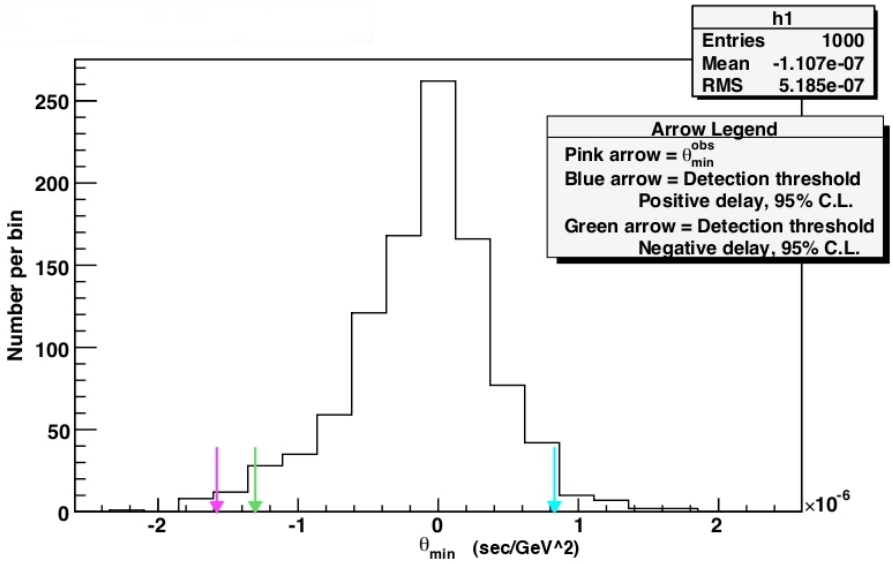

Figure 4.9: The collection of θ_{min}'s from $1,000$ simulated event lists using the quadratic model. θ_{min}^{obs} is the experimental θ_{min}.

Since 1.6% of the θ_{min}'s from the simulations were smaller (more negative) than the experimental θ_{min}^{obs}, we could not claim to see strong evidence for a definite time delay. (Note that only 1% being smaller would correspond to a statistical significance of 3 σ. We are therefore not at a level strong enough to claim a detection.) Thus, we used Eqn. 2.3 to constrain ξ_2, and thus the quantum gravity energy scale, given our $|\theta_{min}^{obs}| = 1.58 \times 10^{-6}$ sec/GeV^2:

$$\xi > 9.39 \times 10^{-9} \tag{4.7}$$

$$E_{QG} > 1.15 \times 10^{11} \text{ GeV} \tag{4.8}$$

Using our more conservative value of $|\theta_{95,+}| = 8.30 \times 10^{-7}$ sec/GeV^2, we find for the sub-luminal case, with 95% confidence:

$$\xi > 1.30 \times 10^{-8} \tag{4.9}$$

$$E_{QG} > 1.58 \times 10^{11} \text{ GeV} \tag{4.10}$$

and for $|\theta_{95,-}| = -1.31 \times 10^{-6}$ sec/GeV^2, we find for the super-luminal case, with 95% confidence:

$$\xi > 1.03 \times 10^{-8} \tag{4.11}$$

$$E_{QG} > 1.26 \times 10^{11} \text{ GeV} \tag{4.12}$$

4.2 Discrete Correlation Function

We ran the DCF analysis for 6 separate sources. These sources were chosen for the fact that they are all part of the Fermi - and subsequently Swift - monitoring programs, thus giving

them contemporaneous coverage with excellent statistics. More specifically, these sources were drawn from the results of the first three months of the Fermi all-sky survey campaign. For more information about Fermi bright source list that came from its first three months of operation and the companion list that identifies those associated with known blazars, please refer to Abdo et al. (2009b) and Abdo et al. (2009c). The sources were also chosen for their apparent variability in gamma rays, making them all good candidates for a correlation study. All Fermi data was downloaded on February 27, 2012; all Swift data was downloaded on March 8, 2012.

For each source, we ran two analyses - one using a binsize of 20 days and one using a binsize of 10 days. After the experimental results were obtained and we had pinpointed the maximum DCF and associated time lag, τ, we continued each analysis with a simulation of 100,000 random light curves in order to calculate the chance probability, which gives us a measure of the likelihood of obtaining our experimental results purely through random statistical fluctuations.

For each source, we plotted the full range of experimental time lags and corresponding DCFs; on top of these we plotted the 1 σ, 2 σ, and 3 σ confidence bands for both the negative DCFs and the positive DCFs. To calculate these confidence bands, for each time lag we collected all the positive simulated DCFs into one histogram and the negative simulated DCFs into another. For both cases, we found the DCF at which 68% (for 1 σ), 95% (for 2 σ), and 99% (for 3 σ) lay between 0 and that DCF. (Note that in all the DCF plots below, the pink curve corresponds to the 1 σ band, the blue curve corresponds to the 2 σ band, and the green curve corresponds to the 3 σ band.)

We calculated the confidence curves with respect to 0 as opposed to the mean of all the DCFs for each τ, since we expect that such a mean should be roughly 0 anyway. To verify

that this was indeed the case (and to also provide an additional check on the simulations), we calculated these mean DCFs for each τ and found that they were close enough to 0 with respect to each maximum DCF value (ie, 2 to 3 orders of magnitude smaller).

Please note that in the analysis, we have used the Fermi gamma-ray data as "light curve 1" and the Swift X-ray data as "light curve 2" (see Chapter 2 for an explanation of terms). With this designation, a positive time delay indicates that gamma-ray behavior occurred *before* the X-ray behavior - in other words, the X-ray behavior lags the gamma-ray behavior. Conversely, a negative time delay indicates that gamma-ray behavior occurred *after* the X-ray behavior - ie, the gamma-ray behavior lags the X-ray behavior.

What follows are descriptions of each of the 6 sources, their Fermi gamma-ray and Swift X-ray light curves, and the DCF plots for both a 20 day binsize analysis and a 10 day binsize analysis. For each of these analyses, we report the maximum DCF value found and its corresponding time lag - these values became the "experimental" DCF and the "experimental" time lag. These results are then summarized in Table 4.1.

4.2.1 3C 273

3C 273 is a quasi-stellar radio source (a classification which is commonly shortened to "quasar") with a redshift of 0.158. Originally part of the radio survey at Cambridge that resulted in the "3C Catalog" (short for "Third Cambridge" - see, eg, Bennett (1962)), it was one of many sources found to be associated with an optical component of stellar appearance (hence the name "quasi-stellar radio source"). Anomalies in the spectra, among other things, suggested these sources were not actually stars, and necessitated the search for an explanatory model. The study of 3C 273 led to the publishing of a now famous paper that explained the "anomalies" by identifying 3C 273 as "the nuclear region of a galaxy with a cosmological redshift of 0.158" (Schmidt (1963)). 3C 273 was thus the first source to be

classified as a quasar. This source has a large (on the order of kiloparsecs) jet that has been studied in great detail - see, for example, Uchiyama et al. (2006), for more information.

For the Fermi and Swift light curves used in our DCF study, please refer to Fig. 4.10.

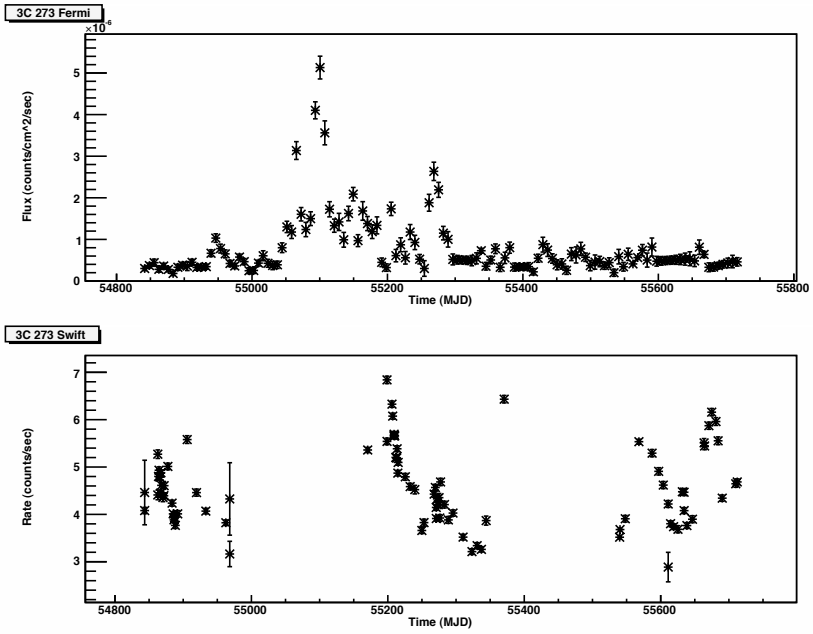

Figure 4.10: Light curves for **3C 273**. The top panel is Fermi data, and the bottom panel is Swift data.

Using a 20 day binsize, we found a maximum DCF of 0.562 ± 0.0925 at a time lag of -60 days. This was found to have a chance probability of 0.227 ± 0.00151. For a 10 day binsize, we found a maximum DCF of 0.650 ± 0.170 at a time lag of -70 days, with a chance probability of 0.142 ± 0.00119. The two resulting DCF plots can be found in Fig. 4.11.

4.2.2 3C 454.3

3C 454.3 (also called PKS 2251+158) is a flat-spectrum radio quasar (FSRQ, a sub-category of quasars - see, for example, Zhai et al. (2011)) with a redshift of 0.859. It is considered to be one of the more active of the FSRQs, particularly in optical and radio, and has had

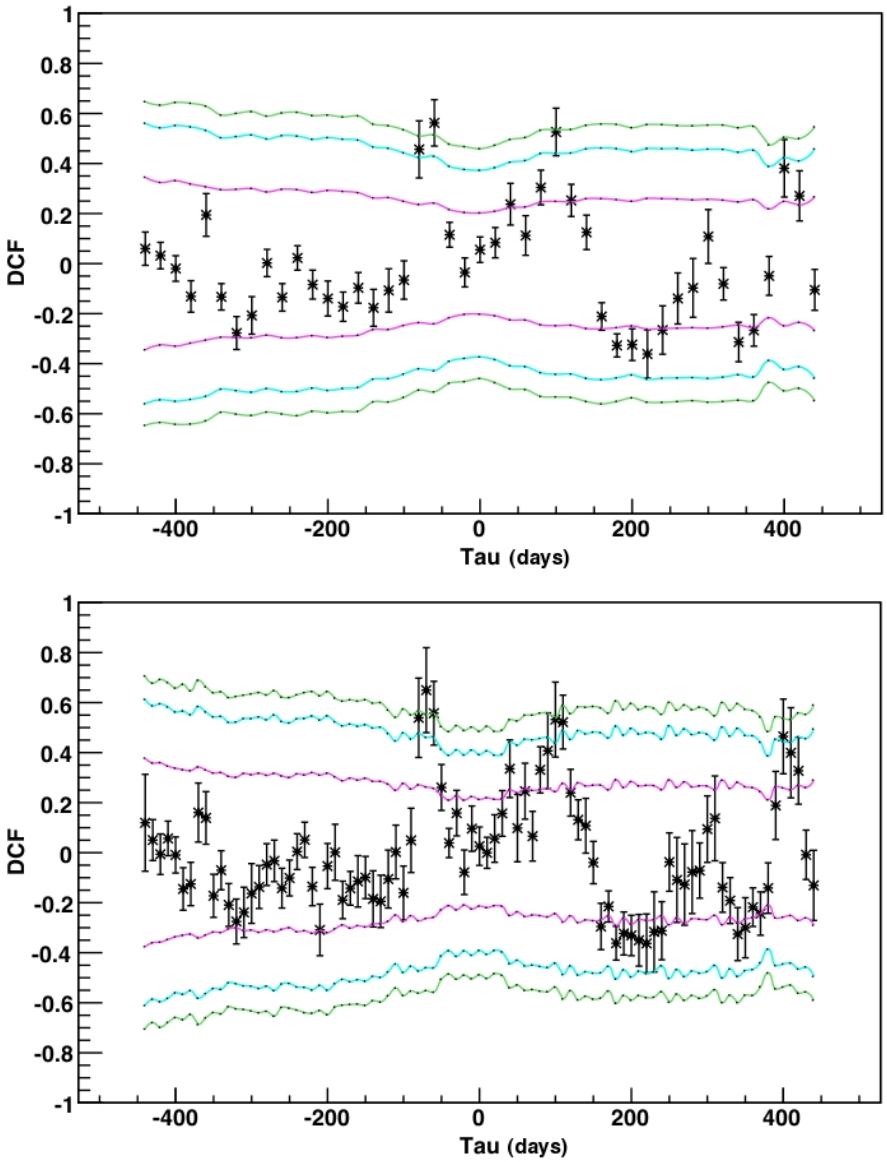

Figure 4.11: **3C 273:** The resulting experimental DCFs as a function of τ with confidence curves. The *top graph* shows the results for the analysis using a 20 day binsize, and the *bottom graph* shows the results for the analysis using a 10 day binsize.

numerous flaring episodes, making it an excellent candidate for extensive multiwavelength campaigns. For examples, see Vercellone et al. (2009), Pacciani et al. (2010), and Zhai et al. (2011). It has been shown to exhibit short-term variability - for example, in gamma rays, it has shown variability on scales of a week or shorter (Hartman et al. (1993)).

Please refer to Fig. 4.12 for the Fermi and Swift light curves used in our DCF study.

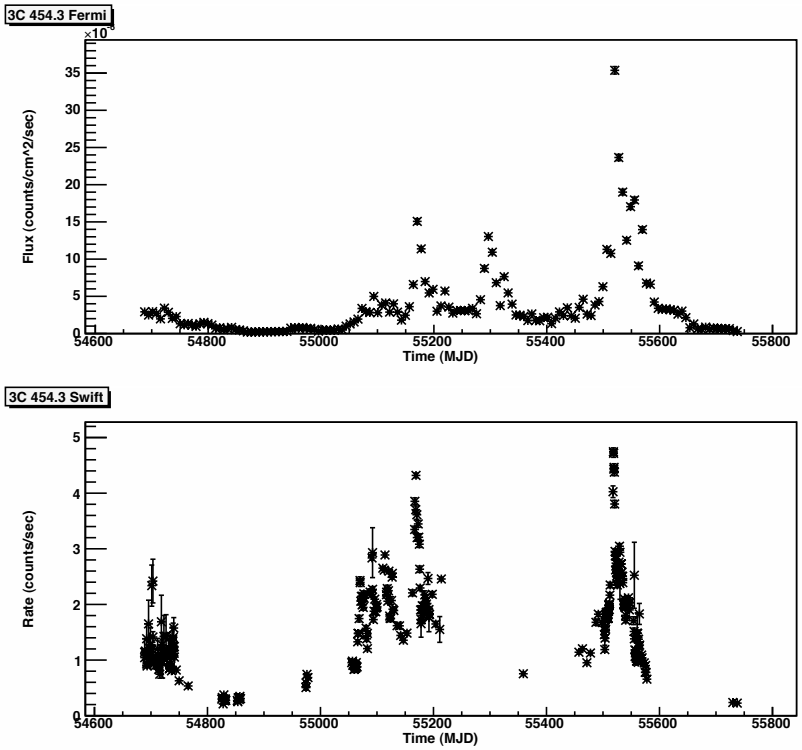

Figure 4.12: Light curves for **3C 454.3**. The top panel is Fermi data, and the bottom panel is Swift data.

Using a 20 day binsize, we found a maximum DCF of 0.547 ± 0.0485 at a time lag of 0 days. This had a chance probability of 0.397 ± 0.00199. For a 10 day binsize, we found a maximum DCF of 0.636 ± 0.0807 at a time lag of 0 days as well, with a chance probability of 0.226 ± 0.00150. The two resulting DCF plots can be found in Fig. 4.13

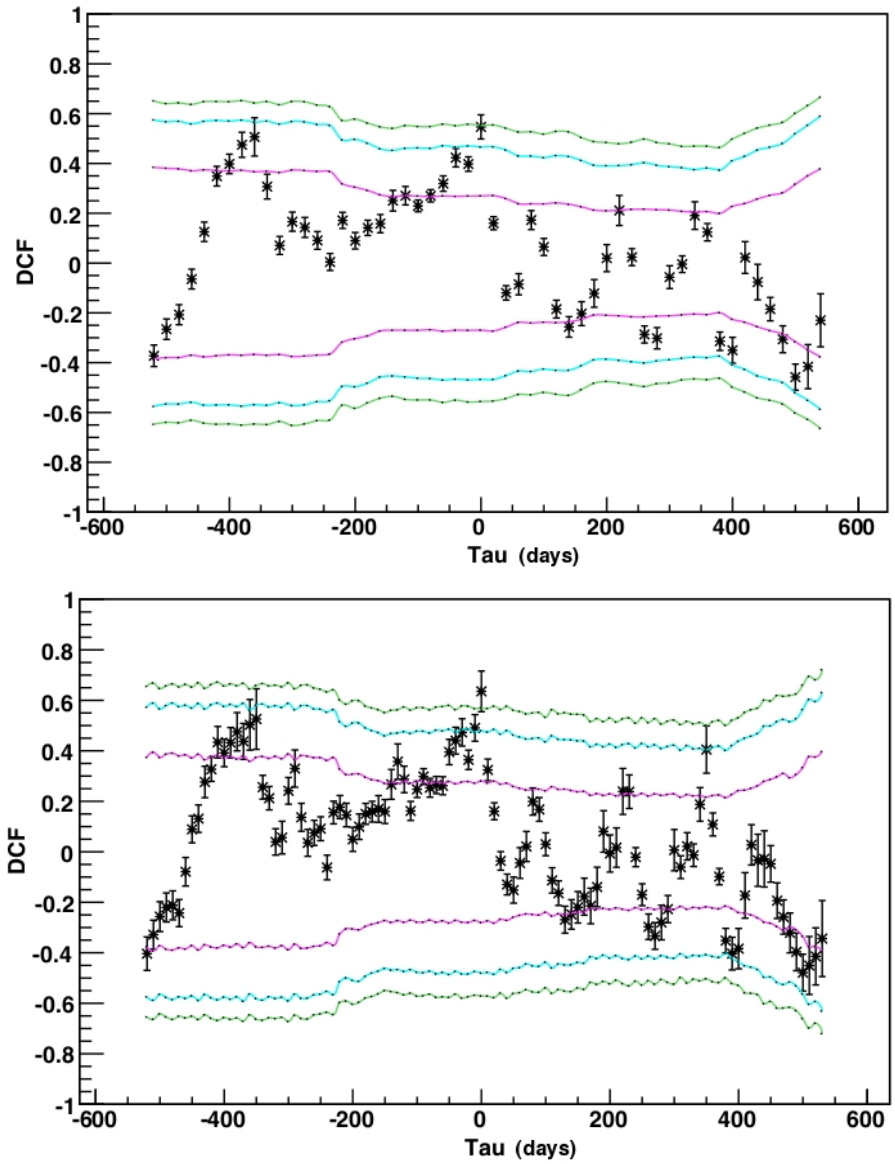

Figure 4.13: **3C 454.3:** The resulting experimental DCFs as a function of τ with confidence curves. The *top graph* shows the results for the analysis using a 20 day binsize, and the *bottom graph* shows the results for the analysis using a 10 day binsize.

4.2.3 3C 66A

3C 66A, along with 3C 66B, historically formed part of the 3C 66 radio galaxy. Further study determined that these two sources, which are separated by only 6', are actually unrelated (see, for example, Northover (1973)); 3C 66B has been identified as Fanaroff-Riley-I-type radio galaxy at a redshift of 0.0215 (see Aliu et al. (2009) for more information). 3C 66A, however, has been far more difficult to understand. Although it was originally identified as a quasar by Wills and Wills (1974), it was later reclassified as a BL Lacertae (abbreviated as BL Lac) object (see, for example, Maccagni et al. (1987)). BL Lac objects, named after the first source, BL Lacertae, to be so classified, are blazars with extreme variability in the optical and X-ray regions; they are also characterized by a having "very weak (if any) detectable emission lines" (Abdo et al. (2011a)). For an excellent discussion of BL Lac objects, please refer to Stein et al. (1976).

Because of the characteristically weak emission lines of BL Lac objects, redshifts are very often difficult to determine accurately. 3C 66A's redshift in particular is notoriously unknown. A value of 0.444 was initially calculated by Miller et al. (1978), and later "confirmed" by Lanzetta et al. (1993). However, both of these studies relied on the use of only one emission line, and thus the results were considered to be very uncertain by their authors. The redshift is still considered uncertain. Further study by Finke et al. (2008) placed a lower limit on the redshift at 0.096.

It should be noted that the VERITAS collaboration was the first experiment to detect 3C 66A in the very high-energy (> 100GeV) regime (Swordy (2008)). For an excellent discussion of the observations that led to the discovery, and for a good general review of the source, please refer to Acciari et al. (2009a).

The Fermi and Swift light curves for 3C 66A can be found in Fig. 4.14.

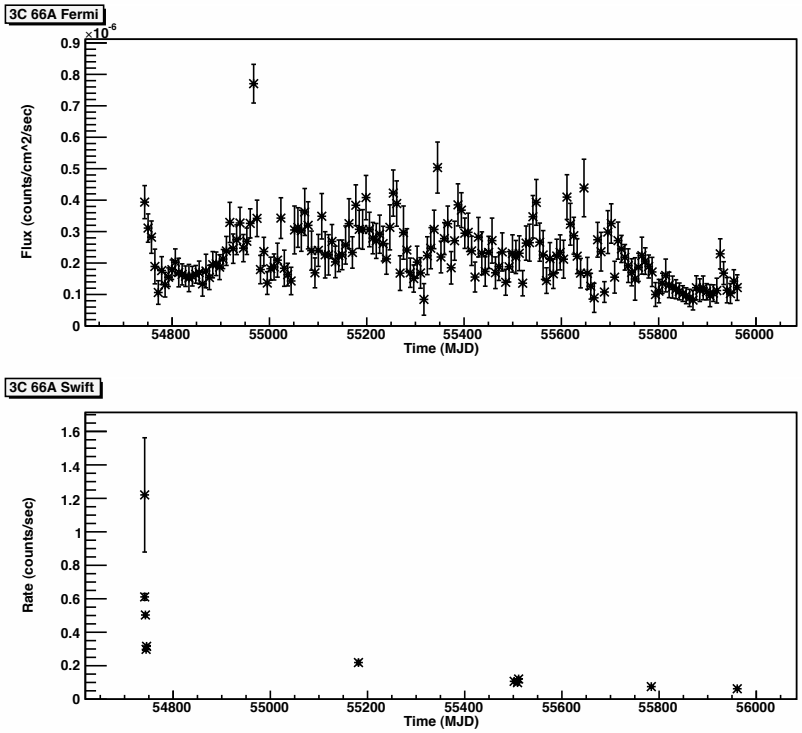

Figure 4.14: Light curves for **3C 66A**. The top panel is Fermi data, and the bottom panel is Swift data.

For a 20 day binsize, we found a maximum DCF of 2.89 ± 1.55 at a time lag of +20 days, with a chance probability of 0.191 ± 0.00138. Using a 10 day binsize, we found a maximum DCF of 5.43 ± 3.99 at a time lag of +130 days. This had a chance probability of 0.171 ± 0.00131. The two resulting DCF plots can be found in Fig. 4.15

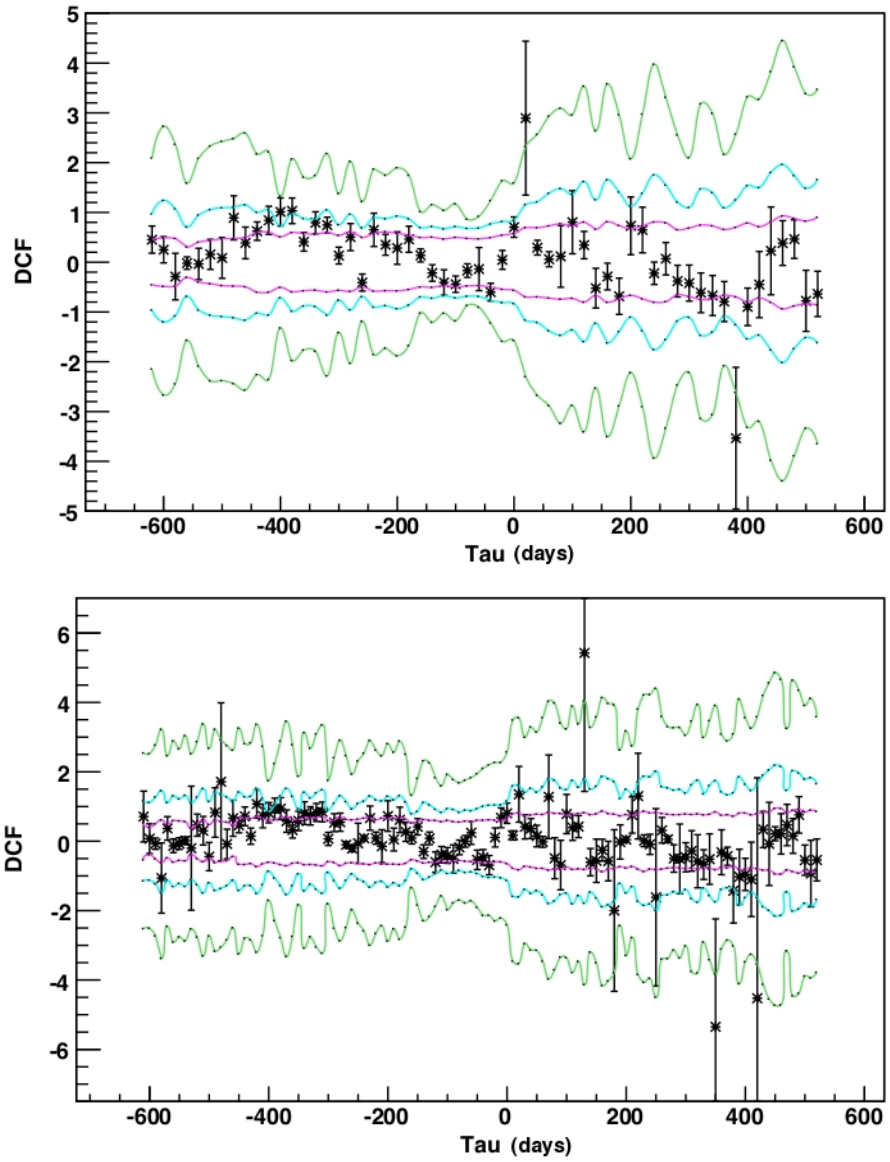

Figure 4.15: **3C 66A:** The resulting experimental DCFs as a function of τ with confidence curves. The *top graph* shows the results for the analysis using a 20 day binsize, and the *bottom graph* shows the results for the analysis using a 10 day binsize.

4.2.4 3C 279

Similar to 3C 454.3, 3C 279 is a very active FSRQ, and has been the subject of many historical firsts - for example, it was the first quasar discovered to emit in the gamma-ray regime (Hartman et al. (1992)) and the first to demonstrate superluminal motion (Whitney et al. (1971)). It has a redshift of 0.536, and has shown great variability across all wavelengths; for example, the X-ray satellite *Ginga* saw a 20% X-ray flux change on sub-hour scales (Makino et al. (1989)). As such, it is often been the subject of multiwavelength campaigns - see, for one example, Aleksić et al. (2011)).

For the purposes of the DCF analysis, please refer to Fig. 4.16 for the Fermi and Swift light curves.

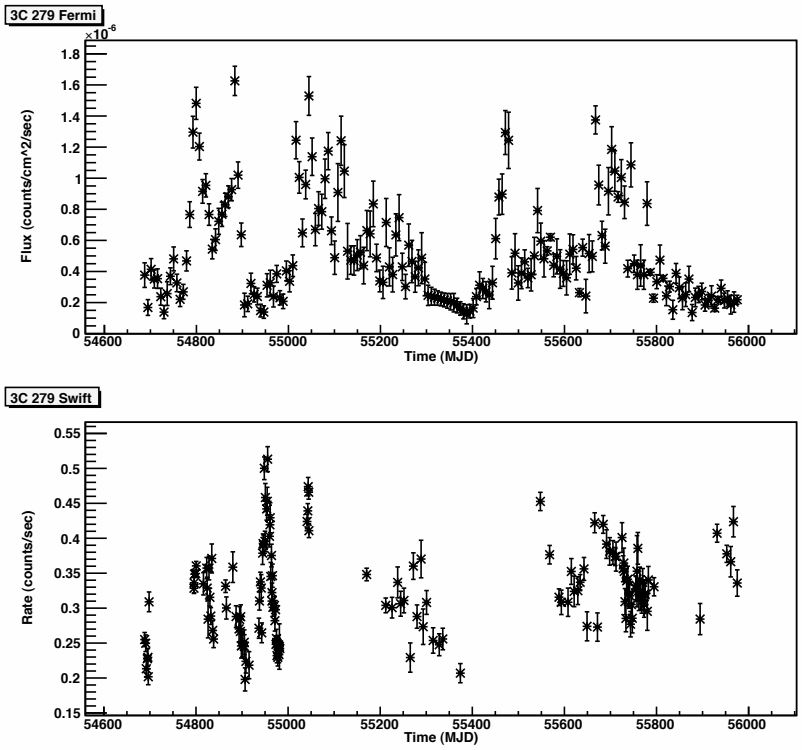

Figure 4.16: Light curves for **3C 279**. The top panel is Fermi data, and the bottom panel is Swift data.

Using a 20 day binsize, we found a maximum DCF of 0.486 ± 0.0762 at a time lag of -520 days. This had a chance probability of 0.223 ± 0.00149. For a 10 day binsize, we found a maximum DCF of 0.547 ± 0.119 at a time lag of -520 days, with a chance probability of 0.304 ± 0.00174. The resulting two DCF plots can be found in Fig. 4.17

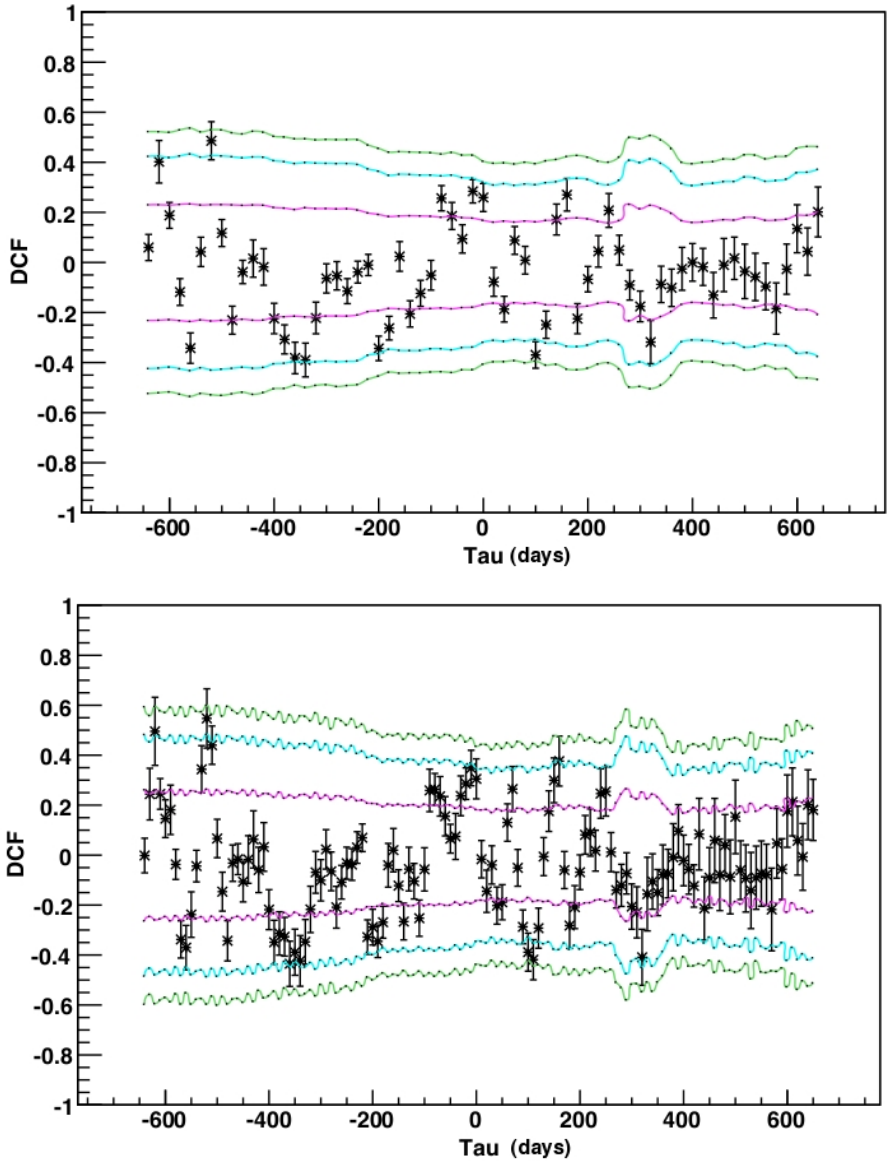

Figure 4.17: **3C 279:** The resulting experimental DCFs as a function of τ with confidence curves. The *top graph* shows the results for the analysis using a 20 day binsize, and the *bottom graph* shows the results for the analysis using a 10 day binsize.

4.2.5 PKS 0235+164

PKS 0235+165 (AO 0235+164) is a BL Lac object with a very complicated surrounding environment (Raiteri et al. (2006)). It was first identified as a BL Lac object by Spinrad and Smith (1975) due to "optical and radio variability and featureless optical spectrum". The complexity of its environment makes the study of this source particularly difficult. According to Cohen et al. (1987), there are three redshifts that have been identified with this source - one from an absorption spectrum, at 0.851, one from an emission spectrum, at 0.940, and one from both emission and absorption, at 0.524. The source PKS 0235 is generally identified with the redshift of 0.940. A cluster of four galaxies has been found at the redshift of 0.524 (for summary, see, for example, Rabbette et al. (1996)), which may be interacting and thus contaminating PKS 0235 (see Raiteri et al. (2006) for more information). The source exhibits strong flaring episodes in radio, infrared, and optical (Rabbette et al. (1996)). This source has been found to exhibit short-term flaring on a scale of less than 10 days (Sasada et al. (2011)).

Please refer to Fig. 4.18 for the Fermi and Swift light curves.

For a 20 day binsize, we found a maximum DCF of 0.371 $\pm$ 0.140 at a time lag of 0 days. This had a chance probability of 0.961 $\pm$0.00310. Using a 10 day binsize, we found a maximum DCF of 0.471 $\pm$ 0.210 at a time lag of 0 days, with a chance probability of 0.957 $\pm$ 0.00309. The resulting two DCF plots can be found in Fig. 4.19

4.2.6 PKS 1510-089

PKS 1510, originally part of the Parks 2700 MHz survey, is an FSRQ with a redshift of 0.360 (Thompson et al. (1990)). Egret detected it in gamma rays (Hartman et al. (1999)), and it has been the subject of several multiwavelength studies - see, for example, Kataoka et al. (2008) and Abdo et al. (2010a), the latter of which is an extensive campaign led by the

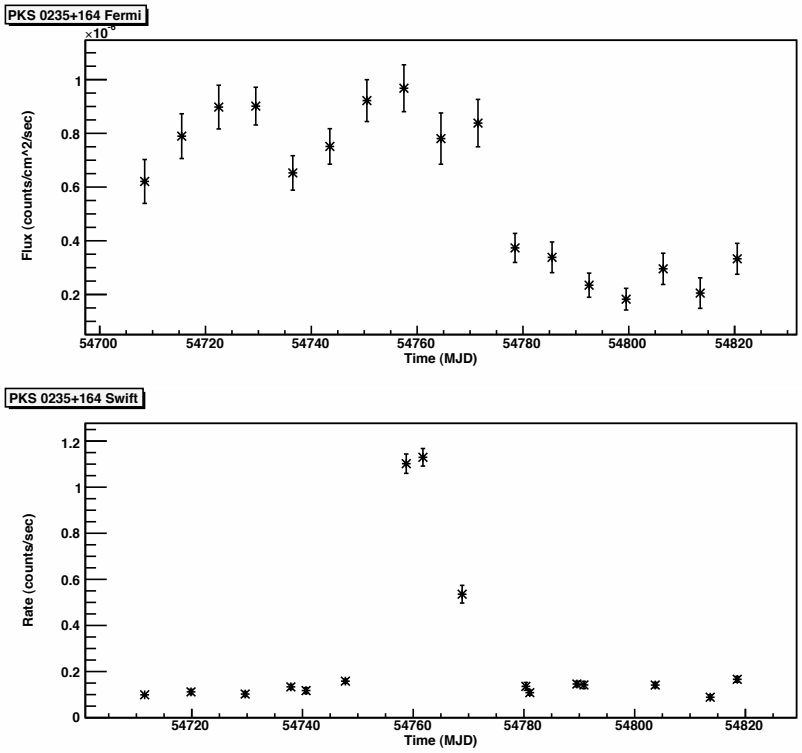

Figure 4.18: Light curves for **PKS 0235+164**. The top panel is Fermi data, and the bottom panel is Swift data.

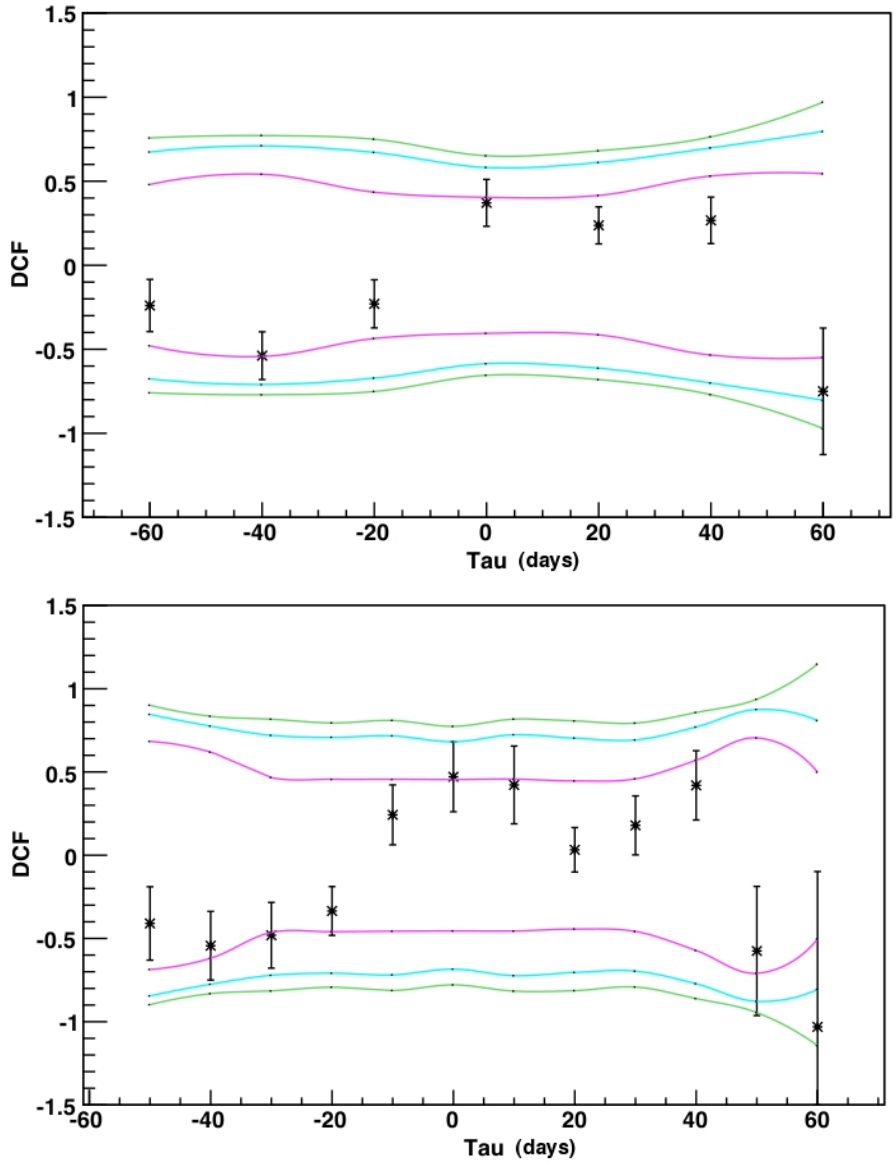

Figure 4.19: **PKS 0235+164:** The resulting experimental DCFs as a function of τ with confidence curves. The *top graph* shows the results for the analysis using a 20 day binsize, and the *bottom graph* shows the results for the analysis using a 10 day binsize.

Fermi LAT team. Similarly to PKS 0235+164, this source has been found to exhibit flaring on short time scales - ie, less than 10 days (Sasada et al. (2011)).

Please refer to Fig. 4.20 for the Fermi and Swift light curves.

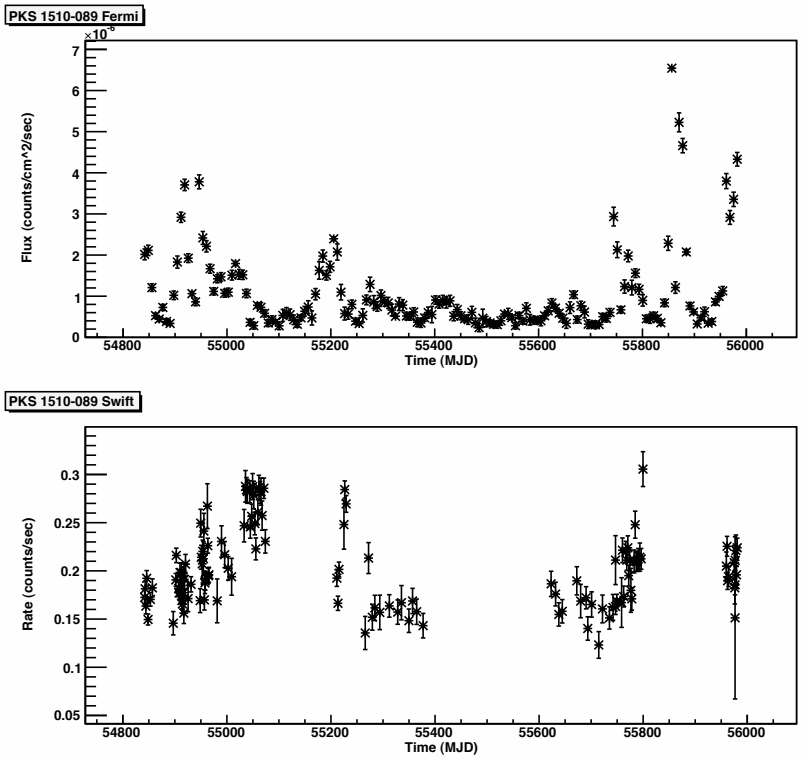

Figure 4.20: Light curves for **PKS 1510-089**. The top panel is Fermi data, and the bottom panel is Swift data.

For a 20 day binsize, we found a maximum DCF of 0.494 ± 0.0799 at a time lag of +220 days. This had a chance probability of 0.339 ± 0.00184. Using a 10 day binsize, we found a maximum DCF of 0.560 ± 0.104 at a time lag of +210 days, with a chance probability of 0.267 ± 0.00163. The two resulting DCF plots can be found in Fig. 4.21

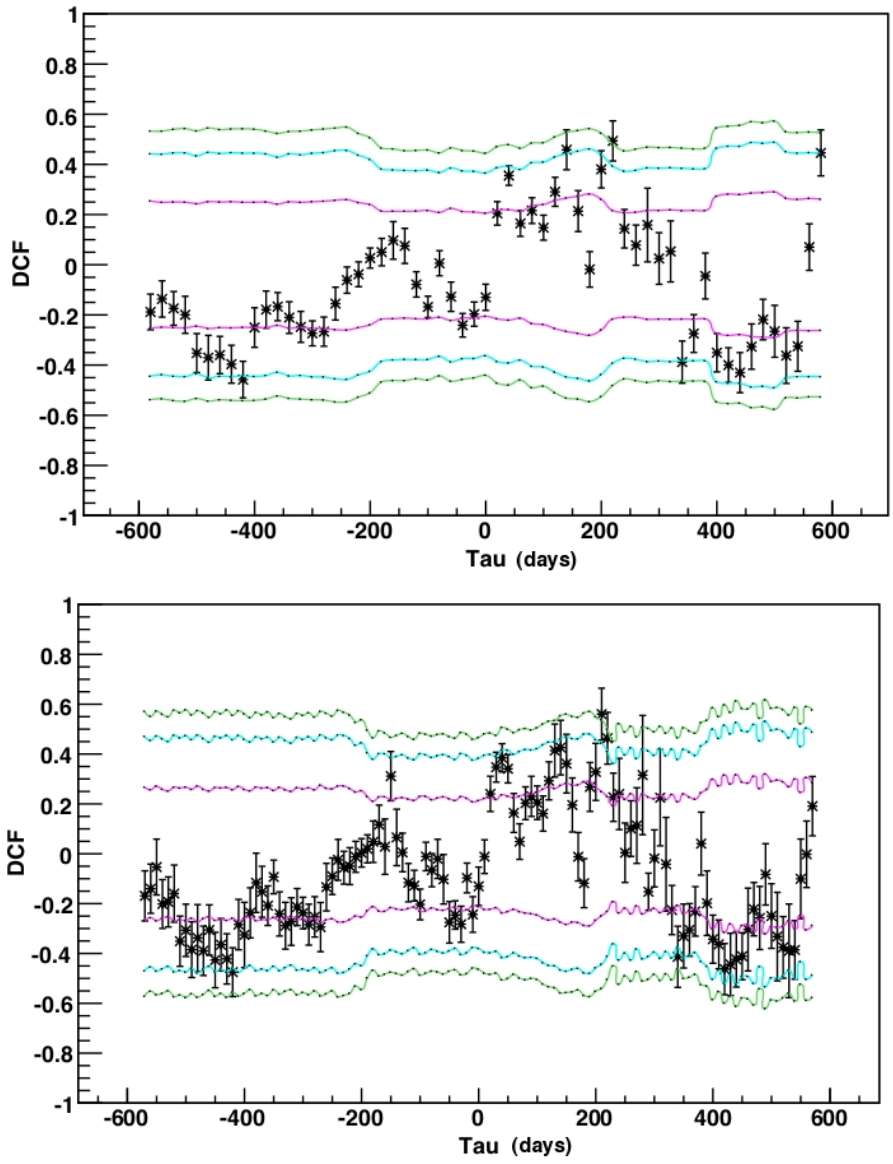

Figure 4.21: **PKS 1510-089:** The resulting experimental DCFs as a function of τ with confidence curves. The *top graph* shows the results for the analysis using a 20 day binsize, and the *bottom graph* shows the results for the analysis using a 10 day binsize.

Source	# Fermi Data Points	# Swift Data Points	Binsize	τ	DCF	DCF Error	P	P Error
3C 273	126	88	20	-60	0.562	0.0925	0.227	0.00151
			10	-70	0.650	0.170	0.142	0.00119
3C 454.3	150	280	20	0	0.547	0.0485	0.397	0.00199
			10	0	0.636	0.0807	0.226	0.00150
3C 66A	174	10	20	+20	2.89	1.55	0.191	0.00138
			10	+130	5.43	3.99	0.171	0.00131
3C 279	184	148	20	-520	0.486	0.0762	0.223	0.00149
			10	-520	0.547	0.119	0.304	0.00174
PKS 0235+164	16	16	20	0	0.371	0.140	0.961	0.00310
			10	0	0.471	0.210	0.957	0.00309
PKS 1510-089	164	126	20	+220	0.494	0.0799	0.339	0.00184
			10	+210	0.560	0.104	0.267	0.00163

Table 4.1: Collection of results from the DCF analysis using 6 different astrophysical sources. P is the chance probability, and P Error is the error on the chance probability. The reported τs, DCFs, and DCF Errors are the experimental values. Both binsize and τ carry units of days. A positive time lag indicates the X-ray behavior lags the gamma-ray behavior, and a negative time lag indicates the gamma-ray behavior lags the X-ray behavior.

4.2.7 An Alternative Method For Generating Random Light Curves

One of the more difficult aspects of the DCF analysis was developing a method, for which there are many possibilities, to generate random light curves for the simulations. As mentioned in Chapter 2, for example, Jordan (2004) used the pile-up of flares with rise and fall times comparable to data. Additionally, Timmer and Koenig (1995) proposed a method that relied on generating noise with amplitudes distributed according to a power law. To do so required us to estimate the spectral index from the data, which proved to be difficult owing to statistical fluctuations in the measured amplitude distribution. We ultimately settled on the method of scrambling the phases of the flux values in Fourier space.

We did decide to investigate whether there would be any benefit to Fourier transforming the *log* of the flux of the data when simulating the random light curves. There is no hard evidence for how best to characterize the shape of flares, and we thought it worthwhile to simulate random light curves using the Fourier transform of the log of the flux of the data, in addition to just the Fourier transform of the flux. We ran the analysis using the same parameters as previously, with the only difference being that we took the natural log of the flux before taking the Fourier transform (which necessitated the extra step of exponentiating the simulated flux values after performing the inverse-Fourier transform). The summary of this analysis, compared to the original analysis, can be found in Table 4.2. Note that of course the experimental values are not different; the differences lie in the resulting chance probabilities.

Source	**Binsize**	τ	**DCF**	**DCF Error**	**P**	**P Error**	$\mathbf{P_{log}}$	$\mathbf{P_{log}}$ **Error**
3C 273	20	-60	0.562	0.0925	0.227	0.00151	0.375	0.00194
	10	-70	0.650	0.170	0.142	0.00119	0.315	0.00177
3C 454.3	20	0	0.547	0.0485	0.397	0.00199	0.527	0.00229
	10	0	0.636	0.0807	0.226	0.00150	0.394	0.00199
3C 66A	20	+20	2.89	1.55	0.191	0.00138	0.280	0.00167
	10	+130	5.43	3.99	0.171	0.00131	0.204	0.00143
3C 279	20	-520	0.486	0.0762	0.223	0.00149	0.261	0.00161
	10	-520	0.547	0.119	0.304	0.00174	0.353	0.00188
PKS 0235+164	20	0	0.371	0.140	0.961	0.00310	0.97	0.00311
	10	0	0.471	0.210	0.957	0.00309	0.979	0.00313
PKS 1510-089	120	+220	0.494	0.0799	0.339	0.00184	0.649	0.00255
	10	+210	0.560	0.104	0.267	0.00163	0.573	0.00239

Table 4.2: A comparison of DCF analysis results: Fourier transforming the flux of the data versus Fourier transforming the log of the flux of the data. P is the chance probability from simulations Fourier transforming just the flux, while P_{log} is the equivalent from Fourier transforming the log of the flux. P Error and P_{log} Error are the errors on their respective chance probabilities. The reported τs, DCFs, and DCF Errors are the experimental values. Both binsize and τ carry units of days. A positive time lag indicates the X-ray behavior lags the gamma-ray behavior, and a negative time lag indicates the gamma-ray behavior lags the X-ray behavior.

Chapter 5

Discussion of Analysis Results

5.1 Lorentz Invariance Violation

As discussed in the Results chapter, although we did not see evidence for a time delay effect, we were able to place a strong constraint on E_{QG} of 2.98×10^{18} GeV in the linear, sub-luminal case and 1.58×10^{11} GeV in the quadratic, sub-luminal case, both with a 95% confidence level. To help ascertain the validity of these results, we constructed a test event list by injecting a known time delay using the linear model into a pre-existing event list; we then ran the test event list through the code to ensure that the code could properly identify the injected time delay.

5.1.1 A Test of the Method

The ideal event list is one with structure - a purely random event list, without peak-like structure, would not contain enough information to enable a strong enough test on the code. Thus, to construct our test event list, we used our actual Mrk 421 event list with the cuts already described as a starting point. We picked a θ (which recall is about $= \Delta t/\Delta E$) 10 times larger than the experimental $\theta^{obs}_{min} = -6.58 \times 10^{-3}$ sec/GeV, which works out to -0.0658 sec/GeV. We injected this into the real data list by inverting the general time delay expression to become:

$$t_i' = t_i^{obs} + \theta(E_i^{obs} - E_{avg}) \tag{5.1}$$

With this new event list, we executed the entire program. After 10 iterations, we found an experimental θ_{min}^{obs} of -0.0723 sec/GeV. We then ran the Monte Carlo simulations, the results of which can be found in Fig. 5.1.

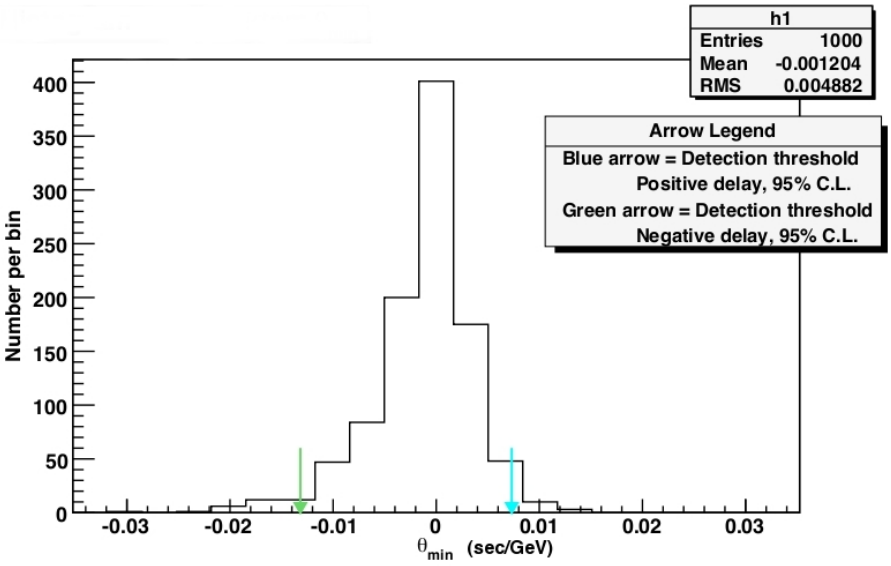

Figure 5.1: Collection of minimizing θ's for 1000 random event lists using the post-cut Mrk 421 event list with an injected θ of -0.0658 sec/GeV.

The experimental θ_{min}^{obs} is well outside the reaches of the histogram summary of the simulations - so much so that it does not even register on the scale of the histogram - thus suggesting that the experimental θ_{min}^{obs} that the code picked out was in fact a "true" θ, as opposed to one that is simply due to random statistical fluctuations. Since of course we purposefully injected this θ, we *expect* the code to recover the value, and we expect that this result could not be attributed purely to chance.

5.1.2 A Comparison of This Work to Existing Results

For a little over a decade, since the publication of Amelino-Camelia et al. (1998), there have been a number of different studies placing constraints on the quantum gravity energy scale. Over the years, as both the observational instruments and the techniques used to derive constraints grew more sophisticated, the resulting constraints began to approach the Planck energy scale and, in the case of Abdo et al. (2009a), surpass it. Please refer to Table 5.1 for a timeline of important constraints. Note that Biller et al. (1999) gave the first published limit on the quantum gravity energy scale. They did so using flare data from Mrk 421, using the Whipple observatory.

Year	Target	Method	$\mathbf{E_{QG,1}}$	$\mathbf{E_{QG,2}}$	Ref
1999	Mrk 421	Peak Timing	$> 6.0 \times 10^{16}$		Biller et al. (1999)
1999	Crab Pulsar	Peak Timing	$> 1.8 \times 10^{15}$		Kaaret (1999)
1999	GRB 930131		$> 8.3 \times 10^{16}$		Schaefer (1999)
2000	5 GRBs	Wavelet analysis	$\gtrsim 10^{15}$		Ellis et al. (2000)*
2003	9 GRBs	Wavelet analysis	$\geq 6.9 \times 10^{15}$	$\geq 2.9 \times 10^{6}$	Ellis et al. (2003)*
2003	Crab Pulsar and Mrk 421 and Mrk 501	HE photon decay to e^-/e^+ pairs	$> 3.66 \times 10^{18}$		Stecker (2003)
2004	GRB 021206	Peak Timing	$> 1.8 \times 10^{17}$	$> 5.5 \times 10^{7}$	Boggs et al. (2004)*
2006/2008	35 GRBs	Wavelet analysis	$> 1.4 \times 10^{16}$		Ellis et al. (2006)*, Ellis et al. (2008)
2007/2008	Mrk 501	Energy-Cost Function	$> 2.1 \times 10^{17}$	$> 2.6 \times 10^{10}$	MAGIC Collaboration et al. (2008)
2008	PKS 2155-304	Peak Timing	$> 7.2 \times 10^{17}$	$> 1.4 \times 10^{9}$	Aharonian et al. (2008)
		Wavelet analysis	$> 5.2 \times 10^{17}$		Aharonian et al. (2008)
2009	GRB 090510	Dis-Can	$> 1.49 \times 10^{19}$		Abdo et al. (2009a)
		Associating 31 GeV photon with start of observed emission	$> 1.45 \times 10^{19}$		Abdo et al. (2009a)
2011	PKS 2155-304†	Likelihood Fit	$> 2.1 \times 10^{18}$	$> 6.4 \times 10^{10}$	HESS Collaboration et al. (2011)
2012	Mrk 421	DisCan, positive delay	$> 2.98 \times 10^{18}$	$> 1.58 \times 10^{11}$	This work
		DisCan, negative delay	$> 2.15 \times 10^{18}$	$> 1.26 \times 10^{11}$	This work

Table 5.1: Previous constraints on the quantum gravity energy scale. $E_{QG,1}$ is the energy constraint using a linear (n=1) model, while $E_{QG,2}$ is the energy constraint using a quadratic (n=2) model. All energy constraints carry units of GeV and, unless otherwise noted, these constraints are all for the sub-luminal case. Those references marked with a * did not take into account the extra factor of $(1+z)$ in, for example, Eqn. 1.5. This mistake was found by Jacob and Piran (2008). The study marked with a † is an update to Aharonian et al. (2008).

We have also taken the best linear term constraints for each source and plotted them to scale on a map of the sky in galactic coordinates (see Fig. 5.2). The idea is that the degree of Lorentz invariance violation may depend on the direction of propagation. To test this, one should execute a population study using sources distributed across the whole sky. From our plot, we can see that there are strong constraints for sources close to the galactic poles, but that there is a dearth of constraints near the galactic plane (particularly near the galactic center). To better test this idea, future studies should apply the LIV analysis to sources in that region.

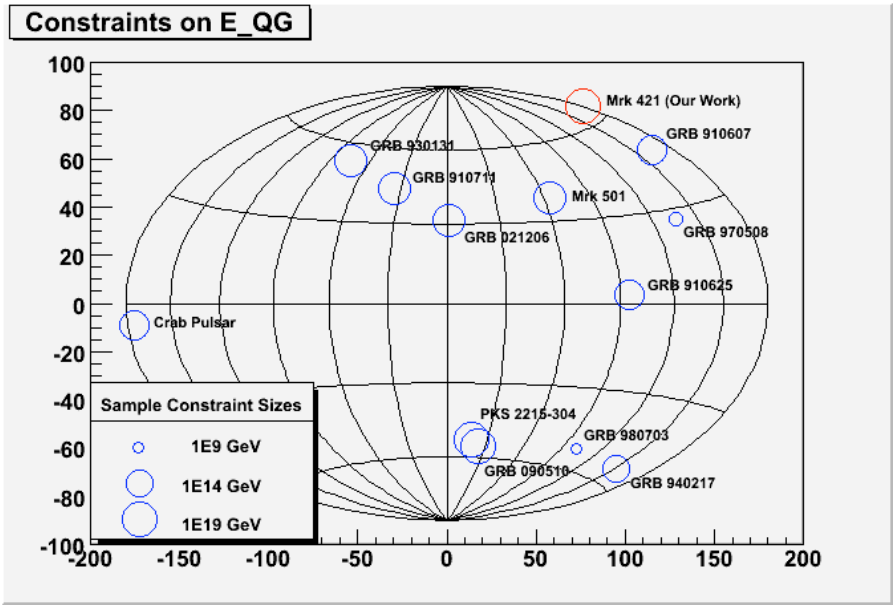

Figure 5.2: Collection of current best LIV linear constraints per source, combined with our own. Note that galactic coordinates are used

When compared to these key (sub-luminal) constraints, our sub-luminal constraint, 2.98×10^{18} GeV, is competitive with the better, more recent ones. Most importantly, our constraint begins to probe the Planck energy, as it is less than the Planck energy scale by only an order of magnitude. Furthermore, our quadratic constraint appears to be one of the best found

thus far.

In principle, no evidence for time delay essentially equates to no current evidence for LIV effects. However, we cannot conclusively rule out the idea that perhaps there is a "conspiracy of nature" in which any source effects that may cause a time delay are cancelled exactly by LIV propagation effects. (See, for instance, the discussion in HESS Collaboration et al. (2011)). As this seems far-fetched, like HESS Collaboration et al. (2011) we prefer to conclude that our result instead points to no propagation effect that we can currently detect.

5.1.3 A Note on Combining LIV Constraints With Quantum Gravity Models

Establishing with confidence the existence of a LIV-induced time delay would be an important result in and of itself. Most of the studies of the potential LIV effect focus on the task of searching for and evaluating calculated constraints. However, as those constraints begin to approach and, in some cases, surpass the Planck energy level, the constraints can become useful in placing limits on quantum gravity scenarios.

Abdo et al. (2009a), which first applied the DisCan method to LIV probes, discussed the fact that most quantum gravity scenarios that predict a linear (n=1) correction term to the photon dispersion relation require the quantum gravity scale to be less than or equal to the Planck energy scale. In that work, the fact that even their most conservative constraint is larger than the Planck energy "greatly reduce[s] the parameter space for n=1 models". They state that their results provide strong evidence against quantum gravity models that contain a linear correction term. Unfortunately, although our constraint is within an order of magnitude of the Planck energy, it does not surpass it; we thus cannot make similar claims from our results.

5.2 Discrete Correlation Function

The LIV study necessitated the assumption that there was no energy-dependent time delay inherent at the source emission site. We assumed that any energy-dependent time delay came from propagation effects alone. There are two ways one could strengthen this assumption. The first is to conduct a population study by applying the DisCan method to several different sources at varying redshifts. In both the linear and quadratic models, the θ parameter is dependent on the time delay. This time delay, and thus θ, should increase with redshift, since the delay effect accumulates with larger distances. Any time delay effects inherent to the source should not scale with redshift. Thus, a population study could help distinguish a "true" LIV effect from any source effects. Doing this kind of population research using the DisCan method would be an excellent area for further study.

The second way to strengthen the assumption is to try to better understand source physics. One way of doing so is through the DCF study presented in this thesis. By either confirming or not seeing correlated behavior between energy bands - in this case, X-ray and GeV gamma-ray - we can begin to understand, for example, the emission mechanisms that generated the radiation used for the LIV study. In particular, confirmation of a time lag can be accounted for in the θ-parameterized time delay expression. Conversely, conclusions that there was no evidence of a time lag can help strengthen the original assumption. It is with this in mind that we executed the DCF study.

5.2.1 Discussion of Experimental Results

Based on the results from the DCF analysis and simulations, we can conclude that we did not see any significant correlated behavior between X-rays and gamma rays in any of the sources, for either a 10 day binsize or a 20 day binsize, or for either Fourier transforming just the flux or the log of the flux. We draw this conclusion based on the fact that none of

our chance probabilities were small ($\ll 0.01$). There are also no clear trends across all the sources used.

To strengthen our conclusions, we can look at the distribution of chance probabilities. Because our simulations did not provide evidence for correlated behavior, we expect the chance probabilities to be randomly distributed from 0 to 1, with an average around 0.5. If we expected consistent evidence of a correlation, we would expect a cluster of chance probabilities close to 0. We looked at the distribution of chance probabilities from all four analysis scenarios - using a 20 day binsize and a 10 day binsize, each applied to Fourier transforming the flux of the data and the log of the flux of the data in simulations. For the plot of the distributions of these chance probabilities, please refer to Fig. 5.3.

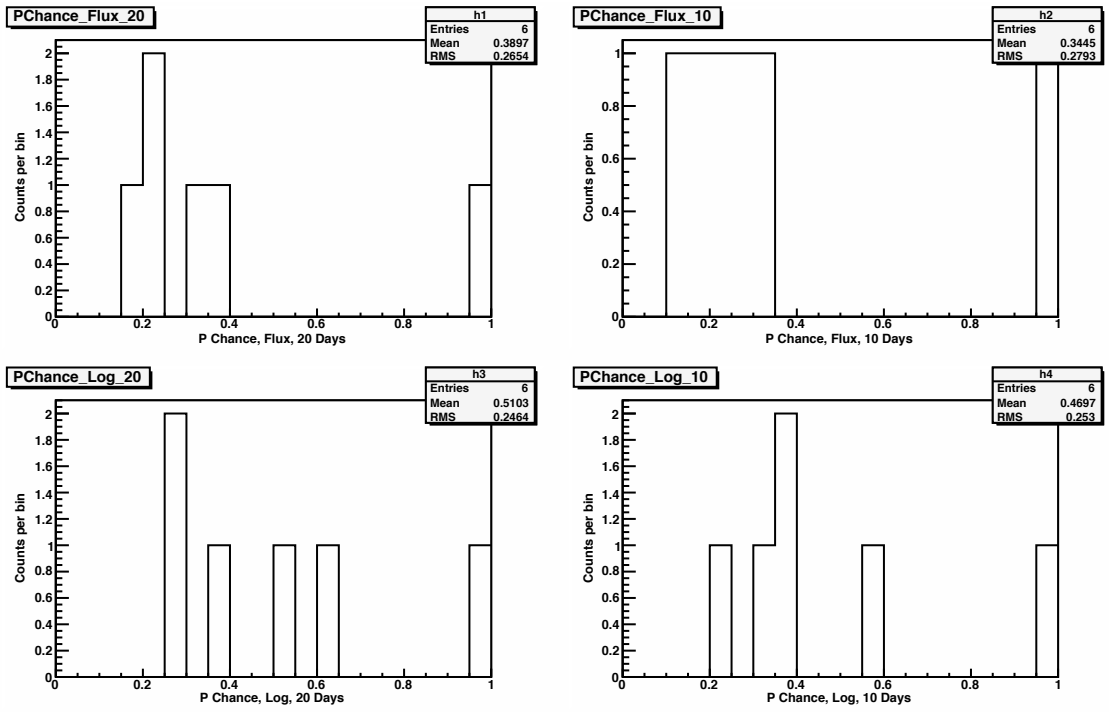

Figure 5.3: Histograms of the chance probabilities from all 6 sources, for all four DCF analysis scenarios. The top left plot shows the chance probabilities from Fourier transforming just the flux and using a 20 day binsize, while the top right panel shows results from transforming just the flux and using a 10 day binsize. The bottom left plot shows the chance probabilities from transforming the log of the flux and using a 20 day binsize, while the bottom right plot shows the results from transforming the log of the flux and using a 10 day binsize.

For six sources - and thus six chance probabilities - there are four possible configurations of chance probability distributions: 6 less than (or greater than) 0.5, 5 less than (or greater than) 0.5, 4 less than (or greater than) 0.5, and 3 less than and greater than 0.5. If we use a binomial distribution to calculate the probability of each of these configurations, we see that having 3 on either "side" of 0.5 is the most probable. However, in both scenarios using the Fourier transform of the flux (i.e., using both a 20 day binsize and a 10 day binsize), we had 5 chance probabilities less than 0.5 and only 1 greater than. The probability of this occurring is $6/2^6$ (about 9.4%). For chance probabilities that resulted from Fourier transforming the log of the flux, there were 3 less than and 3 greater than 0.5 using a 20 day binsize, and 4 less than and 2 greater than 0.5 using a 10 day binsize. The former has the greatest probability of occurring, with a probability of $20/2^6$ (about 31.25%), while the latter has a probability of $15/2^6$ (about 23.4%) of occurring. Were any of these configurations to be considered "rare" (i.e., with a probability of occurring $\ll 1\%$), the results could be considered significant. However, none of these distributions can be considered rare, which strengthens our conclusion that we have not found evidence for correlated behavior at the time lags investigated.

The distributions of chance probabilities hint that using the log of the flux in the simulations could be better than just the flux, since using both a 10 day binsize and a 20 day binsize resulted in distributions that were statistically more probable. However, these hints are not sufficient to enable us to make any strong claims.

It should be noted that our sample size is extremely small. We only used 6 sources for this analysis; even the least probable configuration of chance probabilities, with 6 less than, or greater than, 0.5, still has a probability of 1/64 (about 1.56%) of occurring, which is certainly not $\ll 1\%$. Future studies may wish to use a larger sample size of sources of varying types and at varying redshifts.

5.2.2 Outstanding Issues in Source Physics

There are still a number of outstanding issues surrounding blazar physics, including questions regarding emission mechanisms, jet properties (i.e., characterizations of the magnetic field), and the details of emission models, the latter of which is especially relevant to this discussion. One of the primary questions regards the specifics of inverse-Compton emission models responsible for the higher energy radiation peak in blazar spectral energy distributions (SEDs). As discussed briefly in the Introductory chapter, while it is commonly agreed that synchrotron emission is responsible for lower energy emission, there are still questions about the nature of the higher energy emission. Inverse-Compton scattering is a popular explanation, but there are still unknowns about the origin of the soft photons that are upscattered to higher energies - for example, they may be the photons generated inside the emission region via the original synchrotron radiation (these are Synchrotron-Self Compton (SSC) models), or they may come from outside the emission region (in External Compton (EC) models); see, for example, Krawczynski et al. (2000) and the references therein for a good set-up of the problem as it pertains to correlation studies. Additionally, studies can further look into the two common models of blazar jet emission - "inhomogeneous" models and "homogeneous" models, which both seek to describe the distribution of particles and magnetic field within the jet (Kirk et al. (1998)).

Coppi and Aharonian (1999) predicted that in SSC models, we would expect to see a time delay in the form of gamma rays lagging behind X-rays. A few individual studies have found some evidence for correlations between TeV gamma-ray light curves and X-ray light curves, typically on sub-day scales. One oft-cited work, Fossati et al. (2008a), compared Rossi X-Ray Timing Explorer (RXTE) X-ray data and TeV data from the ground-based HEGRA (High-Energy Gamma Ray Astronomy) telescope and the Whipple telescope of Mrk 421 during the latter half of March 2001. They grouped the data in two ways. The first used their full week data set, with the X-ray data binned in 256 sec bins and the TeV data in 14 to 16 min bins;

doing so they found a DCF peak of $\simeq 0.8$ at a time lag of 0 days. However, when they just looked at a flare on March 18/19 2001, with the X-ray data binned with 128 sec bins and TeV data with 256 sec bins, they found a DCF peak of 0.88 at a time lag of 0 between TeV and hard X-rays, and a DCF peak of 0.84 at a time lag of $\approx +2$ ks between TeV and soft X-rays. The latter indicates the possibility of gamma rays lagging X-rays. As the authors discuss, this correlation lends credence to the idea that the same population of photons in the same emission region are responsible for both the TeV and the soft X-ray photons - as required in SSC models. Furthermore, a study by Krawczynski et al. (2000), which looks at Mrk 501 flare data from 1997, found hints that while there were no correlations between X-ray (25 keV) and gamma-ray (2 TeV) data on a time lag scale of days, there were indications of either simultaneous behavior or the gamma-ray data lagging the X-ray data on the order of hours. Additionally, Rebillot et al. (2006b) found a loose correlation between X-ray and TeV fluxes at a 0 day time lag for Mrk 421 from data accumulated over several weeks.

Other analyses have not found evidence of correlations, nor has there been any evidence for a *trend* of correlations across several different sources. Conclusions of no correlations could give strength to External Compton models, which do not require the same population of photons be responsible for the lower and higher energy emission. For example, Bonning et al. (2009) used Fermi and Swift data from 3C 454.3, and found no correlations between the two, which they interpret as suggesting that an External Compton model may explain the higher energy emission. Additionally, Krawczynski et al. (2004b) found evidence of a TeV gamma-ray flare without an X-ray counterpart. Several of the references cited in this section (for example, Krawczynski et al. (2000)) show that there is no real expectation of correlations on day or week time scales.

It should be noted here that there are two key advantages to the DCF study presented in this thesis. The first is the use of Fermi data. Using Fermi data gives us the ability to look

at emission over a large period of time - i.e., over a year or longer. This enables us to get a much more unbiased look at possible correlations, as we have the potential to witness several flares or other variability in one data set. The second is the fact that we have executed a population study. All of the papers discussed above looked at the DCF for individual sources, often using data from individual flares. In order to be able to draw broader conclusions about the nature of correlations in blazars, the DCF must be applied to several different sources at once, as we have done here.

5.3 Opportunities for Future Study: CTA

The proposed Cherenkov Telescope Array (CTA) represents the next generation of ground-based VHE gamma-ray detectors scheduled to come online within the next few years; its advanced capabilities, which will include an increased sensitivity by an order of magnitude over current instruments, will provide a rich opportunity for enhanced astrophysical studies. The array will consist of a main site in the southern hemisphere, which will primarily be dedicated to galactic observations, and a site in the northern hemisphere, which will focus more on extragalactic science, such as AGN physics. It is projected to begin preliminarily working in 2015-16 and be fully operational by 2018 (Martinez and CTA Consortium (2011)).

Because the array must accommodate a large range of energies (while balancing financial considerations), it will feature multiple configurations, each designed for a specific energy range. For low energies ($\leq$ 100 GeV), there will be a few large telescopes (each with a diameter between 20 and 30 m); since low-energy events are quite common relative to their higher energy counterparts, the use of only a few large telescopes will provide a good ability to observe low-energy gamma rays. For the highest energy photons ($\geq$ 10 TeV), the main concern is the rarity of events; thus, CTA will rely on a large collection area up to km^2 (although the specific configuration of either many smaller telescopes or a few larger ones is not yet decided). The energy range in between will be a "grid of telescopes of the 10 to

15 m class, with a spacing of about 100 m" (Actis et al. (2011)), which will result in an array size that is larger than a typical Cherenkov light pool. For a comprehensive report on the science, objectives, design, and status of CTA, please refer to Actis et al. (2011).

The configuration will provide a large energy coverage, extending as low as 10 GeV and reaching as high as 100 TeV, a sensitivity that should be an order of magnitude better than existing ground-based arrays, and an angular resolution as low as a few arc-minutes (Martinez and CTA Consortium (2011)). Because this array should cover such low energies, it would allow for "nearly seamless coverage" with the Fermi LAT (Martinez and CTA Consortium (2011)), which means that those two projects working together should provide an unprecedented window into the high-energy sky.

For AGN studies, these enhanced specs should allow astrophysicists to see far deeper into the sky than previously. For example, Katarzynski (2011) calculated that CTA should be able to observe a source similar to the famed AGN Mrk 501, which is at a redshift of 0.034, at a redshift as large as 0.4 in 50 hours. This is especially important for LIV studies, which ideally use sources as far away as possible in order to allow for the accumulation of time delay effects - we thus potentially stand to gain a factor of 10 on our constraints. Katarzynski (2011) also points out that the large energy range and the excellent sensitivity should provide better and more precise correlation studies, especially between gamma rays and X-rays - not only will the array allow very high-energy gamma rays to be compared to lower energy counterparts using the same instrument, but the precision of CTA observations will finally start to match those made in the X-ray regime by other instruments.

The real gain to LIV studies will be the potential to detect gamma-ray bursts (GRBs), which are extremely bright, rapid bursts of large amounts of gamma-ray radiation, generally with an afterglow of lower energy radiation. Although the specific mechanics of the bursts are

not yet fully understood, they have been observed to output a large blast of gamma-ray radiation in a very short amount of time (on the order of seconds), typically thought to originate from a region on the order of 10 kilometers in diameter (for a good review, see Mészáros (2006)). Thus, they are capable of variability on the millisecond time scales. (To put this in perspecitve, the fastest flares from AGNs have been found to be on the roughly 100 second time scale.)

For LIV studies, where the parameter we are constraining, E_{QG}, varies as $\Delta E/\Delta t$, we can give a quick order-of-magnitude estimate of how many factors this constraint may gain from the observation of GRBs with CTA, as compared to existing Fermi-based constraints. CTA's effective area will be roughly 10^6 times greater than Fermi's. This means that, when in a signal-limited regime (i.e., when the number of expected background events is roughly 1 or smaller), the observation time to detect a given number of photons will be 10^6 times shorter with CTA than with Fermi. If we are in a background-limited regime (i.e., where the number of expected background events is larger than 1), the time required to detect a given number of photons scales with the square root of the number of photons, meaning that the observation time will be 10^3 times better with CTA than with Fermi. Additionally, the increase in energy (for example, 100 GeV compared to 1 GeV for Fermi) will give a factor of 100; this increase is counterbalanced, though, by a decreased integral flux at higher energies (where the integral flux goes like E^{-1}). These two effects essentially cancel, leaving a potential gain of up to 10^6 in LIV constraints.

Chapter 6

Conclusion

Using temporal data from the ground-based gamma-ray telescope VERITAS, and the space-borne satellites Fermi-LAT and Swift-XRT, we have executed two different projects. The first investigated potential Lorentz invariance violation by using flare data from the blazar Mrk 421. The second looked into possible correlations between gamma-ray and X-ray radiation across 6 different blazars.

Several quantum gravity models have suggested that there will be a breaking of Lorentz invariance at some energy level, E_{QG}, often thought to be near the Planck energy. Amelino-Camelia et al. (1998) first proposed an experimental test of this phenomenon by noting that one consequence would be energy-dependent modifications to the normally energy-independent photon dispersion relation. It was theorized that one could observe the effect by looking at the arrival times of photons, thought to have been emitted at the same time, from a distant astrophysical source. The dispersive effect of LIV should introduce an energy-dependent time delay, which in principle could be measured and used to place constraints on E_{QG}.

We have used the Dispersion Cancellation (DisCan) method to place strong constraints on E_{QG} for both a linear and a quadratic correction term to the typical, energy-independent

photon dispersion relation. This DisCan method used a parameter, θ (which carries units of sec/GeV for a linear model, or sec/GeV^2 for a quadratic model), to shift the arrival times of incident photons according to their energies. Each shifted event list was then evaluated using entropy as a cost function; this was done by binning the data, then calculating the entropy. The θ that produced the event list with the smallest entropy was determined to be the "experimental" θ, called θ_{min}^{obs}. To evaluate this result, we executed a Monte Carlo simulation by scrambling the energies in the original event list to create 1,000 random event lists; each random event list underwent the same entropy-minimization procedure, and the θ_{min}'s from each were collected in a histogram. The results could then be interpreted in a cosmological framework. We used TeV observations of a large flare from Mrk 421 on February 17, 2010 UTC from the VERITAS telescope to calculate the lower limits for the linear, sub-luminal case:

$$|\theta_{95,+}| = 4.56 \times 10^{-3}\,\text{sec/GeV} \tag{6.1}$$

$$E_{QG} > 2.98 \times 10^{18}\,\text{GeV} \tag{6.2}$$

and the quadratic, sub-luminal case:

$$|\theta_{95,+}| = 8.30 \times 10^{-7}\,\text{sec/GeV}^2 \tag{6.3}$$

$$E_{QG} > 1.58 \times 10^{11}\,\text{GeV} \tag{6.4}$$

After comparing these results to existing constraints, we found that **both our linear and quadratic results are among the tightest constraints on the quantum gravity energy scale**.

Because methods that search for dispersive effects use photon arrival time information, we had to make the assumption that any dispersive effects were due solely to Lorentz invariance violation, and not due to an inherent time delay at the source. One way to strengthen this

assumption is to apply the DisCan method to a variety of different sources at different redshifts; any time delays that are due to LIV should scale with distance, while source effects should not. The work presented in this thesis relied only on flare data from one source, meaning that recreating the work for a large number of sources would be a very good direction for future study. However, a second way to strengthen the assumption is through a better understanding of source physics. For example, looking for correlated emission between different energy bands helps to characterize key source properties, including emission region size and the specifics of emission models. Looking for correlations can be done by using the Discrete Correlation Function (DCF).

We have used the DCF (first introduced by Edelson and Krolik (1988), who developed a way to apply the statistical tool called the cross-correlation function to unevenly sampled astrophysical data) to look for correlations between X-ray radiation as recorded by the Swift-XRT satellite, and GeV gamma-ray radiation as observed by the Fermi-LAT satellite. The DCF compares the relative behavior of two different light curves for a variety of different potential time lags. Behavior in one light curve that appears to be mirrored in the other light curve a time lag τ days later (or prior) results in a DCF value close to 1. We investigated a wide range of time lags and found the one that produced the largest DCF. To investigate the significance of the results, we performed Monte Carlo simulations, generating 10,000 random light curves based on the properties of the more evenly sampled data set (in this case, the Fermi data set), and performed the DCF analysis for each random light curve and the Swift X-ray light curve. This led to a chance probability for each experimental DCF.

The strengths of our analysis were two-fold. Firstly, we used data recorded over a long period of time, in some cases up to a year or longer, thus allowing for a fuller investigation into potential correlations. Secondly, we did a population study by applying the analysis to 6 different sources, which enabled us to look for potential trends. By doing this, we were able

to conclude that **we did not see any significant correlations between X-ray and gamma-ray behavior**.

We have shown that the next generation of ground-based instruments, CTA (which should provide, among other things, a full order of magnitude improvement in sensitivity over existing ground-based instruments), could improve LIV-based constraints by up to 6 orders of magnitude. It also stands poised to make tremendous contributions to blazar physics.

Bibliography

A. A. Abdo, M. Ackermann, M. Ajello, et al. A limit on the variation of the speed of light arising from quantum gravity effects. Nature, 462:331–334, Nov. 2009a.

A. A. Abdo, M. Ackermann, M. Ajello, et al. Fermi/Large Area Telescope Bright Gamma-Ray Source List. ApJS, 183:46–66, July 2009b.

A. A. Abdo, M. Ackermann, M. Ajello, et al. Bright Active Galactic Nuclei Source List from the First Three Months of the Fermi Large Area Telescope All-Sky Survey. ApJ, 700: 597–622, July 2009c.

A. A. Abdo, M. Ackermann, I. Agudo, et al. Fermi Large Area Telescope and Multi-wavelength Observations of the Flaring Activity of PKS 1510-089 between 2008 September and 2009 June. ApJ, 721:1425–1447, Oct. 2010a.

A. A. Abdo, M. Ackermann, I. Agudo, et al. The Spectral Energy Distribution of Fermi Bright Blazars. ApJ, 716:30–70, June 2010b.

A. A. Abdo, M. Ackermann, M. Ajello, et al. Multi-wavelength Observations of the Flaring Gamma-ray Blazar 3C 66A in 2008 October. ApJ, 726:43, Jan. 2011a.

A. A. Abdo, M. Ackermann, M. Ajello, et al. Fermi Large Area Telescope Observations of Markarian 421: The Missing Piece of its Spectral Energy Distribution. ApJ, 736:131, Aug. 2011b.

V. A. Acciari, E. Aliu, T. Arlen, et al. Veritas Observations of a Very High Energy γ-Ray Flare From the Blazar 3C 66A. ApJ, 693:L104–L108, Mar. 2009a.

V. A. Acciari, E. Aliu, T. Aune, et al. Simultaneous Multiwavelength Observations of Markarian 421 During Outburst. ApJ, 703:169–178, Sept. 2009b.

M. Ackermann, M. Ajello, A. Allafort, et al. The Second Catalog of Active Galactic Nuclei Detected by the Fermi Large Area Telescope. ApJ, 743:171, Dec. 2011.

M. Actis, G. Agnetta, F. Aharonian, et al. Design concepts for the Cherenkov Telescope Array CTA: an advanced facility for ground-based high-energy gamma-ray astronomy. *Experimental Astronomy*, 32:193–316, Dec. 2011.

F. Aharonian, A. Akhperjanian, M. Beilicke, et al. Variations of the TeV energy spectrum at different flux levels of Mkn 421 observed with the HEGRA system of Cherenkov telescopes. A&A, 393:89–99, Oct. 2002.

F. Aharonian, A. Akhperjanian, M. Beilicke, et al. TeV gamma -ray light curve and energy spectrum of Mkn 421 during its 2001 flare as measured with HEGRA CT1. A&A, 410: 813–821, Nov. 2003.

F. Aharonian, A. G. Akhperjanian, K.-M. Aye, et al. Observations of Mkn 421 in 2004 with HESS at large zenith angles. A&A, 437:95–99, July 2005.

F. Aharonian, A. G. Akhperjanian, U. Barres de Almeida, et al. Limits on an Energy Dependence of the Speed of Light from a Flare of the Active Galaxy PKS 2155-304. *Physical Review Letters*, 101(17):170402, Oct. 2008.

F. A. Aharonian. The Project of the HEGRA Imaging Cherenkov Telescope System: Status and Motivations. In R. C. Lamb, editor, *Towards a Major Atmospheric Cherenkov Detector – II for TeV Astro/Particle Physics*, page 81, 1993.

M. Ajello, M. S. Shaw, R. W. Romani, et al. The Luminosity Function of Fermi-detected Flat-spectrum Radio Quasars. ApJ, 751:108, June 2012.

J. Albert, E. Aliu, H. Anderhub, et al. Observations of Markarian 421 with the MAGIC Telescope. ApJ, 663:125–138, July 2007.

J. Aleksić, L. A. Antonelli, P. Antoranz, et al. MAGIC Observations and multiwavelength properties of the quasar 3C 279 in 2007 and 2009. A&A, 530:A4, June 2011.

E. Aliu, H. Anderhub, L. A. Antonelli, et al. Discovery of a Very High Energy Gamma-Ray Signal from the 3C 66A/B Region. ApJ, 692:L29–L33, Feb. 2009.

G. Amelino-Camelia, J. Ellis, N. E. Mavromatos, D. V. Nanopoulos, and S. Sarkar. Tests of quantum gravity from observations of γ-ray bursts. Nature, 393:763–765, June 1998.

R. Atkins, W. Benbow, D. Berley, et al. Observation of TeV Gamma Rays from the Crab Nebula with Milagro Using a New Background Rejection Technique. ApJ, 595:803–811, Oct. 2003.

W. B. Atwood, A. A. Abdo, M. Ackermann, et al. The Large Area Telescope on the Fermi Gamma-Ray Space Telescope Mission. ApJ, 697:1071–1102, June 2009.

A. S. Bennett. The preparation of the revised 3C catalogue of radio sources. MNRAS, 125: 75, 1962.

S. D. Biller, A. C. Breslin, J. Buckley, et al. Limits to Quantum Gravity Effects on Energy Dependence of the Speed of Light from Observations of TeV Flares in Active Galaxies. *Physical Review Letters*, 83:2108–2111, Sept. 1999.

G. R. Blumenthal and R. J. Gould. Bremsstrahlung, Synchrotron Radiation, and Compton Scattering of High-Energy Electrons Traversing Dilute Gases. *Reviews of Modern Physics*, 42:237–271, 1970.

S. E. Boggs, C. B. Wunderer, K. Hurley, and W. Coburn. Testing Lorentz Invariance with GRB 021206. ApJ, 611:L77–L80, Aug. 2004.

B. M. Bolotovskii. CONFERENCES AND SYMPOSIA: Vavilov - Cherenkov radiation: its discovery and application. *Physics Uspekhi*, 52:1099–1110, Nov. 2009.

E. W. Bonning, C. Bailyn, C. M. Urry, et al. Correlated Variability in the Blazar 3C 454.3. ApJ, 697:L81–L85, June 2009.

J. Buckley. High Speed Electronics for Atmospheric Cherenkov Detectors. In *International Cosmic Ray Conference*, volume 5 of *International Cosmic Ray Conference*, page 267, 1999.

J. Buckley, T. Burnett, G. Sinnis, et al. Gamma-Ray Summary Report. *ArXiv Astrophysics e-prints*, Jan. 2002.

J. H. Buckley, C. W. Akerlof, S. Biller, et al. Gamma-Ray Variability of the BL Lacertae Object Markarian 421. ApJ, 472:L9, Nov. 1996.

D. N. Burrows, J. E. Hill, J. A. Nousek, et al. The Swift X-Ray Telescope. Space Sci. Rev., 120:165–195, Oct. 2005.

R. D. Cohen, H. E. Smith, V. T. Junkkarinen, and E. M. Burbidge. The nature of the BL Lacertae object AO 0235 + 164. ApJ, 318:577–584, July 1987.

P. S. Coppi and F. A. Aharonian. Simultaneous X-Ray and Gamma-Ray Observations of TEV Blazars: Testing Synchro-Compton Emission Models and Probing the Infrared Extragalactic Background. ApJ, 521:L33–L36, Aug. 1999.

C. D. Dermer and R. Schlickeiser. On the location of the acceleration and emission sites in gamma-ray blazars. ApJS, 90:945–948, Feb. 1994.

R. A. Edelson and J. H. Krolik. The discrete correlation function - A new method for analyzing unevenly sampled variability data. ApJ, 333:646–659, Oct. 1988.

J. Ellis, K. Farakos, N. E. Mavromatos, V. A. Mitsou, and D. V. Nanopoulos. A Search in Gamma-Ray Burst Data for Nonconstancy of the Velocity of Light. ApJ, 535:139–151, May 2000.

J. Ellis, N. E. Mavromatos, D. V. Nanopoulos, and A. S. Sakharov. Quantum-gravity analysis of gamma-ray bursts using wavelets. A&A, 402:409–424, May 2003.

J. Ellis, N. E. Mavromatos, D. V. Nanopoulos, A. S. Sakharov, and E. K. G. Sarkisyan. Robust limits on Lorentz violation from gamma-ray bursts. *Astroparticle Physics*, 25: 402–411, July 2006.

J. Ellis, N. E. Mavromatos, D. V. Nanopoulos, A. S. Sakharov, and E. K. G. Sarkisyan. Corrigendum to "Robust limits on Lorentz violation from gamma-ray bursts" [Astropart. Phys. 25 (2006) 402]. *Astroparticle Physics*, 29:158–159, Mar. 2008.

G. G. Fazio, H. F. Helmken, G. H. Rieke, and T. C. Weekes. An experiment to search for discrete sources of cosmic gamma rays in the 10^{11} to 10^{12}eV region. *Canadian Journal of Physics*, 46:451, 1968.

J. D. Finke, J. C. Shields, M. Bottcher, and S. Basu. Redshift limits of BL Lacertae objects from optical spectroscopy. A&A, 477:513–516, Jan. 2008.

G. Fossati, L. Maraschi, A. Celotti, A. Comastri, and G. Ghisellini. A unifying view of the spectral energy distributions of blazars. MNRAS, 299:433–448, Sept. 1998.

G. Fossati, J. H. Buckley, I. H. Bond, et al. Multiwavelength Observations of Markarian 421 in 2001 March: An Unprecedented View on the X-Ray/TeV Correlated Variability. ApJ, 677:906–925, Apr. 2008a.

G. Fossati, J. H. Buckley, I. H. Bond, et al. Multiwavelength Observations of Markarian 421 in 2001 March: An Unprecedented View on the X-Ray/TeV Correlated Variability. ApJ, 677:906–925, Apr. 2008b.

J. A. Gaidos, C. W. Akerlof, S. Biller, et al. Extremely rapid bursts of TeV photons from the active galaxy Markarian 421, Sept. 1996.

N. f. Galante. VERITAS observation of Markarian 421 flaring activity. *ArXiv e-prints*, Sept. 2011.

N. Gehrels, G. Chincarini, P. Giommi, et al. The Swift Gamma-Ray Burst Mission. ApJ, 611:1005–1020, Aug. 2004.

G. Ghisellini, A. Celotti, G. Fossati, L. Maraschi, and A. Comastri. A theoretical unifying scheme for gamma-ray bright blazars. MNRAS, 301:451–468, Dec. 1998.

V. L. Ginzburg and S. I. Syrovatskii. Cosmic Magnetobremsstrahlung (synchrotron Radiation). ARA&A, 3:297, 1965.

R. C. Hartman, D. L. Bertsch, C. E. Fichtel, et al. Detection of high-energy gamma radiation from quasar 3C 279 by the EGRET telescope on the Compton Gamma Ray Observatory. ApJ, 385:L1–L4, Jan. 1992.

R. C. Hartman, D. L. Bertsch, B. L. Dingus, et al. EGRET detection of high-energy gamma radiation from the OVV quasar 3C 454.3. ApJ, 407:L41–L44, Apr. 1993.

R. C. Hartman, D. L. Bertsch, S. D. Bloom, et al. The Third EGRET Catalog of High-Energy Gamma-Ray Sources. ApJS, 123:79–202, July 1999.

HESS Collaboration, A. Abramowski, F. Acero, et al. Search for Lorentz Invariance breaking with a likelihood fit of the PKS 2155-304 flare data taken on MJD 53944. *Astroparticle Physics*, 34:738–747, Apr. 2011.

A. M. Hillas. Cerenkov light images of EAS produced by primary gamma. In F. C. Jones, editor, *International Cosmic Ray Conference*, volume 3 of *International Cosmic Ray Conference*, pages 445–448, Aug. 1985.

J. A. Hinton and W. Hofmann. Teraelectronvolt Astronomy. ARA&A, 47:523–565, Sept. 2009.

J. Holder, V. A. Acciari, E. Aliu, et al. Status of the VERITAS Observatory. In F. A. Aharonian, W. Hofmann, & F. Rieger, editor, *American Institute of Physics Conference Series*, volume 1085 of *American Institute of Physics Conference Series*, pages 657–660, 2008.

S. Inoue and F. Takahara. Electron Acceleration and Gamma-Ray Emission from Blazars. ApJ, 463:555, June 1996.

J. D. Jackson. *Classical Electrodynamics, 3rd Edition*. July 1998.

U. Jacob and T. Piran. Lorentz-violation-induced arrival delays of cosmological particles. J. Cosmology Astropart. Phys., 1:31, Jan. 2008.

T. Jacobson, S. Liberati, and D. Mattingly. Astrophysical Bounds on Planck Suppressed Lorentz Violation. In J. Kowalski-Glikman & G. Amelino-Camelia, editor, *Lecture Notes in Physics, Berlin Springer Verlag*, volume 669 of *Lecture Notes in Physics, Berlin Springer Verlag*, pages 101–130, 2005.

N. Jarosik, C. L. Bennett, J. Dunkley, et al. Seven-year Wilkinson Microwave Anisotropy Probe (WMAP) Observations: Sky Maps, Systematic Errors, and Basic Results. ApJS, 192:14, Feb. 2011.

M. M. Jordan. *Multiwavelength observations of Markarian 421*. PhD thesis, Washington University, Missouri, USA, 2004.

P. Kaaret. Pulsar radiation and quantum gravity. A&A, 345:L32–L34, May 1999.

J. Kataoka, G. Madejski, M. Sikora, et al. Multiwavelength Observations of the Powerful Gamma-Ray Quasar PKS 1510-089: Clues on the Jet Composition. ApJ, 672:787–799, Jan. 2008.

K. Katarzynski. CTA Constraints on AGN models. In *AGN Physics in the CTA Era (AGN 2011)*, 2011.

J. G. Kirk, F. M. Rieger, and A. Mastichiadis. Particle acceleration and synchrotron emission in blazar jets. A&A, 333:452–458, May 1998.

A. Kohnle, F. Aharonian, A. Akhperjanian, et al. Stereoscopic imaging of air showers with the first two HEGRA Cherenkov telescopes. *Astroparticle Physics*, 5:119–131, Aug. 1996.

H. Krawczynski, P. S. Coppi, T. Maccarone, and F. A. Aharonian. X-ray/TeV-gamma-ray observations of several strong flares of Mkn 501 during 1997 and implications. A&A, 353: 97–107, Jan. 2000.

H. Krawczynski, S. B. Hughes, D. Horan, et al. Multiwavelength Observations of Strong Flares from the TeV Blazar 1ES 1959+650. ApJ, 601:151–164, Jan. 2004a.

H. Krawczynski, S. B. Hughes, D. Horan, et al. Multiwavelength Observations of Strong Flares from the TeV Blazar 1ES 1959+650. ApJ, 601:151–164, Jan. 2004b.

H. Krawczynski, D. A. Carter-Lewis, C. Duke, et al. Gamma hadron separation methods for the VERITAS array of four imaging atmospheric Cherenkov telescopes. *Astroparticle Physics*, 25:380–390, July 2006.

F. Krennrich, I. H. Bond, S. M. Bradbury, et al. Discovery of Spectral Variability of Markarian 421 at TeV Energies. ApJ, 575:L9–L13, Aug. 2002.

K. M. Lanzetta, D. A. Turnshek, and J. Sandoval. Ultraviolet spectra of QSOs, BL Lacertae objects, and Seyfert galaxies. ApJS, 84:109–184, Feb. 1993.

M. S. Longair. *High energy astrophysics. Vol.1: Particles, photons and their detection*. Mar. 1992.

D. Maccagni, B. Garilli, R. Schild, and M. Tarenghi. X-ray/optical brightness trends in 3C 66A. A&A, 178:21–24, May 1987.

MAGIC Collaboration, J. Albert, E. Aliu, et al. Probing quantum gravity using photons from a flare of the active galactic nucleus Markarian 501 observed by the MAGIC telescope. *Physics Letters B*, 668:253–257, Oct. 2008.

F. Makino, T. Kii, K. Hayashida, et al. X-ray outburst of the quasar 3C 279. ApJ, 347: L9–L12, Dec. 1989.

M. Martinez and CTA Consortium. Introduction to the CTA Project. In *AGN Physics in the CTA Era (AGN 2011)*, 2011.

D. Mattingly. Modern Tests of Lorentz Invariance. *Living Reviews in Relativity*, 8:5, Sept. 2005.

J. Maza, P. G. Martin, and J. R. P. Angel. On the composite nature of the BL Lacertae objects Markarian 421 and 501. ApJ, 224:368–374, Sept. 1978.

P. Mészáros. Gamma-ray bursts. *Reports on Progress in Physics*, 69:2259–2321, Aug. 2006.

J. S. Miller, H. B. French, and S. A. Hawley. Optical spectra of BL Lacertae objects. In A. M. Wolfe, editor, *BL Lac Objects*, pages 176–187, 1978.

R. Misra, A. Bora, and G. Dewangan. Analytical error estimate for the cross-correlation, phase and time lag between two light curves. *ArXiv e-prints*, June 2010.

P. L. Nolan, A. A. Abdo, M. Ackermann, et al. Fermi Large Area Telescope Second Source Catalog. ApJS, 199:31, Apr. 2012.

K. J. E. Northover. The radio galaxy 3C 66. MNRAS, 165:369, 1973.

R. A. Ong, V. A. Acciari, T. Arlen, et al. Highlight Talk: Recent Results from VERITAS. *ArXiv e-prints*, Dec. 2009.

L. Pacciani, V. Vittorini, M. Tavani, et al. The 2009 December Gamma-ray Flare of 3C 454.3: The Multifrequency Campaign. ApJ, 716:L170–L175, June 2010.

D. H. Perkins. *Particle astrophysics*. 2003.

M. B. Priestley. *Spectral Analysis and Time Series*. Elsevier Academic Press, 2004.

J. R. Primack, J. S. Bullock, and R. S. Somerville. Observational Gamma-ray Cosmology. In F. A. Aharonian, H. J. Völk, and D. Horns, editors, *High Energy Gamma-Ray Astronomy*, volume 745 of *American Institute of Physics Conference Series*, pages 23–33, Feb. 2005.

M. Punch, C. W. Akerlof, M. F. Cawley, et al. Detection of TeV photons from the active galaxy Markarian 421. Nature, 358:477, Aug. 1992.

M. Rabbette, S. McBreen, B. Steel, and N. Smith. Rapid optical variability in the BL Lacertae object AO 0235+164. A&A, 310:1–7, June 1996.

C. M. Raiteri, M. Villata, M. Kadler, et al. Multifrequency variability of the blazar AO 0235+164. The WEBT campaign in 2004-2005 and long-term SED analysis. A&A, 459: 731–743, Dec. 2006.

P. F. Rebillot, H. M. Badran, G. Blaylock, et al. Multiwavelength Observations of the Blazar Markarian 421 in 2002 December and 2003 January. ApJ, 641:740–751, Apr. 2006a.

P. F. Rebillot, H. M. Badran, G. Blaylock, et al. Multiwavelength Observations of the Blazar Markarian 421 in 2002 December and 2003 January. ApJ, 641:740–751, Apr. 2006b.

M. Rodríguez Martínez and T. Piran. Constraining Lorentz violations with gamma ray bursts. J. Cosmology Astropart. Phys., 4:6, Apr. 2006.

R. W. Romani, D. Sowards-Emmerd, L. Greenhill, and P. Michelson. Q0906+6930: The Highest Redshift Blazar. ApJ, 610:L9–L11, July 2004.

G. B. Rybicki and A. P. Lightman. *Radiative processes in astrophysics*. 1979.

M. Sasada, M. Uemura, Y. Fukazawa, et al. Prominent Polarized Flares of the Blazars AO 0235+164 and PKS 1510-089. PASJ, 63:489–, June 2011.

T. Savolainen, D. C. Homan, T. Hovatta, et al. Relativistic beaming and gamma-ray brightness of blazars. A&A, 512:A24, Mar. 2010.

T. Sbarrato, G. Ghisellini, L. Maraschi, and M. Colpi. The relation between broad lines and γ-ray luminosities in Fermi blazars. MNRAS, 421:1764–1778, Apr. 2012.

J. D. Scargle, J. P. Norris, and J. T. Bonnell. An algorithm for detecting quantum gravity photon dispersion in gamma-ray bursts: Discan. *The Astrophysical Journal*, 673(2):972, 2008. URL `http://stacks.iop.org/0004-637X/673/i=2/a=972`.

B. E. Schaefer. Severe Limits on Variations of the Speed of Light with Frequency. *Physical Review Letters*, 82:4964–4966, June 1999.

M. Schmidt. 3C 273 : A Star-Like Object with Large Red-Shift. Nature, 197:1040, Mar. 1963.

H. Spinrad and H. E. Smith. AO 0235+164 a red BL Lacertae object. ApJ, 201:275–276, Oct. 1975.

F. W. Stecker. Constraints on Lorentz invariance violating quantum gravity and large extra dimensions models using high energy γ-ray observations. *Astroparticle Physics*, 20:85–90, Nov. 2003.

F. W. Stecker. Stellar Photon and Blazar Archaeology with Gamma-rays. *ArXiv e-prints*, Sept. 2007.

F. W. Stecker, O. C. de Jager, and M. H. Salamon. TeV gamma rays from 3C 279 - A possible probe of origin and intergalactic infrared radiation fields. ApJ, 390:L49–L52, May 1992.

W. A. Stein, S. L. Odell, and P. A. Strittmatter. The BL Lacertae objects. ARA&A, 14: 173–195, 1976.

S. Swordy. Discovery of $>$ 100 GeV Gamma-ray Emission from the Blazar 3C66A by VERITAS. *The Astronomer's Telegram*, 1753:1, Oct. 2008.

D. J. Thompson, S. Djorgovski, and R. de Carvalho. Spectroscopy of radio sources from the Parkes 2700 MHz survey. PASP, 102:1235–1240, Nov. 1990.

J. Timmer and M. Koenig. On generating power law noise. A&A, 300:707, Aug. 1995.

Y. Uchiyama, C. M. Urry, C. C. Cheung, et al. Shedding New Light on the 3C 273 Jet with the Spitzer Space Telescope. ApJ, 648:910–921, Sept. 2006.

M.-H. Ulrich, T. D. Kinman, C. R. Lynds, G. H. Rieke, and R. D. Ekers. Nonthermal continuum radiation in three elliptical galaxies. ApJ, 198:261–266, June 1975.

C. M. Urry and P. Padovani. Unified Schemes for Radio-Loud Active Galactic Nuclei. PASP, 107:803, Sept. 1995.

S. Vercellone, A. W. Chen, V. Vittorini, et al. Multiwavelength Observations of 3C 454.3. I. The AGILE 2007 November campaign on the "Crazy Diamond". ApJ, 690:1018–1030, Jan. 2009.

VERITAS Collaboration: T. Nagai, R. McKay, G. Sleege, and D. Petry. Focal Plane Instrumentation of VERITAS. *ArXiv e-prints*, Sept. 2007.

H. J. Völk and K. Bernlöhr. Imaging very high energy gamma-ray telescopes. *Experimental Astronomy*, 25:173–191, Aug. 2009.

S. Wakely and D. Horan. TeVCat. `http://tevcat.uchicago.edu/`, 2012.

T. C. Weekes. The Atmospheric Cherenkov Imaging Technique for Very High Energy Gamma-ray Astronomy. *ArXiv Astrophysics e-prints*, Aug. 2005.

T. C. Weekes. TeV Gamma-ray Astronomy: The Story So Far. In F. A. Aharonian, W. Hofmann, and F. Rieger, editors, *American Institute of Physics Conference Series*, volume 1085 of *American Institute of Physics Conference Series*, pages 3–17, Dec. 2008.

T. C. Weekes, M. F. Cawley, D. J. Fegan, et al. Observation of TeV gamma rays from the Crab nebula using the atmospheric Cerenkov imaging technique. ApJ, 342:379–395, July 1989.

A. R. Whitney, I. I. Shapiro, A. E. E. Rogers, et al. Quasars Revisited: Rapid Time Variations Observed Via Very-Long-Baseline Interferometry. *Science*, 173:225–230, July 1971.

C. M. Will. The Confrontation between General Relativity and Experiment. *Living Reviews in Relativity*, 9:3, Mar. 2006.

B. J. Wills and D. Wills. C 66A: a Bright New Quasi-Stellar Object. ApJ, 190:L97, June 1974.

M. Zhai, W. K. Zheng, and J. Y. Wei. Multi-colour optical variability of the blazar 3C 454.3 in 2007-2010. A&A, 531:A90, July 2011.